Dissertation

Dissipative and anisotropic corrections to the kinetic freeze-out in relativistic heavy-ion collisions

Christian Lang

May 2016

Faculty of Physics
University Bielefeld

Supervisor & 1st referee: Prof. Dr. Nicolas Borghini
2nd referee: Prof. Dr. Dietrich Bödeker

Contents

Abstract

Matter produced in relativistic heavy-ion collisions follows the laws of relativistic hydrodynamics when it has reached thermal equilibrium. The hydrodynamic model of choice is often the model of a perfect fluid. In recent years dissipative corrections have been applied to this model to account for several dissipative phenomena.

A significant part of the changes in the momentum distributions induced by dissipative phenomena in the description of the created matter actually takes place when the fluid turns into individual particles. We study these corrections in the limit of a low freeze-out temperature of the flowing medium and we show that they mostly affect particles with a higher velocity than the fluid. For these, we derive relations between different flow coefficients, from which the functional form of the dissipative corrections could ultimately be reconstructed from experimental data.

Although the dissipative relativistic fluid dynamic description of the extended matter is quite successful, it requires a prescription for converting the fluid into particles. We present further arguments in favor of using a locally anisotropic momentum distribution for the particles emitted from the fluid, so as to smooth out discontinuities introduced by the usual conversion prescriptions. Building on this ansatz, we investigate the effect of the anisotropy on several observables of heavy-ion physics.

1 Introduction

Our current understanding of nature involves four fundamental forces: gravity, electromagnetism, the weak force and the strong force. Electromagnetism and the weak force are joined together in a unified theory of electro-weak interaction and it is attempted to further include the strong force to gain a grand unified theory. Regardless, the strong force is in itself an interesting subject for studies together with the fundamental particles which are affected by it: quarks and gluons. All together, quarks, gluons and the strong force are forming the "ingredients" to quantum chromodynamics (QCD), one of the most fundamental physical theories describing the subatomic matter.

Since the first steps of QCD, which started more or less with Gell-Mann's eightfold way[1] in 1961 as a phenomenological model, many new features were found. Especially one should name the color degrees of freedom or the running coupling which leads to the concept of asymptotic freedom. The latter one results in a very interesting property of QCD. Depending on the energy scale at which one examines strong interactions, the strength of the coupling varies. For low energies the coupling is very strong, resulting in the phenomenon of confinement. Confinement means that the constituents of QCD (quarks and gluons) can never be set free like, for example, electrons. Quarks and gluons always have to be bound together to hadrons. On the other hand, for very high energies the coupling is very small and the binding of the hadrons weakens. However, this does not lead to free quarks and gluons, since the concept of color provides no possibility for free quarks or gluons.

The concept of color implies that every quark carries an internal degree of freedom which can take one of three possible colors[2], often called red,

[1] Another attempt to describe subatomic matter was Feynman's parton model. However the parton model only plays a minor role nowadays.

[2] We neglect the colors of the gluons since this subject is more complicated and not relevant in this thesis.

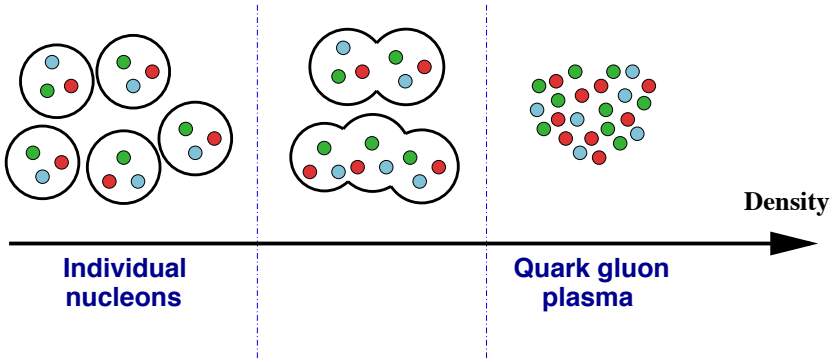

Figure 1.1: Schematic view of the creation of the quark-gluon-plasma. [1]

green and blue[3]. The observable hadrons however do not carry a color, therefore every hadron fulfills one of the following two cases: Either, the hadron is a meson, which consists of a quark with a color and an anti-quark with the corresponding anti-color, or the hadron is a baryon consisting of three quarks where every quark has one of the possible three colors. Both types, mesons and baryons, are called color neutral (white) and are bound states of quarks.

Going back to high energies: If the interaction weakens, but no colored particles can be observed, what is actually happening? The answer is simple: Only the interaction between the quarks weakens, resulting in the effect seen in figure 1.1. The individual hadrons are starting to dissolve and form a single form of matter, called the quark-gluon-plasma (QGP). Since the proposition of the QGP it has been studied, theoretically and experimentally.

The theoretical frameworks for QCD, respectively the QGP, are perturbative QCD (pQCD) or lattice QCD (lQCD). Both techniques describe QCD and the QGP very well, but only in a certain region. pQCD works for high temperatures, while lQCD needs a vanishing chemical potential. The experiments in which the QGP is probed are *relativistic heavy-ion*

[3]It may be obvious, but quarks and gluons do not have an actual color. Instead it is just a name for a new degree of freedom.

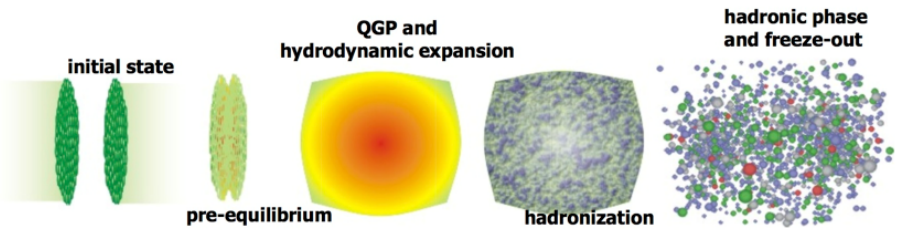

Figure 1.2: Schematic view of a relativistic heavy-ion collision. [2]

collisions. A schematic view of a typical collision in such an experiment is shown in figure 1.2. As it turns out, the created matter in such collisions has many different stages, starting with a pre-equilibrium phase and ending with free streaming hadrons.

The challenge is to combine the different stages of a heavy-ion collision with the theoretical frameworks of pQCD or lQCD to achieve physical insight to the produced matter. This is still a "work in progress". However, if one is only interested in understanding the process of heavy-ion collisions, it may be promising to revert back to an *effective theory* instead of the real theories. Effective theories, like the popular theory of *hydrodynamics*, have the advantage that they can be much simpler than the real QCD-theories, which allows a faster framework to examine and understand heavy-ion collisions.

Experiments

The details of the different properties of QCD, like the QGP and confinement, are still a subject of current research. Experimentally, these subjects are probed in relativistic particle colliders. At present, the two largest colliders in operation are the **L**arge **H**adron **C**ollider (LHC) at CERN with its most important experiments ALICE, ATLAS and CMS[4], and the **R**elativistic **H**eavy **I**on **C**ollider (RHIC) at BNL with the PHENIX and STAR experiments.

Both colliders are circular colliders, where the heavy-ions are first accel-

[4]There are further experiments at LHC, for example LHCb.

erated in smaller linear and circular accelerators before they are inserted into the main storage ring, where the ions circulate until they collide in the different experiments. The heavy-ions used in the experiments are gold at RHIC and lead at LHC. The kinetic energy of the individual ions at RHIC is about 100 GeV per nucleon, while at LHC an energy of about 2 TeV per nucleon can be achieved.

Inside the collider several packets of heavy-ions, called bunches, are circling around, both clock-wise and counter-clock-wise, in two different tubes. The experiments are placed where the tubes intersect, which allows the two "beams" of heavy-ions to collide. The actual experiments consists of several detectors for different particles, such that the particle type (and therefore its quantum numbers, like mass, charge, etc.), the kinetic energy, and the position of the detection can be extracted. Different detectors are needed for each individual experiment, depending on the particle type it should detect. Most of the detectors in the experiments are build perpendicular around the collider, similar to a big cylinder. Few are placed near the entrance and exit of the experiment, close to the beam, where the most energetic particles are observed.

Starting from QCD-theories, it is possible to calculate various cross sections which can be tested against the experimental results. Unfortunately not only calculating the cross sections itself, but also relating them to the experimental data, can be a challenging task. It seemed therefore promising to use an effective theory to describe the experimental results.

Effective theories

The QGP created in heavy-ion collisions is often called a "strongly interacting matter" or, more simply, a *fireball*. This implies that the created particles are viewed as a form of matter instead of individual particles. This allows us to use macroscopic thermodynamic concepts like temperature and pressure. Then it is natural to describe the dynamical evolution of the collision with a macroscopic approach, namely hydrodynamics. This idea dates back to 1953, proposed by L. D. Landau [3].

Experimental data underlines the concept, that the created matter in heavy-ion collisions acts like a fluid [4]. The most striking experimental observation is the phenomena of jet quenching [5]. If two particles, for example protons, collide, several new particles are created in pairs due to

the conservation of momentum and energy. It is possible that such a single particle pair can gain a large amount of kinetic energy and both particles fly in two opposing directions, accounting for momentum conservation. The two particles can later be observed distinctly in the detectors and are called jets. In the presence of the fireball only one jet is observed. The other particle has to traverse through the dense matter of the fireball and in the process loses momentum and energy until it can no longer be detected individually.

The chapter concludes with two remarks. Recent experimental data showed that the matter created in heavy-ion collisions is not in a global thermal equilibrium. However, many older descriptions of the QGP depend on this assumption of a global thermal equilibrium and seem to be no longer valid. Nevertheless, local thermal equilibrium can still be achieved during the process of a heavy-ion collision. For effective theories like hydrodynamics a local thermal equilibrium is sufficient enough to be applied. Still, this also shows clearly the limits of effective theories. If one can not assume local thermodynamic equilibrium, hydrodynamics is not applicable. Indeed this is happening at the beginning, after the fireball is created, and at the end, when the individual hadrons are set free (figure 1.2). Another possible theory to describe the collision is a kinetic theory, but compared to hydrodynamics this theory is more complex.

Outline

In this thesis we use the effective theory of relativistic hydrodynamics to describe the last stage of a heavy-ion collision. In this last stage the QGP disintegrates into several hadrons, a process which is called freeze-out. The whole process of freeze-out is still not completely understood, both in theoretical and experimental aspects, and is still a subject to current research.

From a theoretical point of view, the main problem of the freeze-out is that the created hadrons can not be described by the equations of hydrodynamics and a new theory has to take its place, for example a kinetic theory. Nonetheless, it is possible to use an ansatz for the freeze-out itself to calculate possible observables of the later detected hadrons. Here we restrict ourself purely to the theoretical part. The ansatz involves aspects of both sides at the freeze-out. It includes the momenta of the created hadrons and the flow profile of the fluid-like QGP.

In the presented work the flow profile is modified. We start with a perfect fluid flow for the QGP and include separately dissipative and anisotropic corrections. The dissipative corrections are used to expand the known relations between different flow harmonics and to find new methods to extract the dissipative properties from experimental data. The anisotropic corrections are utilized to smooth out the transition from a fluid to individual particles and the effects on several observables are investigated.

Structure

The layout of the thesis is structured as follows:

Starting with a brief introduction of relativistic heavy-ion collisions in chapter 2, we set the focus on the different stages of a heavy-ion collision. Furthermore, three possible observables of heavy-ion collisions, the particle momentum spectrum (transverse momentum spectrum), anisotropic flow, and HBT-radii are illustrated. For all three observables one possible way to calculate them is shown.

In chapter 3 we present the basics of relativistic hydrodynamics for a perfect and for a dissipative fluid. Although the hydrodynamic equations are not explicitly needed in the thesis, we can extract some concepts and ideas for the following chapters, mainly regarding first order dissipative corrections. Finally, we present a possible calculation method for the fields with the help of the Boltzmann equation.

The subject of the chapters 4 and 5 is to calculate the observables from a specific ansatz, the sudden freeze-out approximation. The fourth chapter is a short summary of an article from 2006 by N. Borghini and J.-Y. Ollitrault [6], where a perfect fluid was involved. In the fifth chapter dissipative corrections are introduced to enhance the previous calculations. The chapter concludes with a comparison to a numerical model, the blast-wave model.

The last part is grouped into two chapters. In chapter 6 the concepts of anisotropic hydrodynamics are introduced, along with a motivation for the need of an anisotropic momentum distribution. Afterwards, the basic hydrodynamical fields are calculated for an anisotropic fluid, which is used in chapter 7 to once more calculate the observables within the sudden freeze-out approximation. However, compared to chapter 5, the obtained results are only numerical calculations within the blast-wave model.

The thesis closes with a conclusion, where the results of both types of corrections, dissipative and anisotropic, are summarized. Also, an outlook is provided.

Conventions

Throughout the thesis the following conventions are used:

- 4-vectors are written in sans serif font or in component representation (e.g. x or x^μ), normal vectors are denoted by an arrow above (e.g. $\vec{p}$) and two-dimensional vectors are in bold font with an arrow above (e.g. $\vec{\mathbf{u}}_\mathbf{t}$).
- In our calculations we use natural units, electronvolt (eV) and fermi (fm), and therefore set $\hbar = c = k_B = 1$.
- In Minkowski coordinates the following metric is used

$$g^{\mu\nu} = \begin{pmatrix} 1 & 0 & 0 & 0 \\ 0 & -1 & 0 & 0 \\ 0 & 0 & -1 & 0 \\ 0 & 0 & 0 & -1 \end{pmatrix}.$$

- In cylindrical coordinates we use the metric

$$g^{\mu\nu} = \begin{array}{c} \\ \tau \\ \eta \\ r \\ \phi \end{array} \begin{array}{c} \begin{array}{cccc} \tau & \eta & r & \phi \end{array} \\ \begin{pmatrix} 1 & 0 & 0 & 0 \\ 0 & -\tau^2 & 0 & 0 \\ 0 & 0 & -1 & 0 \\ 0 & 0 & 0 & -r^2 \end{pmatrix} \end{array}.$$

2 Relativistic heavy-ion collisions

Relativistic collisions of heavy-ions are a well established tool to study subatomic matter. With increasing collision energy subatomic matter is probed at finer resolutions and new facets of the subatomic world are revealed.

In a collision at very low energies the nuclei as a whole are interacting with each other, while the nucleons, protons and neutrons, inside are unaffected. As the energy increases, the nucleons start to interact and the production of new particles is initiated. At even higher energies, the quarks and gluons inside the individual nucleons start to interact, which is the beginning of relativistic heavy-ion collisions. But unlike at low and medium energies, where the collisions can be described in terms of nucleon-nucleon-collisions, in relativistic heavy-ion collisions such a description fails. [7]

In the following sections, we explain the different stages of a relativistic heavy-ion collision and how to model them. Furthermore, we present possible observables of a collision and explain in detail three of them: the particle momentum distribution, the anisotropic flow, and the HBT-radii.

2.1 Stages of relativistic heavy-ion collisions

A heavy-ion collision at relativistic energies passes through several stages until the hadrons are created, which are later detected in the experiments. A space-time diagram with the different stages of the collision is shown in figure 2.1 on page 16. Starting from the diagram in 2.1 the following stages are classified. [7]

1. *Pre-equilibrium*
   At relativistic energies, the initial collisions are expected to be at partonic level. The initial partonic collisions produce the so called fireball, a dense and highly excited state of matter, consisting to

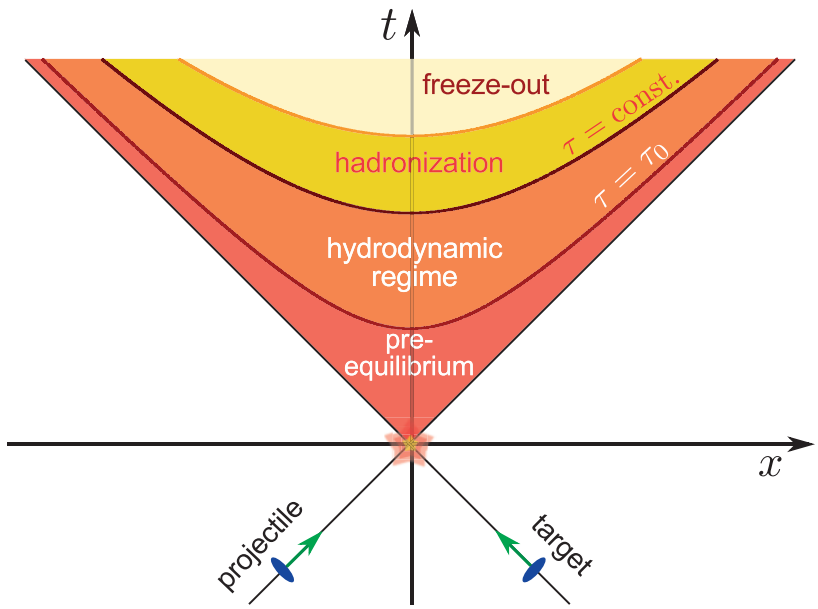

Figure 2.1: Space-time diagram of a collision. The colliding ions are labeled as projectile and target and collide at the origin of the diagram. [8]

a large extend of gluons. This fireball is not in equilibrium and the constituents collide frequently to establish a local equilibrium state. The time to establish the local equilibrium state is called thermalization time and it takes approximately 1 fm to reach this state.

2. *Expansion (Hydrodynamics and Hadronization)*
In the (thermalized) equilibrium state, the constituents of the fireball are the individual partons (quarks and gluons). The partons are still in a deconfined state and the whole fireball has a thermal pressure, acting against the surrounding vacuum. Therefore the fireball undergoes a *collective expansion*, often described by hydrodynamics. During the expansion, the (energy) density decreases and the

system cools down. Below a critical temperature the deconfined partons hadronize and are forming light particles, for example pions. In the *hadronization* stage the entropy density decreases very fast over a small time interval. This implies that the fireball expands rapidly, while the temperature remains approximately constant. This process occurs due to the total entropy conservation.

3. *Freeze-out*
   Even after the hadronization, the matter can still be in local thermal equilibrium. Constituent hadrons collide to maintain equilibrium, but the system is still expanding and cooling down. Eventually, a stage is reached in which inelastic collisions become too small to keep up with the expansion. This stage is called the *chemical freeze-out*, where the hadron abundances remain fixed after this stage. However, the system remains in its expansion and still cools down, since elastic collisions may still be happening. At a certain point, the system reaches a stage where the average distance between the constituents is larger than the interaction range. Collisions between the hadrons are so infrequent that the local thermal equilibrium cannot be maintained. The hydrodynamic description breaks down and the hadrons decouple, they freeze-out. This is the so called *kinetic freeze-out* and the free floating hadrons from this stage are later detected in the experiments.

There are several models for relativistic heavy-ion collisions. They are roughly categorized into two groups: static and dynamic models. The static models try to explain experimental results by modeling the freeze-out conditions, while the dynamic models try to answer how the freeze-out is reached after the initial collision occurred. Currently there are two major dynamic models: hydrodynamics and kinetic theory. Even if the hydrodynamic model is restricted from the expansion stage to freeze-out[1], it is more elementary compared to a kinetic model. As for the static model, we restrict ourself to the popular Cooper-Frye model to describe the kinetic freeze-out. The chemical freeze-out is neglected, therefore we refer to the kinetic freeze-out simply by writing freeze-out.

[1] A kinetic theory may describe the whole process from pre-equilibrium to freeze-out.

2.2 Observables

In this section the main goal is to characterize possible observables of a relativistic heavy-ion collision. There are many different observables, starting with rather simple ones like the particle multiplicity, which is simply counting all particles produced in a collision, up to more complex ones like different correlation functions.

Here we want to present two of these observables: The particle momentum distribution and the anisotropic flow. Both observables are used to describe the collective dynamics of a heavy-ion collision and can be linked together. As written before, we are interested in the kinetic freeze-out, therefore we focus on the particle momentum distribution and the anisotropic flow at this point in the dynamical process.

2.2.1 Particle momentum distribution

Like the particle multiplicity, the particle momentum distribution is a rather simple observable. The actual measurement in real experiments is a basic task and used to calculate further properties of the created matter in the collisions. The particle momentum distribution is the number of particles in a certain momentum interval, which is written as $d^3N/d^3\vec{p}$. Unfortunately this expression is not invariant under Lorentz transformation. The best method to achieve an invariant observable and therefore making it easier to handle, is to multiply $d^3N/d^3\vec{p}$ by the energy $E_{\vec{p}}$ of the corresponding particles with momentum $\vec{p}$. The new observable is the particle momentum distribution

$$E_{\vec{p}}\frac{d^3N}{d^3\vec{p}}. \tag{2.1}$$

In the next step we want to present a possible method to calculate the particle momentum distribution (2.1). The method we choose was introduced by F. Cooper and G. Frye in 1974 [9] and led to the known *Cooper-Frye formula*. The general idea of their work was to describe the particle momentum distribution on a certain surface where it depends on the one-particle distribution with a collective velocity $\vec{v}$. In the following a short derivation is presented, found in [10, p. 232].

Starting with the criterion that when the temperature T reaches a certain point T_f all processes in the created matter stop. This behavior is

easily adopted in the hydrodynamic description of the heavy-ion collision. The condition $T = T_f$ defines a three-dimensional hypersurface in the four-dimensional Minkowski space-time. Due to the hydrodynamic description we know other thermodynamical quantities and flow parameters on the hypersurface and together with these informations we can calculate different observables, like the particle momentum distribution.

We start in the local rest frame of the particles, the particle number in a small volume element dV at equilibrium can be expressed as

$$dN = dVn = dV \int d^3\vec{p}\, f_{eq}(E_{\vec{p}}). \tag{2.2}$$

The issue with this formula is that it is not Lorentz invariant and therefore it is only valid in the rest frame of the particles. We generalize (2.2) by writing it in a covariant way

$$dN = dVn = dV_\mu \int \frac{d^3\vec{p}}{E_{\vec{p}}} p^\mu f(p^\nu u_\nu) \tag{2.3}$$

with the four-velocity field u^ν of the fluid modeled with the help of hydrodynamics and $dV^\mu = dVu^\mu$. It is clear, that in the rest frame where u^μ is equal to $(1, 0, 0, 0)$, the equation (2.3) is reduced to equation (2.2). The total number of particles is obtained by integrating over the volume element dV^μ. However, both dV^μ and u^μ depend on the space-time position x. We achieve the total particle number

$$N = \int dV_\mu(\mathsf{x}) \int \frac{d^3\vec{p}}{E_{\vec{p}}} p^\mu f(p^\nu u_\nu(\mathsf{x})). \tag{2.4}$$

With this equation we are almost finished and can determine the distribution of the emitted particles on the hypersurface, but an important modification has to be done yet.

The volume elements cannot be generally written in the form $dV^\mu = dVu^\mu$. For example, at the early stages of the collision the emitted particles have a surface character and an appropriate fluid element is obtained by the multiplication of the area of the emission region by the time this emission takes place. In this case dV^μ is space-like and thus the structure of equation (2.4) is of the desired form. But the fluid element $dV^\mu(\mathsf{x})$ should be taken independently of $u^\mu(\mathsf{x})$. It is reasonable that the form

of $dV^\mu(\mathsf{x})$ should follow from the model used to describe the space-time evolution of the matter.

With this remark in mind we rewrite the number of particles N which decouple on the freeze-out hypersurface Σ:

$$N = \int \frac{d^3\vec{p}}{E_{\vec{p}}} \int d\Sigma_\mu(\mathsf{x})\, p^\mu f(\mathsf{x}, \mathsf{p}). \tag{2.5}$$

This is the first form of the Cooper-Frye formula. The element dV moving with the four-velocity u^μ is replaced by the three-dimensional element of the freeze-out hypersurface $d\Sigma_\mu$. With the help of differential geometry it is possible to calculate $d\Sigma_\mu$ by using

$$d\Sigma_\mu = \epsilon_{\mu\nu\rho\sigma} \frac{dx^\nu}{d\nu} \frac{dx^\rho}{d\rho} \frac{dx^\sigma}{d\sigma} d\nu d\rho d\sigma, \tag{2.6}$$

with $\epsilon_{\mu\nu\rho\sigma}$ the Levi-Civita tensor and three parameters ν, ρ, and σ, which are used to parameterize the three-dimensional hypersurface in the four-dimensional Minkowski space-time. More details on $d\Sigma^\mu$ can be found in [10, p. 233-235]. The particle momentum distribution from equation (2.5) is rewritten to

$$E_{\vec{p}} \frac{d^3N}{d^3\vec{p}} = \int d\Sigma_\mu(\mathsf{x})\, p^\mu f(\mathsf{x}, \mathsf{p}). \tag{2.7}$$

If the particles are still in local equilibrium we replace the function $f(\mathsf{x}, \mathsf{p})$ with the equilibrium distribution function

$$f_{eq}(p^\nu u_\nu) = \frac{1}{(2\pi)^3} \frac{1}{e^{\frac{p^\nu u_\nu - \mu}{T}} - \alpha}. \tag{2.8}$$

For $\alpha = +1$ the formula (2.8) corresponds to the Bose-Einstein statistics, for $\alpha = -1$ to the Fermi-Dirac statistics and in the limit $\alpha \to 0$ the classical Maxwell-Boltzmann statistics are obtained.

2.2.2 Anisotropic Flow

When two heavy-ions collide they almost never collide head on. Instead the collision is characterized by an impact parameter b. At finite b every

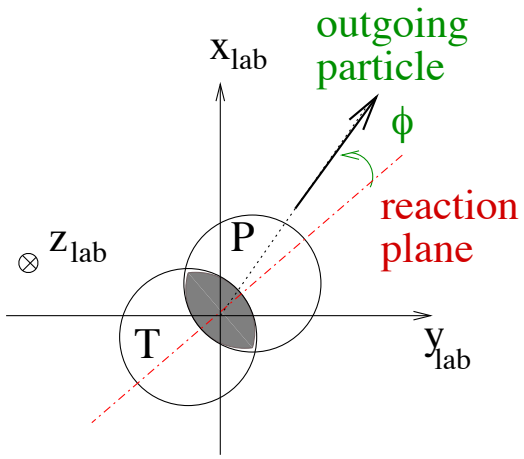

Figure 2.2: The reaction plane and the almond-shaped form of the collision zone. [11]

collision has a reaction plane, spanned by the beam axis and the orientation of the impact parameter b in the transverse plane. As a result, non-central collisions tend to have an almond-shaped area where the collision took place and therefore an asymmetric distribution in space remains (see figure 2.2). After a certain amount of time the asymmetry in space is transferred to momentum-space and is then also visible in the particle momentum distribution. [11]

There is a simple explanation for this behavior: A particle moving along the long axis of the collision zone has a larger probability to scatter and then change direction, compared to a particle along the short axis. The observed particle emission is azimuthal anisotropic and grows even more anisotropic the more rescattering occurs. The anisotropy serves as a measurement of the frequency of rescatterings during the dense expansion phase of a heavy-ion collision. [12, 13]

The next step is to characterize the momentum distribution as a function of the azimuthal angle ϕ with respect to the reaction plane angle ϕ_{RP}. The reaction plane is a crucial point in this process since it may change from collision to collision. Instead of ϕ the difference $\phi - \phi_{RP}$ seems more

fit to characterize the azimuthal dependence. Unfortunately, there is a downside to this description: In a heavy-ion collision the reaction plane cannot be measured and one has to find other options to measure the azimuthal angle. In a theoretical treatment it is possible to assume that the reaction plane does not change, which is used in this thesis.

In general there are two sources of azimuthal asymmetries: Statistical fluctuations and correlations within the reaction plane. While the first one should always be present even in the absence of a reaction plane, the second one manifests itself in form of collective behavior of the produced matter. The resulted anisotropy is quantified in terms of a Fourier expansion of the azimuthal distribution within the particle momentum distribution

$$E_{\vec{p}}\frac{d^3N}{d^3\vec{p}} = \frac{d^2N}{2\pi p_\perp dp_\perp dy}\left[1 + \sum_{n=1}^{\infty} 2v_n \cos(n(\phi - \phi_{RP}))\right], \tag{2.9}$$

where $d^3\vec{p}/E_{\vec{p}} = p_\perp dp_\perp dy d\phi$ with the transverse momentum $p_\perp$ and the momentum rapidity y. Only the even cosine part is kept, the odd sine part is zero due to the symmetry under $\phi \to -\phi$. [12]

The *flow coefficients* v_n are expressed as expectation values of the cosine from (2.9)

$$v_n = \langle \cos(n(\phi - \phi_{RP}))\rangle = \frac{\int_0^{2\pi} d\phi \frac{d^2N}{2\pi p_\perp dp_\perp dy} \cdot \cos(n(\phi - \phi_{RP}))}{\int_0^{2\pi} d\phi \frac{d^2N}{2\pi p_\perp dp_\perp dy}}. \tag{2.10}$$

In general the coefficients (2.10) may depend on the transverse momentum $p_\perp$ and the rapidity y and they can differ from particle species to particle species. At first, when the idea of collective flow was presented, it was common to neglect all v_n for odd n, since for identical particles in heavy-ion collisions at mid-rapidity ($y \approx 0$) the collision region is symmetric under $\phi \to -\phi$. Recently, more sources for anisotropic flow, like fluctuations, have been considered which result in non-vanishing terms for odd n. The individual v_n have different names which originate from the geometrical shape associated with the corresponding coefficient: v_1 is called the "direct flow", v_2 is the "elliptic flow", v_3 is the "triangular flow", and so on. A last remark: Non-vanishing flow coefficients may indicate that the created medium in heavy-ion collisions consists of interacting particles. If the collision would be only a superposition of independent collisions between different nucleons, no ϕ-distribution should be visible. [11]

2.3 Hanbury-Brown Twiss interferometry

This section covers the so called Hanbury-Brown and Twiss interferometry, more commonly known as *HBT-interferometry*. The HBT-interferometry is the correlation of identical particles, mainly pions, to get access to the size of the emitting source, in our case the heavy-ion collision. Originally, HBT-interformetry was invented for examining far away galactic sources, but it turned out to be a good measurement in relativistic heavy-ion collisions. However, what is the source in the case of a heavy-ion collision? It is common to assume that the source reflects the position of the pions when they freeze-out, this means when they scatter for the last time. [11]

The following derivation is taken from [10, p. 246-256], but the rather old but still complete article [14] by G. Baym serves also as a good source.

2.3.1 Time-independent correlation function

We start with the two-particle distribution $P_2(\vec{p}_1, \vec{p}_2)$, the one-particle distributions $P_1(\vec{p}_1)$ and $P_1(\vec{p}_2)$, and the correlation function $C(\vec{p}_1, \vec{p}_2)$ which are all related by

$$C(\vec{p}_1, \vec{p}_2) = \frac{P_2(\vec{p}_1, \vec{p}_2)}{P_1(\vec{p}_1) P_1(\vec{p}_2)} \tag{2.11}$$

The one- and two-particle distribution are directly related to the particle momentum distribution in section 2.2.1 by

$$P_1(\vec{p}_1) = E_{\vec{p}_1} \frac{d^3 N}{d^3 \vec{p}_1} \tag{2.12}$$

$$P_2(\vec{p}_1, \vec{p}_2) = E_{\vec{p}_1} E_{\vec{p}_2} \frac{d^6 N}{d^3 \vec{p}_1 d^3 \vec{p}_2}. \tag{2.13}$$

We assume that there are two pions at positions $\vec{x}_1$ and $\vec{x}_2$ randomly distributed in space and they have momenta $\vec{p}_1$ and $\vec{p}_2$, which are detected far away from the source of the pions. Furthermore, the source size is much smaller than the distance to the particle detectors. This means that the momentum of a particle seen at a detector does not depend on the position where it was emitted. The distribution of the positions is given by a density distribution $\rho(\vec{x})$. It is possible to express the two-particle

distribution as follows

$$P_2(\vec{p}_1,\vec{p}_2) = \int d^3\vec{x}_1 d^3\vec{x}_2\, \rho(\vec{x}_1)\rho(\vec{x}_2)\, |\Psi_{12}(\vec{p}_1,\vec{p}_2,\vec{x}_1,\vec{x}_2)|^2\,, \tag{2.14}$$

where Ψ_{12} is the symmetric wave function of the pions

$$\Psi_{12}(\vec{p}_1,\vec{p}_2,\vec{x}_1,\vec{x}_2) = \frac{1}{\sqrt{2}}\left(e^{i\vec{p}_1\cdot\vec{x}_1}e^{i\vec{p}_2\cdot\vec{x}_2} + e^{i\vec{p}_1\cdot\vec{x}_2}e^{i\vec{p}_2\cdot\vec{x}_1}\right). \tag{2.15}$$

For further proceedings we introduce two new variables, the relative momentum

$$\vec{q} \equiv \vec{p}_1 - \vec{p}_2 \tag{2.16}$$

and the center of mass momentum

$$\vec{k} \equiv \frac{1}{2}(\vec{p}_1 + \vec{p}_2). \tag{2.17}$$

With these two variables equation (2.15) is rewritten to

$$\Psi_{12}(\vec{k},\vec{q},\vec{x}_1,\vec{x}_2) = \frac{1}{\sqrt{2}} e^{i\vec{k}\cdot(\vec{x}_1+\vec{x}_2)}\left[e^{\frac{i}{2}\vec{q}\cdot(\vec{x}_1-\vec{x}_2)} + e^{-\frac{i}{2}\vec{q}\cdot(\vec{x}_1-\vec{x}_2)}\right], \tag{2.18}$$

which is further simplified to

$$\left|\Psi_{12}(\vec{k},\vec{q},\vec{x}_1,\vec{x}_2)\right|^2 = 1 + \frac{1}{2}\left[e^{i\vec{q}\cdot(\vec{x}_1-\vec{x}_2)} + e^{-i\vec{q}\cdot(\vec{x}_1-\vec{x}_2)}\right]. \tag{2.19}$$

This result leads to the final form of the two-particle distribution

$$\begin{aligned} P_2(\vec{k},\vec{q}) &= \int d^3\vec{x}_1 d^3\vec{x}_2\, \rho(\vec{x}_1)\rho(\vec{x}_2)\left[1 + \frac{1}{2}\left(e^{i\vec{q}\cdot(\vec{x}_1-\vec{x}_2)} + e^{-i\vec{q}\cdot(\vec{x}_1-\vec{x}_2)}\right)\right] \\ &= \int d^3\vec{x}_1\, \rho(\vec{x}_1) \int d^3\vec{x}_2\, \rho(\vec{x}_2) + \left|\int d^3\vec{x}\, \rho(\vec{x}) e^{-i\vec{q}\cdot\vec{x}}\right|^2. \end{aligned} \tag{2.20}$$

The one-particle distribution is obtained in a similar way as

$$P_1(\vec{p}) = \int d^3\vec{x}\, \rho(\vec{x}) \left|e^{i\vec{p}\cdot\vec{x}}\right|^2 = \int d^3\vec{x}\, \rho(\vec{x}), \tag{2.21}$$

which is independent of the momentum, reflecting the uncertainty relation. From the definition of the correlation function (2.11) the final result is

$$C(\vec{k},\vec{q}) = 1 + \frac{\left|\int d^3\vec{x}\, \rho(\vec{x}) e^{-i\vec{q}\cdot\vec{x}}\right|^2}{\left[\int d^3\vec{x}\, \rho(\vec{x})\right]^2}. \tag{2.22}$$

The correlation $C(\vec{k},\vec{q})$ is directly related to the Fourier transformation of the source density at the point $\vec{q}$. For small $\vec{q}$ the correlation function takes a value of 2.

2.3.2 The source function

The model from 2.3.1 is still rather simple and therefore it lacks an important feature: The time dependency of the pion source. This dependency is important for pion production since pions may be created close to each other but the time distance is large and therefore no correlation should be present. For a better description of the HBT-radii, we want to introduce the source function, also sometimes called the *emission function*. [10, p. 237]

The emission function is defined as follows

$$S(\mathsf{x}, \vec{p}) \equiv \int d\Sigma_\mu(\mathsf{x}')\, p^\mu \delta^{(4)}(\mathsf{x}' - \mathsf{x}) f(\mathsf{x}', \mathsf{p}). \tag{2.23}$$

The physical interpretation of the emission function is rather simple. The emission function gives the number of particles emitted in the phase-space element per unit time. If we integrate the emission function over space and time we achieve the particle momentum distribution (2.7)

$$\int d^4x\, S(\mathsf{x}, \vec{p}) = \int d\Sigma_\mu(\mathsf{x})\, p^\mu f(\mathsf{x}, \mathsf{p}) = E_{\vec{p}} \frac{d^3N}{d^3\vec{p}}. \tag{2.24}$$

The concept of the emission function is useful in the modeling of the physical conditions at the freeze-out, since it is in general not restricted to the hydrodynamical picture. The emission function is often used to compute particle spectra, but here we want to use it for HBT-interferometry and especially the HBT-radii.

To use the emission function we make an ansatz for the Fourier transformation of the density matrix $\varrho(\vec{p}_1, \vec{p}_2)$ depending on the source function

$$\varrho(\vec{p}_1, \vec{p}_2) = \varrho(\vec{k} + \frac{1}{2}\vec{q}, \vec{k} - \frac{1}{2}\vec{q}) = \int d^4x\, e^{iq_\mu x^\mu} S(\mathsf{x}, \vec{k}\,). \tag{2.25}$$

The momenta $\vec{k}$ and $\vec{q}$ are defined by the equations (2.17) and (2.16). To generalize equation (2.25) to full space-time integrals, we have to define k^0 and q^0 to achieve full four-momenta k^μ and q^μ. The most applicable way is to assume that the pions are on the mass shell which leads to the following definitions

$$k^0 = \frac{1}{2}\left(\sqrt{m^2 + \vec{p}_1^{\,2}} + \sqrt{m^2 + \vec{p}_2^{\,2}}\right) \tag{2.26}$$

$$q^0 = \sqrt{m^2 + \vec{p}_1^{\,2}} - \sqrt{m^2 + \vec{p}_2^{\,2}}. \tag{2.27}$$

With the density matrix and the relation (2.24) it is possible to rewrite the correlation function (2.11) to

$$\begin{aligned} C(\vec{p}_1,\vec{p}_2) &= 1 + \frac{|\varrho(\vec{p}_1,\vec{p}_2)|^2}{\varrho(\vec{p}_1,\vec{p}_1)\varrho(\vec{p}_2,\vec{p}_2)} \\ &= 1 + \frac{\left|\varrho(\vec{k}+\frac{1}{2}\vec{q},\vec{k}-\frac{1}{2}\vec{q})\right|^2}{\int d^4x\, S(\mathsf{x},\vec{p}_1)\int d^4y\, S(\mathsf{y},\vec{p}_2)} \\ &= 1 + \frac{\left|\int d^4x\, e^{iq_\mu x^\mu} S(\mathsf{x},\vec{k})\right|^2}{\int d^4x\, S(\mathsf{x},\vec{k}+\frac{1}{2}\vec{q})\int d^4y\, S(\mathsf{y},\vec{k}-\frac{1}{2}\vec{q})}, \end{aligned} \tag{2.28}$$

where the following relation of the source function to the density matrix was used

$$\varrho(\vec{p},\vec{p}) = E_{\vec{p}}\frac{d^3N}{d^3\vec{p}} = \int d^4x\, S(\mathsf{x},\vec{p}). \tag{2.29}$$

Very often the q-dependence of the denominator is neglected because it is assumed to be rather weak. This is called the smoothness approximation

$$S(\mathsf{x},\vec{k}+\frac{1}{2}\vec{q})S(\mathsf{y},\vec{k}-\frac{1}{2}\vec{q}) \approx S(\mathsf{x},\vec{k})\, S(\mathsf{y},\vec{k}). \tag{2.30}$$

Due to this approximation equation (2.28) is rewritten to

$$C(\vec{k},\vec{q}) = 1 + \frac{\left|\int d^4x\, e^{iq_\mu x^\mu} S(\mathsf{x},\vec{k})\right|^2}{\left|\int d^4x\, S(\mathsf{x},\vec{k})\right|^2}. \tag{2.31}$$

We conclude that the correlation function is the Fourier transformation of the emission function. The range of the correlation function is related to the space-time extension of the emitting source.

2.3.3 Computing the HBT-radii

In the final step we need to parameterize the emission function. Since there is no actual way to measure the emission function we have to choose one, for example a Gaussian function

$$S(\mathsf{x},\vec{k}) = N(\vec{k})e^{-\frac{1}{2}\widetilde{x}^\mu(\vec{k})B_{\mu\nu}(\vec{k})\widetilde{x}^\nu(\vec{k})}. \tag{2.32}$$

$N(\vec{k})$ is a normalization factor and the coordinates $\widetilde{x}^{\mu}(\vec{k})$ are deviations from the mean values $\overline{x}^{\mu}(\vec{k})$,

$$\widetilde{x}^{\mu}(\vec{k}) = x^{\mu} - \overline{x}^{\mu}(\vec{k}). \tag{2.33}$$

By performing a diagonalization of $B_{\mu\nu}(\vec{k})$, shown in [10, p. 250-252], it is possible to express the correlation function as

$$C(\vec{k}, \vec{q}) = 1 + e^{-q_{\mu}(B^{-1})^{\mu\nu}(\vec{k})q_{\nu}}. \tag{2.34}$$

One may also rewrite $(B^{-1})_{\mu\nu}(\vec{k})$ to $\langle \widetilde{x}_{\mu}\widetilde{x}_{\nu}\rangle(\vec{k})$ and therefore rewrite (2.34) to

$$C(\vec{k}, \vec{q}) = 1 + e^{-q^{\mu}q^{\nu}\langle \widetilde{x}_{\mu}\widetilde{x}_{\nu}\rangle(\vec{k})} \tag{2.35}$$

where the $\langle ... \rangle$ is an abbreviation for

$$\langle f \rangle = \frac{\int d^4x \, f(\mathsf{x}, \vec{k}) S(\mathsf{x}, \vec{k})}{\int d^4x \, S(\mathsf{x}, \vec{k})}. \tag{2.36}$$

We rewrite $q^{\mu}q^{\nu}\langle \widetilde{x}_{\mu}\widetilde{x}_{\nu}\rangle(\vec{k})$ to obtain the HBT-radii

$$\begin{aligned} q^{\mu}q^{\nu}\langle \widetilde{x}_{\mu}\widetilde{x}_{\nu}\rangle(\vec{k}) &= \sum_{i,j=1}^{3} q^i q^j \langle (\widetilde{x}^i - \beta^i \widetilde{t})(\widetilde{x}^j - \beta^j \widetilde{t})\rangle(\vec{k}) \\ &= \sum_{i,j=1}^{3} q^i q^j R^2_{ij}(\vec{k}), \end{aligned} \tag{2.37}$$

with $\beta^i = \frac{k^i}{k^0}$. The matrix $R^2_{ij}(\vec{k})$ is symmetric under permutation of i and j, therefore it only consists of six components and is further simplified by choosing the right coordinate system, the so called *Out-side-long-system*[2]. In this system the vector $\vec{k}$ is simplified to the pair momentum

$$\vec{k} = (k_{\perp}, 0, k_{\parallel}). \tag{2.38}$$

The z-axis coincides with the beam axis of the heavy-ion collision and determines the long-direction. In the transverse plane the x-axis is chosen parallel to the vector component of the momentum pair in (2.38), which

[2]Sometimes this coordinate system is called *Bertsch-Pratt-system*.

is transverse to the beam direction and therefore fixes the out-direction. The remaining y-axis determines the side-direction. The $R^2_{ij}(\vec{k})$ matrix consists of the following elements: The diagonal elements

$$R^2_{11}(\vec{k}) = R^2_{out}(\vec{k}) = \langle(\widetilde{x} - \beta_\perp \widetilde{t})^2\rangle(\vec{k}) \tag{2.39a}$$

$$R^2_{22}(\vec{k}) = R^2_{side}(\vec{k}) = \langle\widetilde{y}^2\rangle(\vec{k}) \tag{2.39b}$$

$$R^2_{33}(\vec{k}) = R^2_{long}(\vec{k}) = \langle(\widetilde{z} - \beta_\parallel \widetilde{t})^2\rangle(\vec{k}), \tag{2.39c}$$

and the off-diagonal elements

$$R^2_{12}(\vec{k}) = R^2_{out-side}(\vec{k}) = \langle(\widetilde{x} - \beta_\perp \widetilde{t})\widetilde{y}\rangle(\vec{k}) \tag{2.40a}$$

$$R^2_{23}(\vec{k}) = R^2_{side-long}(\vec{k}) = \langle\widetilde{y}(\widetilde{z} - \beta_\parallel \widetilde{t})\rangle(\vec{k}) \tag{2.40b}$$

$$R^2_{31}(\vec{k}) = R^2_{long-out}(\vec{k}) = \langle(\widetilde{z} - \beta_\parallel \widetilde{t})(\widetilde{x} - \beta_\perp \widetilde{t})\rangle(\vec{k}). \tag{2.40c}$$

In a cylindrically symmetric system $\widetilde{y}(\vec{k})$ is equal to zero because we have a reflection symmetry with respect to the side-direction, which means $y \to -y$. In this case all off-diagonal elements linear in $\widetilde{y}$ are equal to zero. Furthermore, if the system is boost-invariant, the off-diagonal element linear in $\widetilde{z}$ is also zero. Finally, in a longitudinally comoving system the momentum $k_\parallel$ vanishes and the remaining three matrix elements are

$$R^2_{out}(k_\perp) = \langle(\widetilde{x} - \beta_\perp \widetilde{t})^2\rangle(\vec{k}) \tag{2.41a}$$

$$R^2_{side}(k_\perp) = \langle\widetilde{y}^2\rangle(\vec{k}) \tag{2.41b}$$

$$R^2_{long}(k_\perp) = \langle\widetilde{z}^2\rangle(\vec{k}). \tag{2.41c}$$

These three matrix elements are commonly called the *HBT-radii* and are calculated with the help of equation (2.36). Moreover, the correlation function (2.34) is rewritten to

$$C(\vec{k}, \vec{q}) = 1 + e^{-R^2_{out}(k_\perp)q^2_{out} - R^2_{side}(k_\perp)q^2_{side} - R^2_{long}(k_\perp)q^2_{long}}. \tag{2.42}$$

With these final results we have all equations needed to calculate the desired observables, namely the particle momentum spectrum (2.7), the flow coefficients (2.10), and the HBT-radii (2.41).

Before the actual calculations we summarize in the next chapter the basic fields and equations of relativistic hydrodynamics. These results may not be needed explicitly, but they provide concepts and ideas necessary for the following chapters.

3 Relativistic hydrodynamics

The basic theory in this thesis is hydrodynamics. In this chapter we want to explain the fundamental concepts of relativistic hydrodynamics. We start with a short overview of a classical fluid and go on to relativistic hydrodynamics. For relativistic hydrodynamics we present general predications, but also take a look at perfect and dissipative relativistic fluids. The chapter is based on the lecture [15] by N. Borghini.

3.1 Classical fluid

Hydrodynamics is a *classical effective field theory* which describes a continuous medium like a fluid or a gas. This means that the theory discards any relativistic or quantum mechanical effects, uses averages over the microscopic degrees of freedom of the system and at every point in time and space assigns physical quantities a certain value.

We want to look closer at the aspects of an effective theory. Instead of looking at the real degrees of freedom of a physical system, we choose new degrees of freedom. In hydrodynamics this is done by averaging over particles in a certain volume V in space and choose the volume as the new particles of the system. This volume V is often called a *fluid-particle* and it has to fulfill two criteria. First, the fluid-particle has to be larger than the real particles of the system, for example elementary particles or atoms. The effect of many particles inside one fluid-particle is a reduction of the microscopic fluctuations of the physical quantities which are relevant for the system. Second, the fluid-particle has to be much smaller than the whole system we want to describe. Therefore, when looking at the whole system, the fluid-particles act as point-like particles.

If a system satisfies these conditions, it fulfills the following relation

$$\frac{l_{mfp}}{L} \ll 1. \tag{3.1}$$

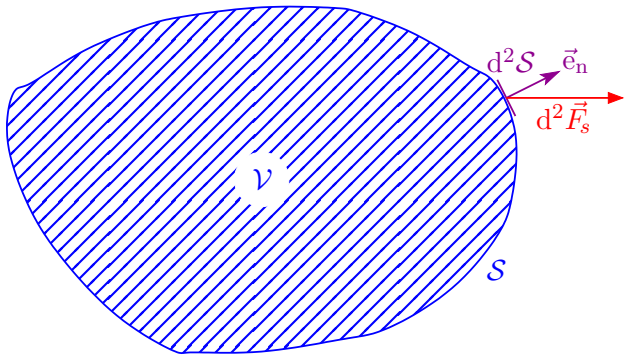

Figure 3.1: $d^2\mathcal{S}$ and $d^2\vec{F}_\mathcal{S}$ on the surface $\mathcal{S}$ of a volume $\mathcal{V}$. [15]

The fraction (3.1) is called the *Knudsen-number*. It consists of two length scales, the mean free path length l_{mfp} and the typical size of the system L. While the second length scale is self-explaining, the mean free path length is a measurement for the distance a particle travels until it interacts with another particle. If the Knudsen-number is much smaller than one, the particles in the system interact with each other almost certainly. A medium which fulfills the condition (3.1) is a *continuous medium*.

A continuous medium is further subclassified into solid state bodies and fluids. The two types differ in the response to external forces on them. Possible external forces are volume forces and surface forces. For example, volume forces are the weight force or long-range electromagnetic forces and surface forces are frictional forces. We define the mechanical stress tensor (see figure 3.1) as

$$\vec{T}_S \equiv \frac{d^2\vec{F}_\mathcal{S}}{d^2\mathcal{S}} \tag{3.2}$$

to classify the surface forces. It represents the surface density of contact forces on the surface $d^2\mathcal{S}$. The stress vector $\vec{T}_\mathcal{S}$ on a given surface element $d^2\mathcal{S}$ at a point P is decomposed into two components:

- a vector orthogonal to the tangent plane in P to $d^2\mathcal{S}$, called the normal stress. It is also referred to as compression or tension.
- a vector in the tangent plane in P, called the shear stress. It is often

denoted by $\vec{\tau}$.

With the help of the notion of mechanical stress, we define a *fluid*:

A fluid is a continuous medium that deforms itself as long as it is submitted to shear stress.

Or from another viewpoint: In a fluid at rest or in a reference frame with respect to which it is at rest, the mechanical stresses are necessarily all normal.

Fluids are described by several fields, while the field dynamics are obtained by rewriting conservation laws with the help of the Reynolds transport theorem

$$\frac{D\mathcal{G}(t)}{Dt} = \int_{\mathcal{V}} \frac{\partial}{\partial t} \left[g(t,\vec{r})\rho(t,\vec{r}) \right] d^3\vec{r} + \oint_{\mathcal{S}} \left[g(t,\vec{r})\rho(t,\vec{r})\vec{v}(t,\vec{r}\,] \cdot d^2\vec{\mathcal{S}}. \right. \quad (3.3)$$

The theorem states the following: The usual laws of dynamics are valid only for closed systems and not for open systems. Accordingly, these laws involve time derivatives which follow the system in its motion, the material derivative (substantial derivative) D/Dt. The Reynolds transport theorem (3.3) expresses the latter for extensive quantities $\mathcal{G}(t)$, in terms of local densities $g(t,\vec{r})$ attached to a fixed spatial position. $\mathcal{G}(t)$ and $g(t,\vec{r})$ are connected by the relation

$$g(t,\vec{r}) = \frac{d\mathcal{G}(t,\vec{r})}{dM(t,\vec{r})} \quad (3.4)$$

with $M(t,\vec{r})$ the mass inside the small material volume $\mathcal{V}$ at position $\vec{r}$ and time t.

Starting from the Reynolds transport theorem (3.3), several fields and their differential equations for common conservation laws are found. The most popular are the Euler equation for a perfect fluid and the Navier-Stokes equation for a dissipative fluid. The actual form of these equations is not important for this thesis. Instead we are moving directly to the basic concepts of relativistic hydrodynamics.

3.2 Relativistic hydrodynamics

A non-relativistic description can no longer be adapted if the energy density of the fluid becomes very large. This means that the participating particles in the fluid achieve very high kinetic energies comparable to the rest energy of the particles itself. Such behavior is found in the early universe or in relativistic heavy-ion collisions. Therefore it is necessary to adopt a relativistic description of fluids. In the same way as in the non-relativistic (classical) case, the fundamental equations describing the fluid in the relativistic regime are formulations of conservation laws for the particle number, energy, and momentum. For a more complete overview of relativistic hydrodynamics we refer to [8, chapter 3 and 6].

3.2.1 Basic equations

Particle number conservation

In a relativistic fluid the particle number is strictly speaking no longer conserved. Instead, due to the high energies, particle-antiparticle-pairs are created or annihilated and therefore the particle number is no longer a conservation quantity, even if the system is closed. But if the particles carry a conserved quantum number, for example electric charge, the difference of the quantum number between particles and antiparticles is conserved. In any creation or annihilation process the amount of the quantum number changes with $+1$, respectively -1, but the difference remains constant. This difference between particles and antiparticles is our new particle number and in a similar way we use particle number density and particle number flux which both refer to the difference of particles.

We consider a relativistic fluid consisting of a single species of particles, respectively antiparticles, both with mass m. Also, for simplicity, $(t, \vec{r})$ is replaced by (x). The *local particle number density* $n(\mathsf{x})$ is defined such that the product of $n(\mathsf{x})$ and the infinitesimal spatial volume element $d^3\vec{r}$ represents the total number of particles about position $\vec{r}$ at time t. Since the spatial element $d^3\vec{r}$ depends on the reference frame, this should also be the case for $n(\mathsf{x})$, such that the total particle number in $d^3\vec{r}$ remains independent of the reference frame. In a similar way, the *particle flux density* $\vec{j}_N(\mathsf{x})$ is defined as the number of particles that cross a unit surface

per unit time interval. Both, unit surface and unit time interval, are reference frame concepts.

The quantities $n(\mathsf{x})$ and $\vec{j}_N(\mathsf{x})$ are combined to the *particle number four-current* $\mathsf{N}(\mathsf{x})$

$$N^\mu(\mathsf{x}) = \begin{pmatrix} n(\mathsf{x}) \\ \vec{j}_N(\mathsf{x}) \end{pmatrix}. \tag{3.5}$$

The local formulation of the conservation of the particle number is

$$d_\mu N^\mu(\mathsf{x}) = 0 \tag{3.6}$$

where $d_\mu = \frac{d}{dx^\mu}$ denotes the components of the four-gradient[1].

Energy-momentum conservation

In a relativistic theory, energy and momentum are the time and space components of a four-vector, the *four-momentum* p. The local conservation of the four-momentum is expressed in form of densities and flux densities of energy and momentum at each point in space-time. Together they form the *energy-momentum tensor* $\mathsf{T}(\mathsf{x})$, a tensor of rank two, defined by the physical content of its components

- $T^{00}(\mathsf{x})$: the energy density
- $T^{0j}(\mathsf{x})$: the j-th component of the energy flux density $(j = 1, 2, 3)$
- $T^{i0}(\mathsf{x})$: the density of the i-th momentum component $(i = 1, 2, 3)$
- $T^{ij}(\mathsf{x})$: the momentum flux-density tensor $(i, j = 1, 2, 3)$.

All physical quantities are measured with respect to the reference frame. In the absence of external forces, the local conservation of the energy-momentum tensor is written as

$$d_\mu T^{\mu\nu}(\mathsf{x}) = 0 \;\; \forall\, \nu = 0, 1, 2, 3. \tag{3.7}$$

For $\nu = 0$ this is the conservation of energy, while for $j = 1, 2, 3$ we have momentum conservation for each component.

[1] In Minkowski-coordinates d_μ is replaced by the partial derivative $\partial_\mu = \frac{\partial}{\partial x^\mu}$.

3.2.2 Local rest frame and four-velocity

The *four-velocity* u of a fluid is a field defined at each point in space-time. Its vectors are time-like and fulfill

$$u_\mu(\mathsf{x})u^\mu(\mathsf{x}) = 1 \quad \forall \mathsf{x}. \tag{3.8}$$

At each point of the fluid, we define a proper reference frame, the so-called *local rest frame*, abbreviated as LR, in which the spatial components of the four-velocity vanish

$$u^\mu(\mathsf{x})\Big|_{LR} = (1, 0, 0, 0)\,. \tag{3.9}$$

Let $\vec{v}(\mathsf{x})$ denote the instantaneous velocity of (an observer at rest in) the local rest frame with respect to a fixed reference frame. In the latter, the components of the four-velocity are

$$u^\mu(\mathsf{x})\Big|_{R} = \begin{pmatrix} \gamma(\mathsf{x}) \\ \gamma(\mathsf{x})\vec{v}(\mathsf{x}) \end{pmatrix}, \tag{3.10}$$

where $\gamma(\mathsf{x})$ is the corresponding Lorentz factor

$$\gamma(\mathsf{x}) = \frac{1}{\sqrt{1 - \vec{v}(\mathsf{x})^2}}. \tag{3.11}$$

The local rest frame also represents the reference frame in which the local thermodynamic variables of the system, particle number density $\boldsymbol{n}(\mathsf{x})$ and energy density $\epsilon(\mathsf{x})$, are defined in their usual interpretation

$$\boldsymbol{n}(\mathsf{x}) \equiv n(\mathsf{x})\Big|_{LR}, \quad \epsilon(\mathsf{x}) \equiv T^{00}(\mathsf{x})\Big|_{LR}. \tag{3.12}$$

For the remaining local thermodynamic variables in the local rest frame it is assumed that they are related to $\boldsymbol{n}(\mathsf{x})$ and $\epsilon(\mathsf{x})$ in the same way, as when the fluid is at thermodynamic equilibrium.

3.3 Perfect relativistic fluid

A "perfect" fluid has no dissipative currents in itself, namely friction and heat flow. As a consequence we can find at each space-time point of the fluid a reference frame in which the local neighborhood of the given point is spatially isotropic. This reference frame represents the natural choice of the local rest frame. In this section we present the particle number four-current $N^\mu(x)$ and the energy-momentum tensor $T^{\mu\nu}(x)$ for a perfect fluid.

We adopt a cartesian coordinate system for the spatial directions in the local rest frame. This defines the spatial isotropy of the local fluid properties since the fluid characteristics are the same in all spatial directions. In such a system the local rest frame values of the i-th component of the particle number flux density $N^i(\mathsf{x})$, the j-th components of the energy flux density $T^{0j}(\mathsf{x})$ and the i-th component of the momentum density $T^{i0}(\mathsf{x})$ should all vanish. Also, the momentum flux density tensor $T^{ij}(\mathsf{x})$ should be diagonal. These conditions are expressed as

$$N^0(\mathsf{x})\Big|_{LR} = n(\mathsf{x}), \tag{3.13a}$$

$$N^i(\mathsf{x})\Big|_{LR} = 0 \quad \forall i = 1,2,3 \tag{3.13b}$$

$$T^{00}(\mathsf{x})\Big|_{LR} = \epsilon(\mathsf{x}), \tag{3.13c}$$

$$T^{ij}(\mathsf{x})\Big|_{LR} = \mathcal{P}(\mathsf{x})\delta^{ij}, \quad \forall i,j = 1,2,3 \tag{3.13d}$$

$$T^{i0}(\mathsf{x})\Big|_{LR} = T^{0j}(\mathsf{x})\Big|_{LR} = 0, \quad \forall i,j = 1,2,3 \tag{3.13e}$$

where the conditions in (3.12) are respected and $\mathcal{P}(\mathsf{x})$ denotes the pressure. The matrix form of the energy-momentum tensor is

$$T^{\mu\nu}(x)\Big|_{LR} = \begin{pmatrix} \epsilon(x) & 0 & 0 & 0 \\ 0 & \mathcal{P}(x) & 0 & 0 \\ 0 & 0 & \mathcal{P}(x) & 0 \\ 0 & 0 & 0 & \mathcal{P}(x) \end{pmatrix}. \tag{3.14}$$

In an arbitrary reference frame the components of the particle number four-current and energy-momentum tensor are

$$N^\mu(\mathsf{x}) = n(\mathsf{x})u^\mu(\mathsf{x}) \tag{3.15}$$
$$T^{\mu\nu}(\mathsf{x}) = [\epsilon(\mathsf{x}) + \mathcal{P}(\mathsf{x})]u^\mu(\mathsf{x})u^\nu(\mathsf{x}) - \mathcal{P}(\mathsf{x})g^{\mu\nu}(\mathsf{x}) \tag{3.16}$$

with $u^\mu(\mathsf{x})$ the components of the fluid four-velocity. $T^{\mu\nu}(\mathsf{x})$ in (3.16) can be rewritten as

$$T^{\mu\nu}(\mathsf{x}) = \epsilon(\mathsf{x})u^\mu(\mathsf{x})u^\nu(\mathsf{x}) + \mathcal{P}(\mathsf{x})\Delta^{\mu\nu}(\mathsf{x}). \tag{3.17}$$

$\Delta^{\mu\nu}(\mathsf{x})$ represents the components of a tensor which is a projector on the three-dimensional vector space orthogonal to the four-velocity $u^\mu(\mathsf{x})$

$$\Delta^{\mu\nu}(\mathsf{x}) = u^\mu(\mathsf{x})u^\nu(\mathsf{x}) - g^{\mu\nu}(\mathsf{x}). \tag{3.18}$$

On the other hand $u^\mu(\mathsf{x})u^\nu(\mathsf{x})$ is projecting on the time-like direction of the four-velocity.

3.4 Dissipative relativistic fluid

In a dissipative relativistic fluid, the transport of particle number and four-momentum is no longer only convective (caused by fluid motion), but may also be diffusive. The diffusive effects happen due to spatial gradients of the flow velocity field, the temperature, or the chemical potential(s) associated with the conserved particle number(s). A description of these new types of transport needs the introduction of additional terms in the particle number four-current and the energy-momentum tensor. These terms break the local isotropy of the fluid and therefore the local rest frame of the fluid is no longer uniquely.

3.4.1 Dissipative currents

Additional types of transport present in a dissipative fluid are accounted for by adding extra terms to the particle number four-current and the energy-momentum tensor. Denoting the quantities for a perfect fluid by a subscript 0, their equivalents in the dissipative case thus read

$$N^\mu(\mathsf{x}) = N_0^\mu(\mathsf{x}) + n^\mu(\mathsf{x}) \tag{3.19}$$
$$T^{\mu\nu}(\mathsf{x}) = T_0^{\mu\nu}(\mathsf{x}) + \tau^{\mu\nu}(\mathsf{x}) \tag{3.20}$$

with $n^\mu(\mathsf{x})$ components of a four-vector and $\tau^{\mu\nu}(\mathsf{x})$ components of a tensor of rank two. They represent a dissipative particle number four-current and a dissipative energy-momentum flux density.

In analogy to the perfect fluid, it is natural to introduce a four-velocity $u^\mu(\mathsf{x})$ in terms of which the quantities $N_0^\mu(\mathsf{x})$ and $T_0^{\mu\nu}(\mathsf{x})$ achieve a simple isotropic expression. Let $u^\mu(\mathsf{x})$ be an arbitrary time-like four-vector field respecting equation (3.8). The reference frame in which the spatial components of this four-velocity vanish will constitute the local rest frame associated with $u^\mu(\mathsf{x})$. The projector $\Delta^{\mu\nu}(\mathsf{x})$ on the three-dimensional vector space orthogonal to the four-velocity $u^\mu(x)$ is defined as in (3.18). Compared with (3.15) and (3.16) we write

$$N^\mu(\mathsf{x}) = n(\mathsf{x})u^\mu(\mathsf{x}) + n^\mu(\mathsf{x}) \tag{3.21}$$
$$T^{\mu\nu}(\mathsf{x}) = \epsilon(\mathsf{x})u^\mu(\mathsf{x})u^\nu(\mathsf{x}) + \mathcal{P}(\mathsf{x})\Delta^{\mu\nu}(\mathsf{x}) + \tau^{\mu\nu}(\mathsf{x}). \tag{3.22}$$

The physical content and mathematical form of the additional terms can be further specified.

Relations for $n^\mu(\mathsf{x})$ and $\tau^{\mu\nu}(\mathsf{x})$

In the local rest frame the following condition must hold

$$u_\mu(\mathsf{x})n^\mu(\mathsf{x})\Big|_{LR} = 0. \tag{3.23}$$

The left-hand side is a Lorentz scalar and therefore it should hold in any coordinate system

$$u_\mu(\mathsf{x})n^\mu(\mathsf{x}) = 0. \tag{3.24}$$

Physically $n^\mu(\mathsf{x})$ represents a *diffusive particle number four-current* in the local rest frame, which describes the non-convective transport of the particle number.

For the dissipative energy-momentum current $\tau^{\mu\nu}(\mathsf{x})$ we conclude that it has no 00-component in the local rest frame, to ensure that $T^{00}(\mathsf{x})$ in

that frame still defines the comoving energy density $\epsilon(\mathsf{x})$. Therefore, the components $\tau^{\mu\nu}(\mathsf{x})$ may not be proportional to the product $u^{\mu}(\mathsf{x})u^{\nu}(\mathsf{x})$. The most general symmetric tensor of rank two which obeys this condition has the form

$$\tau^{\mu\nu}(\mathsf{x}) = q^{\mu}(\mathsf{x})u^{\nu}(\mathsf{x}) + q^{\nu}(\mathsf{x})u^{\mu}(\mathsf{x}) + \pi^{\mu\nu}(\mathsf{x}) \tag{3.25}$$

with $q^{\mu}(\mathsf{x})$ the components of a four-vector and $\pi^{\mu\nu}(\mathsf{x})$ components of a tensor with rank two such that

$$u_{\mu}(\mathsf{x})q^{\mu}(\mathsf{x}) = 0 \tag{3.26}$$

$$u_{\mu}(\mathsf{x})\pi^{\mu\nu}(\mathsf{x})u_{\nu}(\mathsf{x}) = 0. \tag{3.27}$$

The condition (3.26) states that $q^{\mu}(\mathsf{x})$ is a four-vector orthogonal to the four-velocity $u^{\mu}(\mathsf{x})$. Its physical representation is the *heat current* or *energy flux current* in the local rest frame. On the other hand, $\pi^{\mu\nu}(\mathsf{x})$ contains all dissipative phenomena due to friction forces and is called *stress tensor*. Furthermore, $\pi^{\mu\nu}(\mathsf{x})$ is a symmetric tensor and is decomposed into the sum of a traceless tensor $\omega^{\mu\nu}(\mathsf{x})$ and a tensor proportional to the projector (3.18)

$$\pi^{\mu\nu}(\mathsf{x}) = \omega^{\mu\nu}(\mathsf{x}) + \Pi(\mathsf{x})\Delta^{\mu\nu}(\mathsf{x}). \tag{3.28}$$

The tensor $\omega^{\mu\nu}(\mathsf{x})$ is the *shear stress tensor* in the local rest frame of the fluid, that describes the transport of momentum due to shear deformations. Eventually, $\Pi(\mathsf{x})$ represents a *dissipative pressure* term, since it behaves like the thermodynamic pressure $\mathcal{P}(\mathsf{x})$. With these new fields, the energy-momentum tensor of a dissipative relativistic fluid is written as

$$\begin{aligned} T^{\mu\nu}(\mathsf{x}) = \epsilon(\mathsf{x})u^{\mu}(\mathsf{x})u^{\nu}(\mathsf{x}) + \left[\mathcal{P}(\mathsf{x}) + \Pi(\mathsf{x})\right]\Delta^{\mu\nu}(\mathsf{x}) \\ + q^{\mu}(\mathsf{x})u^{\nu}(\mathsf{x}) + q^{\nu}(\mathsf{x})u^{\mu}(\mathsf{x}) + \omega^{\mu\nu}(\mathsf{x}). \end{aligned} \tag{3.29}$$

3.4.2 Local rest frames

At a given point in a dissipative relativistic fluid, the particle number and the energy may flow in different directions. This happens in particular because particle-antiparticle pairs, which do not contribute to the particle density, still transport energy. Another possibility is that different conserved quantum numbers flow in different directions.

In general it is not possible to find a preferred reference frame in which the local properties of the fluid are isotropic. As a consequence, there is no unique natural choice for the four-velocity $u^\mu(\mathsf{x})$ of the fluid flow. On the contrary, several definitions of the four-velocity are possible, implying varying relations for the dissipative currents, although the described physics remain the same.

- A first natural possibility was proposed by C. Eckart [16]. The four-velocity is assumed proportional to the particle number four-current. Accordingly, the dissipative particle number flux $n^\mu(\mathsf{x})$ vanishes automatically and the expression of the particle number conservation is simpler with this choice. The local rest frame associated with this four-velocity is referred to as *Eckart frame*.

- Another natural definition of the four-velocity is that of L. D. Landau [17, p. 512-514]. The four-velocity is assumed to be proportional to the energy flux density. This choice determines the *Landau frame*, where the heat current $q^\mu(\mathsf{x})$ vanishes and the dissipative tensor $\tau^{\mu\nu}(\mathsf{x})$ is reduced to its viscous part $\pi^{\mu\nu}(\mathsf{x})$.

Eventually, one may choose to work with a general four-velocity and thus keep both the diffusive particle number current and the heat flux density in the dynamical fields.

3.4.3 First order dissipative relativistic fluid dynamics

The decompositions (3.21) and (3.29) are purely algebraic and do not imply anything regarding the physics of the fluid. Such assumptions involve two different elements: an equation of state, relating the energy density ϵ to the pressure $\mathcal{P}$ and the particle number n, and a constitute equation that models the dissipative effects, for example the diffusive particle number four-current $n^\mu(\mathsf{x})$, the heat flux density $q^\mu(\mathsf{x})$, and the dissipative stress tensor $\pi^{\mu\nu}(\mathsf{x})$.

Several approaches are possible to construct such constitutive equations. At first one could compute the particle number four-current and energy-momentum tensor starting from an underlying microscopic theory, in particular from a kinetic theory of the fluid constituents. Alternatively, one can work at the macroscopic level, using the various constraints applying to such. For example, the tensorial structure of the various currents

should be the correct one, or the second law of thermodynamics should be satisfied.

In the Landau frame the heat flux density $q^\mu(\mathsf{x})$ vanishes and the remaining constituents are written as[2]

$$\Pi(\mathsf{x}) = -\zeta(\mathsf{x})\nabla^\mu(\mathsf{x})u_\mu(\mathsf{x}) \tag{3.30}$$

$$\omega^{\mu\nu}(\mathsf{x}) = -\eta(\mathsf{x})\left[\nabla^\mu(\mathsf{x})u^\nu(\mathsf{x}) + \nabla^\nu(\mathsf{x})u^\mu(\mathsf{x}) - \frac{2}{3}\left[\nabla^\nu(\mathsf{x})u_\nu(\mathsf{x})\right]\right] \tag{3.31}$$

$$n^\mu(\mathsf{x}) = \kappa(\mathsf{x})\left[\frac{n(\mathsf{x})T(\mathsf{x})}{\epsilon(\mathsf{x}) + \mathcal{P}(\mathsf{x})}\right]^2 \nabla^\mu(\mathsf{x})\left[\frac{\mu(\mathsf{x})}{T(\mathsf{x})}\right] \tag{3.32}$$

for dissipative pressure, stress tensor, and particle number four-current. The new coefficients ζ, η, and κ are three positive numbers which depend on the space-time position implicitly and vary with temperature and chemical potential. The three coefficients are named after the dissipative phenomenon to which they contribute. ζ is the *bulk viscosity*, η is the *shear viscousity*, and κ is the *heat conductivity*. The constitutive equations (3.30), (3.31), and (3.32) only involve first order terms in the derivatives of velocity, temperature, or chemical potential. A theory constructed with such an ansatz is referred to as *first order dissipative fluid dynamics* which is the relativistic generalization of the set of laws valid for classical dissipative fluids.

However, the theory suffers from a severe issue which does not affect its non-relativistic counterpart. Many solutions of the first order dissipative fluid dynamics equations are unstable against small perturbations. Such disturbances grow exponentially with time on a typical microscopic time scale. As a result the velocity of given modes can quickly exceed the speed of light, which is of course unacceptable in a relativistic theory. Additionally, gradients also grow quickly, leading to a breakdown of the small-gradient assumption that underlies the construction of first order dissipative fluid dynamics. As a consequence, including dissipation in relativistic fluid dynamics necessitates going beyond a first order expansion in gradients. The most popular theory of the second order dissipative fluid dynamics is called Israel-Stewart-theory. Further insight regarding this theory can be found in [18]. For simplicity in this thesis we will remain with the first order dissipative fluid dynamics.

[2] We introduce the following notation: $\nabla^\mu(x) \equiv \Delta^{\mu\nu}(x)d_\nu$.

3.5 Boltzmann approach

The last section of this chapter shows a different approach to calculate the hydrodynamical fields (3.15) and (3.16) for a perfect fluid. This time we start from a *kinetic theory* description. This short overview is taken from [19, p. 10-12].

The starting point in a kinetic theory is the *relativistic Boltzmann equation*

$$p^\mu \partial_\mu f(\mathsf{x}, \mathsf{p}) = -C\left[f(\mathsf{x}, \mathsf{p})\right], \tag{3.33}$$

where $\mathsf{x} = (t, \vec{x})$, $\mathsf{p} = (E_{\vec{p}}, \vec{p})$[3] and $\partial_\mu = (\partial_t, -\vec{\nabla})$. The function $f(\mathsf{x}, \mathsf{p})$ is the (one-particle) distribution function of the fluid particles and the functional C is the so called *collision integral* which includes interactions between the particles of the fluid. To obtain the fields from section 3.3, we take the first two moments (zeroth and first) of the Boltzmann equation, which we achieve by multiplying both sides of (3.33) with the following integral operator

$$I^{\mu_1 \mu_2 \dots \mu_n} = \int dP \prod_{i=1}^{n} p_i^\mu \tag{3.34}$$

with $dP \propto d^3\vec{p}/E_{\vec{p}} = d^3\vec{p}/(2\pi)^3 p_0$ the Lorentz invariant phase-space element.

For the zeroth moment ($n = 0$) we obtain by partial integration

$$\begin{aligned} \int dP\, p^\mu \partial_\mu f(\mathsf{x}, \mathsf{p}) &= -\int dP\, C\left[f(\mathsf{x}, \mathsf{p})\right] \\ \partial_\mu \int dP\, p^\mu f(\mathsf{x}, \mathsf{p}) &= \int dP\, C\left[f(\mathsf{x}, \mathsf{p})\right]. \end{aligned} \tag{3.35}$$

The right side of (3.35) is generalized by the n-th moment of the collision integral $C_n \equiv \int dP \prod_{i=1}^{n} p_i^\mu C\left[f(\mathsf{x}, \mathsf{p})\right]$. The integral on the left side of (3.35) represents the known particle number four-current N in a different component form

$$N^\mu(\mathsf{x}, \mathsf{p}) = \int dP\, p^\mu f(\mathsf{x}, \mathsf{p}). \tag{3.36}$$

This allows us to write (3.35) in a more compact form

$$\partial_\mu N^\mu = C_0. \tag{3.37}$$

[3] Note that we restrict ourself to on-shell particles. For a more general formalism $E_{\vec{p}}$ should be replaced by p^0.

If the (effective) particle number is conserved, C_0 has to be zero and we find the already known equation (3.6).

For the first moment ($n = 1$) we achieve from (3.33)

$$\int dP\, p^\nu p^\mu \partial_\mu f(\mathsf{x}, \mathsf{p}) = -C_1$$
$$\partial_\mu \int dP\, p^\nu p^\mu f(\mathsf{x}, \mathsf{p}) = C_1. \tag{3.38}$$

On the left side, the energy-momentum tensor in its component form $T^{\mu\nu}$ is found

$$T^{\mu\nu} = \int dP\, p^\mu p^\nu f(\mathsf{x}, \mathsf{p}) \tag{3.39}$$

and the equation (3.38) is simplified to

$$\partial_\mu T^{\mu\nu} = C_1. \tag{3.40}$$

C_1 vanishes in case of energy-momentum conservation, leading to the known formula (3.7).

It is easy to extend the equations above in the case of dissipative hydrodynamics, which is shortly presented for the energy-momentum tensor. The energy-momentum tensor for a dissipative fluid is written as in (3.20) and the distribution function $f(\mathsf{x}, \mathsf{p})$ is assumed to be

$$f(\mathsf{x}, \mathsf{p}) = f_0(\mathsf{x}, \mathsf{p}) + \delta f(\mathsf{x}, \mathsf{p}), \tag{3.41}$$

where $f_0(\mathsf{x}, \mathsf{p})$ the distribution function for a perfect fluid and $\delta f(\mathsf{x}, \mathsf{p})$ dissipative corrections to f_0. In the next step, (3.41) is inserted into (3.39)

$$T^{\mu\nu} = \int dP\, p^\mu p^\nu f_0(\mathsf{x}, \mathsf{p}) + \int dP\, p^\mu p^\nu \delta f(\mathsf{x}, \mathsf{p})$$
$$= T_0^{\mu\nu} + \int dP\, p^\mu p^\nu \delta f(\mathsf{x}, \mathsf{p}). \tag{3.42}$$

From this result we deduce that $\tau^{\mu\nu}$ is

$$\tau^{\mu\nu} = \int dP\, p^\mu p^\nu \delta f(\mathsf{x}, \mathsf{p}). \tag{3.43}$$

This concludes the chapter about hydrodynamics. From now on we use the information from this chapter to calculate observables at the freeze-out.

4 Freeze-out of a perfect fluid

In section 2.1 we explained that during the expansion of the fireball the mean free path length gets smaller and smaller, until the fireball thermalizes. This leads to an isentropic collision-dominated phase, which can be described by perfect hydrodynamics. In the later stages the collisions cease until the expansion becomes collision-free. Between these two stages, hydrodynamics and free expansion, a transition has to take place. The transition should be modeled by a transport theory to account both important aspects of the process, the isentropic and the collision-less limits.

This chapter is a short summary of an article by N. Borghini and J.-Y. Ollitrault written in 2006 [6]. In the article a rather simple ansatz for the transition was chosen, the *sudden freeze-out approximation*. The approximation involves the already presented Cooper-Frye method from section 2.2.1.

4.1 Ansatz for the Cooper-Frye formula

The particle momentum distribution is calculated with the following form of the Cooper-Frye formula

$$E_{\vec{p}}\frac{d^3N}{d^3\vec{p}} = C\int_\Sigma d\sigma_\mu(\mathsf{x})\, p^\mu \exp\left(-\frac{p^\mu u_\mu(\mathsf{x})}{T}\right), \tag{4.1}$$

where Σ is a given space-time hypersurface along the history of the fluid. It is also the surface where the transition should take place, therefore at each point of Σ free-streaming particles are emitted, accordingly to the known thermal distribution (2.8) in the rest frame. For simplicity, quantum mechanical effects are neglected and as a result the thermal distribution is equal to the *Maxwell-Jüttner distribution*, the relativistic form of the Maxwell-Boltzmann distribution. A further simplification is to set the temperature T, also called *freeze-out temperature*, as a constant everywhere on the surface Σ. All possible normalization factors have been

grouped together to the normalization constant C. The perfect hydrodynamics are represented by the fluid four-velocity $\mathsf{u}(\mathsf{x})$ at space-time point[1] x on Σ.

It is assumed that the approximation gives poor results for observables, which depend on the detailed physics at the freeze-out, like the HBT-radii. On the other hand it should give reasonable results for single-particle spectra, like the anisotropic flow, if the collective expansion dominates over random thermal motion.

4.2 Method of steepest descent

The general idea to solve the integral over Σ in equation (4.1) in the limit of small T is to apply the *method of steepest descent*, also known as saddle point integration. The dominant contribution comes from points where the energy of the particles in the fluid frame E_{FF} is at minimum. For a given p, E_{FF} is a function of the spatial components of u, which themselves depend on the space-time point x on Σ. Here E_{FF} is equal to $p^\mu u_\mu$. The component u^0 is related to the spatial components via $u^0 = \sqrt{1+\vec{u}^{\,2}}$, since u has to fulfill condition (3.8). The absolute minimum of E_{FF} is the particle mass m, which is reached if the particles are at rest with respect to the fluid. This absolute minimum occurs only if a point on Σ exists where this value of the fluid velocity is reached.

The values taken by the longitudinal velocity of the fluid along the beam axis span the whole range in relativistic heavy-ion collisions, while the transverse velocity perpendicular to the beam axis is limited to a certain range. This behavior is explained by the absence of the transverse part of the flow in the beginning of the collision, which only builds up in the progress of the expansion. For a given fluid rapidity y, which depends on the longitudinal fluid velocity u^z and the component u^0, the transverse velocity $u_t = \sqrt{(u^x)^2 + (u^y)^2}$ extends up to a maximum value u_{max}. The value u_{max} may depend on y and the azimuthal angle ϕ for non-central collisions and is largest along the direction of the impact parameter ($\phi = 0$) due to larger pressure gradients in this direction.

[1] For simplicity the x-dependence will be dropped in this chapter.

4.3 Slow and fast particles

From now on the following distinction is made: a particle of mass m, rapidity y and transverse momentum p_t is considered to be a *slow particle* if $p_t/m < u_{max}(y,\phi)$ for all ϕ (actually for $\phi = \pi/2$, where the minimum occurs)[2]. Conversely, a *fast particle* is defined by $p_t/m > u_{max}(y,\phi)$ for all ϕ (this is for $\phi = 0$, where the velocity is at its maximum). Between both particle regimes should be a small intermediate region, which is neglected in the article.

Slow particles

For a slow particle, there is a point x on Σ where the fluid velocity is the same as the particle velocity and the minimum $p^\mu u_\mu = m$ is reached. If the freeze-out temperature T is small enough, the dominant contributions to (4.1) come from the neighborhood of the point x. The integral is evaluated approximatively by expanding the exponent around the minimum to second order. This results in a Gaussian integral. For a given velocity, the four-momentum is proportional to the particle mass. The width of the Gaussian varies with $\sqrt{m}$ and the integral over Σ in (4.1) is proportional to $\sqrt{m}^3$ times a function of the particle velocity. The result has a mass dependence only as a global factor for slow particles

$$E_{\vec{p}}\frac{d^3N}{d^3\vec{p}} = \frac{d^3N}{p_t dp_t\, d\phi\, dy} = c(m)F\left(\frac{p_t}{m}, y, \phi\right), \tag{4.2}$$

where F is the same function for all particles. The transverse momentum and rapidity spectra of slow particles coincide up to a normalization factor, if they are plotted as a function of p_t/m and y. The flow coefficients $v_n = \langle\cos(n\phi)\rangle$, which are independent of the total yield, should also coincide for different slow particles with the same p_t/m and y.

Fast particles

For particles that move faster than the fluid, the fast particles, the minimum value of $p^\mu u_\mu$ is larger than m. To locate this minimum, one denotes

[2] Keep in mind, that p_t is the momentum of the particles and $u_{max}(y,\phi)$ is the maximum value of the fluid velocity.

the particle rapidity as y and the fluid particle rapidity as y_f, the transverse component of $\vec{u}$ parallel to the particle transverse momentum $\vec{\mathbf{p}}_\mathbf{t}$ as $u_\parallel$ and the transverse component of $\vec{u}$ orthogonal to $\vec{\mathbf{p}}_\mathbf{t}$ as $u_\perp$. With these notations $p^\mu u_\mu$ is written as

$$p^\mu u_\mu = m_t \cosh(y - y_f)\sqrt{1 + u_\parallel^2 + u_\perp^2} - p_t u_\parallel \tag{4.3}$$

where $m_t = \sqrt{m^2 + p_t^2}$ is the transverse mass. The minimum of (4.3) with respect to y_f and $u_\perp$ is given by $y_f = y$ and $u_\perp = 0$, implying that the fluid velocity is parallel to the particle velocity. For $u_\parallel$ the minimum is attained for $u_\parallel = u_{max}(y, \phi)$. Fast particles come from regions on Σ where the parallel velocity is close to its maximum value. Depending on the point of Σ, the saddle-point integration results in[3]

$$\frac{d^3N}{p_t dp_t\, d\phi\, dy} \propto \frac{1}{\sqrt{p_t - m_t v_{max}}} \exp\left(\frac{p_t u_{max} - m_t u^0_{max}}{T}\right), \tag{4.4}$$

where we introduced v_{max} defined as

$$v_{max} \equiv \frac{u_{max}}{\sqrt{1 + u_{max}^2}}. \tag{4.5}$$

The y- and ϕ-dependence of u_{max} is implicit. The transverse momentum spectrum of the particles is directly obtained from equation (4.4) by neglecting the y- and ϕ-dependence of u_{max}. Radial flow results in flatter m_t-spectra for heavier particles and also implies a breakdown of the m_t-scaling.

4.4 Flow coefficients

For non-central collisions the flow coefficients are obtained from equation (4.4) by expanding u_{max} in a Fourier series while neglecting the rapidity y and the odd harmonics

$$u_{max}(\phi) = u_{max}(1 + 2V_2 \cos(2\phi) + 2V_4 \cos(4\phi) + ...). \tag{4.6}$$

[3] It is assumed, that the maximum u_{max} is reached at an inner point of Σ. If the maximum is reached at the edge, there is no square root in the prefactor.

The ϕ-distribution is gained by inserting (4.6) into (4.4). If T is small enough, the ϕ-dependence in (4.4) is dominated by the exponential function. Expanding the latter to first order in V_2, respectively in $\cos(2\phi)$, one obtains the elliptic flow

$$v_2(p_t) = \frac{V_2 u_{max}}{T}(p_t - m_t v_{max}). \tag{4.7}$$

In particular, equation (4.7) shows that the mass ordering, following from equation (4.2) for slow particles, persists at high p_t in perfect hydrodynamics. At a given p_t, heavier particles have smaller $v_2(p_t)$.

Furthermore, the hexadecupole flow $v_4(p_t)$ is calculated by expanding (4.4) and looking for terms up to $\cos(4\phi)$ in leading order. Two terms arise

$$v_4(p_t) = \frac{V_4 u_{max}}{T}(p_t - m_t v_{max}) + \frac{(V_2 u_{max})^2}{2T^2}(p_t - m_t v_{max})^2. \tag{4.8}$$

If p_t is large enough, the first term can be neglected against the second term and the following simple relation is acquired

$$v_4(p_t) = \frac{v_2(p_t)^2}{2}. \tag{4.9}$$

The result for $v_4(p_t)$ in equation (4.8), respectively (4.9), is a contradiction to the assumption of a probe sensitive to the initial conditions. If $v_4(p_t)$ would be a sensitive probe, it should not depend on $v_2(p_t)$. On the other hand, a universal result is found which is directly used to probe the perfect fluid behavior. Deviations from this behavior are generally expected to yield a higher value for $v_4(p_t)$.

All these results can be used as signatures of hydrodynamical evolution in relativistic heavy-ion collisions and consistency checks of numerical fluid calculations. Some results for fast particles have already been known from blast-wave model calculations, but the results of N. Borghini and J.-Y. Ollitrault are more general.

In the next chapter the calculations from [6] are expanded to the case of a dissipative fluid.

5 Dissipative corrections to the freeze-out

Dissipative phenomena enter the freeze-out description in two possible ways. First, the whole evolution process is changed, which is accounted for by the fluid velocity obeying equations of dissipative relativistic hydrodynamics, namely the relativistic Navier-Stokes equation or second order equations [13]. This necessitates knowledge of the temperature dependence of the transport coefficients over the history of the fireball. Secondly, dissipation changes the endpoint of the fluid evolution, namely the transition from a continuous medium to individual particles. This process is modeled again by the sudden freeze-out approximation, with the help of the Cooper-Frye prescription.

We use the following form of the Cooper-Frye formula, which is similar to (4.1)

$$E_{\vec{p}}\frac{d^3N}{d^3\vec{p}} = \frac{g}{(2\pi)^3}\int_\Sigma d\sigma_\mu(\mathsf{x})\, p^\mu f\left(\frac{p^\mu u_\mu(\mathsf{x})}{T}\right), \tag{5.1}$$

with Σ the freeze-out hypersurface, g the degeneracy factor of the particles and f the phase-space distribution, which depends on the particle type (bosons or fermions) and dissipative properties of the fluid. Like in chapter 4, f is given by the Bose-Einstein, Fermi-Dirac, or the Maxwell-Jüttner distribution. Again, quantum effects are neglected and the Maxwell-Jüttner distribution denoted by f_0 is used

$$f_0(p^\mu u_\mu(\mathsf{x})) \propto \exp\left(-\frac{p^\mu u_\mu \mathsf{x}}{T}\right). \tag{5.2}$$

If the fluid is dissipative, f in equation (5.1) contains extra terms to ensure the continuity of the energy-momentum tensor (3.29) at decoupling. These corrections have been calculated in the case of a transition to a single component Boltzmann gas for a fluid with finite shear viscosity [20] or bulk viscosity [21], or a conformal fluid obeying second order dissipative

hydrodynamics [22]. However, it has been recognized that more realistic corrections are needed, some have been computed in [23–28]. Also, there have been attempts to constrain them from available experimental data in [29].

Here, we wish to pursue this approach and investigate whether the functional form of the dissipative corrections to the phase-space distribution f at the end of the hydrodynamical evolution (the particle momentum distribution) can be reconstructed from the shape of the flow coefficients. This is done by following the basic ideas of [6].

The content of this chapter has also been published in the following article: [30].

5.1 Saddle point approximation

Similar to [6], we do not assume a specific flow profile (Bjorken flow or blast-wave model) as in previous analytical studies. We bypass the knowledge of the freeze-out surface in the Cooper-Frye prescription by approximating the integral with the method of steepest descent (saddle point approximation). Naturally, the trade-off for the approximation is a restriction to the range of validity of our results, which should only hold in a certain transverse momentum interval and for some observables.

Most models[1] analyzed so far, take the one-particle distribution function at decoupling as follows

$$f(\mathsf{x},\mathsf{p}) = [1+\delta f(\mathsf{x},\mathsf{p})]\, f_0\left(\frac{p^\mu u_\mu(\mathsf{x})}{T}\right). \tag{5.3}$$

Dissipative effects contribute to an additional term proportional to the equilibrium distribution f_0 in addition to the modified velocity profile $\mathsf{u}(\mathsf{x})$. For the sake of consistency, the modulus of δf should be smaller than one. We shall adopt the ansatz (5.3) and use the condition $|\delta f| \ll 1$ to replace the actual saddle point of the integrand in equation (5.1), corresponding to f, by the saddle point obtained with f_0 only[2]. The changes introduced by this simplification are of second order in the small parameters, which are controlling δf. Since we consider the regime of not too small momenta,

[1] An exception is [26].

[2] For simplicity the x-dependence is dropped again in this section.

where f_0 is given by the Maxwell-Jüttner distribution (5.2), the saddle point is the point on the freeze-out surface where $p^\mu u_\mu$ is at its minimum.

For a longitudinal motion, the saddle point method selects regions of the fluid with the same rapidity y_f as the rapidity y of emitted particles. Regarding the transverse motion, a particle with an azimuthal angle φ is stemming from a fluid cell with transverse velocity $\vec{\mathbf{u}}_\mathbf{t}$ pointing along φ. For further specifications, we introduce the maximum value $u_{max}(y, \varphi)$ of $\vec{\mathbf{u}}_\mathbf{t}$ for a fixed rapidity y and azimuth φ. Depending on the transverse velocity p_t/m of the particle being smaller or bigger than $u_{max}(y, \varphi)$ one defines again slow particles and fast particles. The slow particles are emitted by regions with respect to which they are at rest, such that $\vec{\mathbf{u}}_\mathbf{t} = \vec{\mathbf{p}}_\mathbf{t}/m$. For fast particles, they are emitted from where the fluid velocity reaches its maximum $u_{max}(y, \varphi)$.

5.1.1 Minimization

Let $\vec{\mathbf{p}}_\mathbf{t}$ and y be the transverse momentum and longitudinal rapidity of an emitted particle with mass m in a proper reference frame and transverse mass $m_t = \sqrt{m^2 + (\vec{\mathbf{p}}_\mathbf{t})^2}$. Furthermore, $\vec{\mathbf{u}}_\mathbf{t}$ and y_f denote the transverse velocity and longitudinal rapidity of the fluid. The time-like component of the fluid velocity is given by $u^0 = \tilde{u}_t \cosh(y_f)$, with $\tilde{u}_t = \sqrt{1 + (\vec{\mathbf{u}}_\mathbf{t})^2}$ following directly from the normalization of u in equation (3.8),

$$u^\mu = (\tilde{u}_t \cosh(y_f),\, \vec{\mathbf{u}}_\mathbf{t},\, \tilde{u}_t \sinh(y_f)) \tag{5.4}$$

$$\begin{aligned} u^\mu u_\mu &= (\tilde{u}_t)^2 \cosh^2(y_f) - (\tilde{u}_t)^2 \sinh^2(y_f) - (\vec{\mathbf{u}}_\mathbf{t})^2 \\ &= (\tilde{u}_t)^2 - (\vec{\mathbf{u}}_\mathbf{t})^2 = 1 \\ &\Rightarrow (\tilde{u}_t)^2 = 1 + (\vec{\mathbf{u}}_\mathbf{t})^2 \Leftrightarrow \tilde{u}_t = \sqrt{1 + (\vec{\mathbf{u}}_\mathbf{t})^2}. \end{aligned} \tag{5.5}$$

Eventually, φ and φ_f are the azimuthal angles of the particle transverse momentum and fluid transverse velocity. With these information we find that p is

$$p^\mu = (m_t \cosh(y),\, \vec{\mathbf{p}}_\mathbf{t},\, m_t \sinh(y))$$

due to $\mathsf{p}^2 = m^2$ and that $p^\mu u_\mu$ in the exponent of (5.2) is written as follows

$$\begin{aligned} p^\mu u_\mu &= m_t \sqrt{1 + (\vec{\mathbf{u}}_\mathbf{t})^2}(\cosh(y)\cosh(y_f) - \sinh(y)\sinh(y_f)) - \vec{\mathbf{p}}_\mathbf{t} \cdot \vec{\mathbf{u}}_\mathbf{t} \\ &= m_t \sqrt{1 + (\vec{\mathbf{u}}_\mathbf{t})^2}\cosh(y - y_f) - \vec{\mathbf{p}}_\mathbf{t} \cdot \vec{\mathbf{u}}_\mathbf{t} \\ &= m_t \sqrt{1 + (u_t)^2}\cosh(y - y_f) - p_t u_t \cos(\varphi - \varphi_f) \end{aligned} \tag{5.6}$$

with $p_t = |\vec{\mathbf{p}}_\mathbf{t}|$ and $u_t = |\vec{\mathbf{u}}_\mathbf{t}|$.

We introduce the transverse rapidity $y_{f,t}$ of the fluid, which is defined through $u_t = \sinh(y_{f,t})$, as well as, the transverse rapidity y_t of the particle, which obeys $m_t = m\cosh(y_t)$ and $p_t = m\sinh(y_t)$. With the help of $y_{f,t}$ and y_t, the product (5.6) is written as

$$\begin{aligned} p^\mu u_\mu = m\cosh(y_t)\cosh(y_{f,t})\cosh(y - y_f) \\ - m\sinh(y_t)\sinh(y_{f,t})\cos(\varphi - \varphi_f). \end{aligned} \tag{5.7}$$

Minimizing (5.7) with respect to y_f and φ_f gives the conditions

$$y_f = y \tag{5.8a}$$

$$\varphi_f = \varphi. \tag{5.8b}$$

The first result (5.8a) indicates that the time and longitudinal components of the particle four-momentum and the four-velocity of the fluid obey $p^z/p^0 = u^z/u^0 = \tanh(y)$ at the points of the freeze-out surface, where the minimum is reached. On the other hand, (5.8b) suggests that the transverse components of the particle four-momentum and the four-velocity of the fluid are parallel at the corresponding points. Further computations yield the second derivatives of (5.7) with respect to y_f and φ_f at the minimum

$$\left.\frac{\partial^2(p^\mu u_\mu)}{\partial y_f^2}\right|_{min} = m\cosh(y_t)\cosh(y_{f,t}) \tag{5.9a}$$

$$\left.\frac{\partial^2(p^\mu u_\mu)}{\partial \varphi_f^2}\right|_{min} = m\sinh(y_t)\sinh(y_{f,t}). \tag{5.9b}$$

At the minimum the product (5.7) is rewritten to

$$\begin{aligned} p^\mu u_\mu &= m\cosh(y_t)\cosh(y_{f,t}) - m\sinh(y_t)\sinh(y_{f,t}) \\ &= m\cosh(y_t - y_{f,t}) \end{aligned} \tag{5.10}$$

which reaches its absolute minimum for $y_{f,t} = y_t$.

Instead of characterizing the transverse components through transverse rapidity and azimuthal angle, it is possible to adopt the same choice as in [6]. The components of the transverse fluid velocity are parallel and orthogonal to the transverse momentum $\vec{\mathbf{p}}_\mathbf{t}$ of the emitted particle, denoted by $u_\parallel$ and $u_\perp$. If this coordinate system is chosen, (5.6) is rewritten to

$$p^\mu u_\mu = m_t \sqrt{1 + u_\parallel^2 + u_\perp^2} \cosh(y - y_f) - p_t u_\parallel. \tag{5.11}$$

Again, minimizing (5.11) with respect to y_f and $u_\perp$ gives the results

$$y_f = y \tag{5.12a}$$
$$u_\perp = 0, \tag{5.12b}$$

which are equivalent to the conditions (5.8a) and (5.8b). Equation (5.11) at its minimum is expressed as

$$p^\mu u_\mu = m_t \sqrt{1 + u_\parallel^2} - p_t u_\parallel. \tag{5.13}$$

The absolute minimum of (5.13) is reached when $v_\parallel \equiv u_\parallel / \sqrt{1 + u_\parallel^2}$ is as close as possible to p_t/m_t. The second derivatives of (5.11) with respect to y_f and $u_\perp$ at the minimum are

$$\left.\frac{\partial^2 (p^\mu u_\mu)}{\partial y_f^2}\right|_{min} = m_t \sqrt{1 + u_\parallel^2} \tag{5.14a}$$
$$\left.\frac{\partial^2 (p^\mu u_\mu)}{\partial \varphi_f^2}\right|_{min} = \frac{m_t}{\sqrt{1 + u_\parallel^2}}. \tag{5.14b}$$

For further calculations we distinguish between slow and fast particles, as seen in section 4.3.

5.1.2 Slow particles

A point on the freeze-out surface with $y_{f,t} = y_t$ defines in the terminology of [6] a slow particle and gives the minimum of $p^\mu u_\mu$, which is simply m

(see equation (5.10)). This determines the saddle point x_{sp} of the Cooper-Frye integral. The condition $y_{f,t} = y_t$ together with (5.8a) and (5.8b) are equivalent to the already known relation at the saddle point

$$p^\mu u_\mu(\mathsf{x}_{sp}) = m. \tag{5.15}$$

The non-vanishing second derivatives at the saddle point are

$$\left.\frac{\partial^2(p^\mu u_\mu)}{\partial y_f^2}\right|_{min} = m\cosh^2 y_t = \frac{m_t^2}{m} \tag{5.16a}$$

$$\left.\frac{\partial^2(p^\mu u_\mu)}{\partial \varphi_f^2}\right|_{min} = m\sinh^2 y_t = \frac{p_t^2}{m} \tag{5.16b}$$

$$\left.\frac{\partial^2(p^\mu u_\mu)}{\partial y_{f,t}^2}\right|_{min} = m. \tag{5.16c}$$

Equivalently, in the $\vec{\mathbf{p}}_\mathbf{t}$-attached coordinate system[3] with $u_\perp$ and $u_\parallel$, the condition $y_{f,t} = y_t$ becomes $u_\parallel = p_t/m$ and the second derivatives are

$$\left.\frac{\partial^2(p^\mu u_\mu)}{\partial y_f^2}\right|_{min} = \frac{m_t^2}{m} \tag{5.17a}$$

$$\left.\frac{\partial^2(p^\mu u_\mu)}{\partial u_\perp^2}\right|_{min} = m \tag{5.17b}$$

$$\left.\frac{\partial^2(p^\mu u_\mu)}{\partial u_\parallel^2}\right|_{min} = \frac{m^3}{m_t^2}. \tag{5.17c}$$

The validity of the saddle point approximation is ensured, if the higher order terms in the Taylor expansion of $(p^\mu u_\mu)/T$ are negligible compared to the quadratic terms. Considering the derivatives with respect to $y_{f,t}$ the odd terms all vanish at the saddle point while the even terms are all equal to m/T. Fixing now y_f and φ_f to their saddle points, the following expansion holds

$$\frac{p^\mu u_\mu}{T} \sim \frac{m}{T} + \frac{m}{T}\frac{(y_{f,t} - y_t)^2}{2} + \frac{m}{T}\frac{(y_{f,t} - y_t)^4}{4!} + \mathcal{O}\left((y_{f,t} - y_t)^6\right). \tag{5.18}$$

[3] We call this coordinate system from now on the p_t-system.

For values of $y_{f,t} - y_t \lesssim \sqrt{T/m}$ the quadratic term is of order one. Therefore the quartic term is much smaller than the quadratic term, if one assumes $m \gg T$, which excludes pions and maybe even kaons.

If we insert (5.15) and (5.17) into the exponent of (5.2) via a Taylor expansion, we use the following formula to calculate the integral (5.1)

$$\lim_{T\to 0} \int_{-\infty}^{\infty} d^3x \exp\left(-\frac{p^\mu u_\mu(\mathsf{x})}{T}\right) = \exp\left(-\frac{p^\mu u_\mu(\mathsf{x}_{sp})}{T}\right) \sqrt{\frac{2\pi T^3}{(p^\mu u_\mu)''}}, \quad (5.19)$$

where $(p^\mu u_\mu)''$ is the product of the second derivatives from (5.17). The result is

$$E_{\vec{p}} \frac{d^3N}{d^3\vec{p}} = c(m) F\left(\frac{p_t}{m}, \varphi, y\right) \quad (5.20)$$

with $c(m) = \exp\left(-\frac{m}{T}\right) \sqrt{\frac{2\pi T^3}{m^3}}$ and $F\left(\frac{p_t}{m}, \varphi, y\right)$ a function which follows from changing the integration measure $d\sigma_\mu(\mathsf{x})\, p^\mu$ from space-time coordinates to four-velocity coordinates. The same result has already been shown in section 4.3. One should note that still no dissipative corrections have been considered.

5.1.3 Fast particles

Fast particles are defined as the particles whose transverse velocity is larger than the maximal transverse velocity $u_{max}(y_f, \varphi_f)$ reached by the fluid flowing in the same direction. For them $p^\mu u_\mu$ is minimal when the fluid transverse velocity takes its maximum value along that direction, namely $y_{f,t}^{max}(y_f, \varphi_f) = \ln\left[u_{max}(y_f, \varphi_f) + u^0_{max}(y_f, \varphi_f)\right]$, where we defined $u^0_{max}(y_f, \varphi_f) = \sqrt{1 + u_{max}(y_f, \varphi_f)^2}$. This yields the value of the product (5.7) at the corresponding point on the freeze-out hypersurface

$$p^\mu u_\mu(\mathsf{x}_{sp}) = m \cosh(y_t) u^0_{max}(y, \varphi) - m \sinh(y_t) u_{max}(y, \varphi). \quad (5.21)$$

Equivalently in the p_t-system with $u_\perp$ and $u_\parallel$ where the maximum is reached for $u_\parallel = u_{max}(y, \varphi)$, we deduce for (5.13)

$$p^\mu u_\mu(\mathsf{x}_{sp}) = m_t u^0_{max}(y, \varphi) - p_t u_{max}(y, \varphi). \quad (5.22)$$

At the saddle point, the first derivative in $y_{f,t}$ is

$$\left.\frac{\partial(p^\mu u_\mu)}{\partial y_{f,t}}\right|_{min} = m_t u_{max}(y, \varphi) - p_t u^0_{max}(y, \varphi), \quad (5.23)$$

respectively in the p_t-system the first derivative in $u_\parallel$ is

$$\left.\frac{\partial(p^\mu u_\mu)}{\partial u_\parallel}\right|_{min} = m_t v_{max}(y,\varphi) - p_t, \tag{5.24}$$

with $v_{max}(y,\varphi) \equiv u_{max}(y,\varphi)/u^0_{max}(y,\varphi)$. The latter expression shows clearly that the derivative is negative, since $p_t/m_t > v_{max}(y,\varphi)$. The other two first derivatives vanish as they did in the case of slow particles. In turn the non-vanishing second derivatives for fast particles are

$$\left.\frac{\partial^2(p^\mu u_\mu)}{\partial y_f^2}\right|_{min} = m_t u^0_{max}(y,\varphi) \tag{5.25a}$$

$$\left.\frac{\partial^2(p^\mu u_\mu)}{\partial \varphi_f^2}\right|_{min} = p_t u_{max}(y,\varphi) \tag{5.25b}$$

$$\left.\frac{\partial^2(p^\mu u_\mu)}{\partial y_{f,t}^2}\right|_{min} = m_t u^0_{max}(y,\varphi) - p_t u_{max}(y,\varphi), \tag{5.25c}$$

and in the corresponding p_t-system, the second derivatives are

$$\left.\frac{\partial^2(p^\mu u_\mu)}{\partial y_f^2}\right|_{min} = m_t u^0_{max}(y,\varphi) \tag{5.26a}$$

$$\left.\frac{\partial^2(p^\mu u_\mu)}{\partial u_\perp^2}\right|_{min} = m_t \frac{1}{u^0_{max}(y,\varphi)} \tag{5.26b}$$

$$\left.\frac{\partial^2(p^\mu u_\mu)}{\partial u_\parallel^2}\right|_{min} = m_t u^0_{max}(y,\varphi)^3. \tag{5.26c}$$

Both second derivatives with respect to $y_{f,t}$ and $u_\parallel$ are actually irrelevant for the saddle point approximation, since the corresponding first derivatives do not vanish. Therefore, the first derivatives are the leading terms in this approximation. However, they are important for the determination of the region of validity of the approximation. With y_f and φ_f fixed to their saddle point values we write

$$\begin{aligned}\frac{p^\mu u_\mu}{T} \sim \frac{m_t u^0_{max} - p_t u_{max}}{T} - \frac{p_t u^0_{max} - m_t u_{max}}{T}(y_{f,t} - y_f) \\ + \frac{m_t u^0_{max} - p_t u_{max}}{2T}(y_{f,t} - y_f)^2 + \mathcal{O}\left((y_{f,t} - y_t)^3\right).\end{aligned} \tag{5.27}$$

The quadratic term is negligible compared to the linear term, if

$$\frac{(m_t u_{max} - p_t u^0_{max})^2}{m_t u^0_{max} - p_t u_{max}} \gg T, \tag{5.28}$$

resulting in a validity region of the saddle point approximation. The condition (5.28) is more stringent than the trivial condition $p_t > m_t v_{max}$ and translates in a species-dependent lower bound of the particle transverse momentum. Also, like in the slow particle case, the smaller the freeze-out temperature, the better the saddle point approximation.

We write down the exponent $-p^\mu u_\mu/T$ in the Maxwell-Jüttner distribution (5.2) at the saddle point x_{sp} for fast particles

$$\begin{aligned} -\frac{p^\mu u_\mu(\mathsf{x})}{T} = &- \frac{m_t u_{max}(y,\varphi) - p_t u_{max}(y,\varphi)}{T} \\ &+ \frac{p_t u^0_{max}(y,\varphi) - m_t u_{max}(y,\varphi)}{T}(y_{f,t} - y^{max}_{f,t}(y,\varphi)) \\ &- \frac{m_t u^0_{max}(y,\varphi)}{T}\frac{(y_f - y)^2}{2} \\ &- \frac{p_t u_{max}(y,\varphi)}{T}\frac{(\varphi_f - \varphi)^2}{2}, \end{aligned} \tag{5.29}$$

or in case of the p_t-system

$$\begin{aligned} -\frac{p^\mu u_\mu(\mathsf{x})}{T} = &- \frac{m_t u_{max}(y,\varphi) - p_t u_{max}(y,\varphi)}{T} \\ &+ \frac{p_t u^0_{max}(y,\varphi) - m_t u_{max}(y,\varphi)}{T}(u_\parallel - u_{max}(y,\varphi)) \\ &- \frac{m_t u^0_{max}(y,\varphi)}{T}\frac{(y_f - y)^2}{2} \\ &- \frac{m_t}{T u^0_{max}(y,\varphi)}\frac{u^2_\perp}{2}, \end{aligned} \tag{5.30}$$

where every coefficient of each term is positive. Also, $(y_f - y)$, $(\varphi_f - \varphi)$, and $(y_{f,t} - y^{max}_{f,t}(y,\varphi))$, respectively $u_\perp$ and $(u_\parallel - u_{max}(y,\varphi))$ are functions of the space-time coordinate x, restricted to the freeze-out surface Σ. As in [6], depending on whether the maximum $y^{max}_{f,t}(y,\varphi)$, respectively $u_{max}(y,\varphi)$, is reached on the edge of Σ or at a point in its interior, it is possible for $y_{f,t} - y^{max}_{f,t}(y,\varphi)$ and $u_\parallel - u_{max}(y,\varphi)$ to be linear or quadratic

in their space-time coordinates. With (5.30) as the exponent of formula (5.2) we use equation (5.19) to calculate the particle momentum spectrum with the Cooper-Frye formula (5.1). For the $u_\parallel$-integral, which is simply a exponential function, the saddle point approximation is not needed. The results are

$$E_{\vec{p}}\frac{dN}{d^3\vec{p}} \propto \sqrt{\frac{2\pi T^3}{m_t^2}}\frac{1}{\sqrt{p_t - m_t v_{max}}}\exp\left(\frac{p_t u_{max} - m_t u^0_{max}}{T}\right), \tag{5.31}$$

if the maximum value u_{max} is reached at an inner point and

$$E_{\vec{p}}\frac{dN}{d^3\vec{p}} \propto \sqrt{\frac{2\pi T^3}{m_t^2}}\frac{1}{p_t - m_t v_{max}}\exp\left(\frac{p_t u_{max} - m_t u^0_{max}}{T}\right), \tag{5.32}$$

if the maximum value u_{max} is reached at the edge[4]. The first result coincides with the result in section 4.3. For practical purposes, we assume that the minimum is reached at an inner point and we neglect the prefactor $\sqrt{(2\pi T^3)/m_t^2}$, which is insignificant for the next calculations. The term which accounts for the change of the integration measure $d\sigma_\mu(\mathsf{x})\, p^\mu$ from space time to four-velocity coordinates is also neglected. Like in section 5.1.2, no dissipative corrections are included.

We conclude this section with a small remark: All calculations in section 5.1 hold for perfect and for dissipative fluids. However, the fluid velocity $\mathsf{u}(\mathsf{x})$ does change when switching from a perfect to a dissipative fluid, but these changes will not affect the following calculations.

5.2 Freeze-out of a dissipative fluid

This section introduces dissipative properties to the fluid. As in the previous section, we will divide the results into slow particles and fast particles. Since we only work with first order dissipative corrections, three possible dissipative transport phenomena may contribute: shear viscosity, bulk viscosity and heat conductivity. As seen in section 3.4.2, the Landau frame results in a vanishing heat current and the phenomenon of heat conductivity has not to be taken into account. Therefore, the following results have all been calculated within the Landau frame.

[4] In both formulas the (y, φ)-dependence of v_{max}, u_{max}, and u^0_{max} is implicit.

5.2.1 Slow particles revisited

First let us quickly review the results from section 5.1.2, respectively from section 4.3. If slow particles decouple from a perfect fluid, the Cooper-Frye prescription is simply a function of the mass m multiplied by a species-independent function

$$E_{\vec{p}}\frac{d^3N}{d^3\vec{p}} = c(m)F\left(\frac{p_t}{m}, \varphi, y\right). \tag{5.33}$$

The particle momentum spectrum for different particles should only differ by a normalization factor. The flow coefficients $v_n(p_t/m, y)$ should be identical for different species of slow particles. This leads to the so called "mass ordering", which means that the flow coefficients are smaller for heavier particles.

We show that these generic features persist for slow particles decoupling from a dissipative fluid. This holds at least as far as first order effects are concerned. One should note, that the factor c and the function F depend on the actual form of the dissipative corrections. These corrections are grouped into two kinds: shear viscosity δf_{shear} and bulk viscosity δf_{bulk}. We write δf from equation (5.3) as follows[5]

$$\delta f = \delta f_{shear} + \delta f_{bulk}. \tag{5.34}$$

First, consider the corrections δf_{shear} accounting for shear viscosity effects. Such a contribution should at least contain a term

$$\delta f_{shear}(\mathsf{x}, \mathsf{p}) \propto \pi^{\mu\nu}_{shear}(\mathsf{x}) p_\mu p_\nu, \tag{5.35}$$

with $\pi^{\mu\nu}_{shear}(\mathsf{x})$ the shear stress tensor, motivated by section 3.4.3. For our case, the important feature of the shear stress tensor is, that it is orthogonal to the fluid velocity, the so called *Landau matching condition*, which was already presented in equation (3.27)

$$\pi^{\mu\nu}_{shear}(\mathsf{x}) u_\mu(\mathsf{x}) = 0. \tag{5.36}$$

We have already shown in section 5.1.2 that the saddle point for slow particles is $u^\mu(\mathsf{x}) = p^\mu/m$ which yields at once

$$\pi^{\mu\nu}_{shear}(\mathsf{x}_{sp}) p_\mu p_\nu \propto \pi^{\mu\nu}_{shear}(\mathsf{x}_{sp}) u_\mu(\mathsf{x}) u_\nu(\mathsf{x}) = 0. \tag{5.37}$$

[5] The (x, p)-dependence is implicit.

Therefore, the additive correction for shear viscosity vanishes for slow particles at decoupling in the saddle point approximation.

Secondly, the bulk viscosity term δf_{bulk} is also motivated by section 3.4.3 and in general is written as

$$\delta f_{bulk}(\mathsf{x}, \mathsf{p}) = C_{bulk}(p^\mu u_\mu(\mathsf{x}), p^\mu p_\mu)\Pi(\mathsf{x}), \tag{5.38}$$

with $\Pi(\mathsf{x}) = \zeta \nabla_\mu(\mathsf{x}) u^\mu(\mathsf{x})$ the bulk pressure from equation (3.30) and C_{bulk} a certain function. For slow particles, it is easily shown that the arguments of C_{bulk} are simply m and m^2, which means the function is momentum independent. The bulk pressure at freeze-out only includes the expansion rate $\nabla_\mu(\mathsf{x}) u^\mu(\mathsf{x})$, which is taken at the saddle point for particles which have the same transverse velocity.

We find that the particle momentum distribution only depends on the momentum through the variables p_t/m, φ, and y, so that the conclusions for the decoupling from a perfect fluid remain valid for decoupling from a dissipative fluid. However, the factor c and the function F have to be modified.

5.2.2 Fast particles revisited

We review the dissipative corrections δf, which are again divided into shear viscosity δf_{shear} and bulk viscosity δf_{bulk}. We use the framework of Grad's prescription, in which the relative corrections to the phase-space distribution due to shear viscosity effects are written as

$$\begin{aligned} \delta f_{shear} &= \frac{1}{2\left[\epsilon(\mathsf{x}) + \mathcal{P}(\mathsf{x})\right] T(\mathsf{x})^2} \pi^{\mu\nu}_{shear}(\mathsf{x}) p_\mu p_\nu \\ &\equiv C_{shear}(\mathsf{x}) \pi^{\mu\nu}_{shear}(\mathsf{x}) p_\mu p_\nu \end{aligned} \tag{5.39}$$

with $\epsilon(\mathsf{x})$ and $\mathcal{P}(\mathsf{x})$ the already known energy density and pressure from chapter 3. The shear stress tensor $\pi^{\mu\nu}_{shear}(\mathsf{x})$ is recast as $\pi^{\mu\nu}_{shear}(\mathsf{x}) = \eta \nabla^{\langle\mu} u^{\nu\rangle}$ from equation (3.31), with η the shear viscosity and $\nabla^{\langle\mu} u^{\nu\rangle} = \nabla^\mu u^\nu + \nabla^\nu u^\mu - \frac{2}{3}\left[\nabla^\nu u_\nu\right]$, where we have neglected the x-dependency of ∇^μ and u^μ. To handle the product $\pi^{\mu\nu}_{shear}(\mathsf{x}) p_\mu p_\nu$, we use the Landau condition to cancel out the component of the the particle four-momentum p along the flow velocity u, by introducing[6] $q^\mu \equiv p^\mu - (p^0/u^0)u^\mu$. We obtain $\pi^{\mu\nu}_{shear}(\mathsf{x}) p_\mu p_\nu = \pi^{\mu\nu}_{shear}(\mathsf{x}) q_\mu q_\nu$.

[6] Note that q^μ is not the heat current, introduced in equation (3.25).

We make the assumption that our velocity profile should only have a radial component u^r and an azimuthal component u^φ. Therefore, the only non-vanishing components of $\pi^{\mu\nu}_{shear}(\mathsf{x})$ are $\pi^{rr}_{shear}(\mathsf{x})$, $\pi^{\varphi\varphi}_{shear}(\mathsf{x})$, and the symmetric component $\pi^{r\varphi}_{shear}(\mathsf{x})$. Computations yield

$$\pi^{rr}_{shear} = -2\eta \left[\partial_r u^r + u^r D u^r - \frac{1 + (u^r)^2}{3} \nabla \cdot \mathsf{u} \right] \tag{5.40a}$$

$$\pi^{\varphi\varphi}_{shear} = -2\eta \left[\frac{1}{r^2} \partial_\varphi u^\varphi + \frac{1}{r^3} u^r + u^\varphi D u^\varphi - \frac{1 + (r u^\varphi)^2}{3r^2} \nabla \cdot \mathsf{u} \right] \tag{5.40b}$$

$$\pi^{r\varphi}_{shear} = -\eta \left[\partial_r u^\varphi + \frac{1}{r^2} \partial_\varphi u^r + u^r D u^\varphi + u^\varphi D u^r - \frac{2 u^r u^\varphi}{3} \nabla \cdot \mathsf{u} \right], \tag{5.40c}$$

where D is given by $Du^\mu = u^\nu d_\nu u^\mu$. D is the time derivative in the local rest frame (Landau frame) and $\nabla \cdot \mathsf{u}$ is the four-divergence of the velocity field

$$\nabla \cdot \mathsf{u} = \partial_r u^r + \partial_\varphi u^\varphi + \partial_\tau u^\tau + \frac{u^r}{r} + \frac{u^\tau}{\tau}. \tag{5.41}$$

We assume that the velocity profile is approximately radial at freeze-out and that u^φ and its derivatives vanish. Under this hypothesis, only the radial components of q^μ and $\pi^{\mu\nu}_{shear}(\mathsf{x})$ contribute, with

$$q^r = p_t - m_t v_{max}(y, \varphi) \tag{5.42}$$

and $\pi^{rr}_{shear}(\mathsf{x})$ as in equation (5.40a). At the saddle point, corresponding to a given four-momentum, we find

$$\delta f_{shear} = C_{shear}(\mathsf{x}_{sp}) \pi^{rr}_{shear}(\mathsf{x}_{sp}) \left[p_t - m_t v_{max}(y, \varphi) \right]^2. \tag{5.43}$$

The bulk viscosity term δf_{bulk} is neglected because it is of higher order in φ in the Cooper-Frye formula (5.1). If we look at (5.3), the equilibrium distribution f_0 should be of order one in φ at the saddle point, which means that the computed correction (5.43) is already of second order in φ and therefore it is the leading term in δf. This indicates that δf_{bulk} has to be of higher order than δf_{shear} and therefore can be neglected. Furthermore, the bulk viscosity ζ in the bulk pressure $\Pi(\mathsf{x})$ is proportional to $c_s^2 - 1/3$, where c_s is the speed of sound. In the case of relativistic heavy-ion collisions, calculations revealed that the speed of sound is about $1/\sqrt{3}$, which leads to $\zeta \approx 0$.

Inserting equation (5.43) into formula (5.3) and combining it with the result from equation (5.31), we achieve the following result for the particle momentum spectrum[7]

$$E_{\vec{p}}\frac{d^3N}{d^3\vec{p}} \propto \frac{1}{\sqrt{p_t - m_t v_{max}}}(1 + C_{shear}(\mathsf{x}_{sp})\pi^{rr}_{shear}(\mathsf{x}_{sp})\left[p_t - m_t v_{max}(y,\varphi)\right]^2) \times \exp\left[\frac{p_t u_{max}(y,\varphi) - m_t u^0_{max}(y,\varphi)}{T}\right], \quad (5.44)$$

or, if the prefactor is neglected,

$$E_{\vec{p}}\frac{d^3N}{d^3\vec{p}} \propto (1 + C_{shear}(\mathsf{x}_{sp})\pi^{rr}_{shear}(\mathsf{x}_{sp})\left[p_t - m_t v_{max}(y,\varphi)\right]^2) \times \exp\left[\frac{p_t u_{max}(y,\varphi) - m_t u^0_{max}(y,\varphi)}{T}\right]. \quad (5.45)$$

Neglecting the y- and φ-dependence in (5.44), respectively (5.45), results in the transverse momentum spectrum dN/dp_t. The transverse momentum spectra are shown in figure 5.1.

It is shown that the approximated dissipative momentum spectrum coincides for large p_t with the complete dissipative spectrum, but departs from it for low p_t, obviously due to the neglected square root prefactor. Furthermore, the "exact" dissipative spectrum coincides with the perfect spectrum for low p_t, but for high p_t it grows larger, indicating a "harder" spectrum for the decoupled particles. This behavior is in good agreement with our results for slow particles from the previous section 5.2.1. The prefactor in (5.44) should depend on the dissipative corrections, which are estimated at the saddle point, as well as the behavior of the velocity in the neighborhood of the saddle point, which necessitates a more detailed knowledge on the flow profile at the freeze-out. Here, we chose a constant value for u_{max}, which allows us to show the differences between the three possible momentum spectra.

To bypass the need for a more detailed knowledge about the prefactor, we will focus on the azimuthal anisotropies of the particle distribution, the flow coefficients v_n. The flow coefficients should not depend on the normalization factor of the spectrum in (5.44). We also assume that the

[7] Again, the (y,φ)-dependence of v_{max} under the square root is implicit.

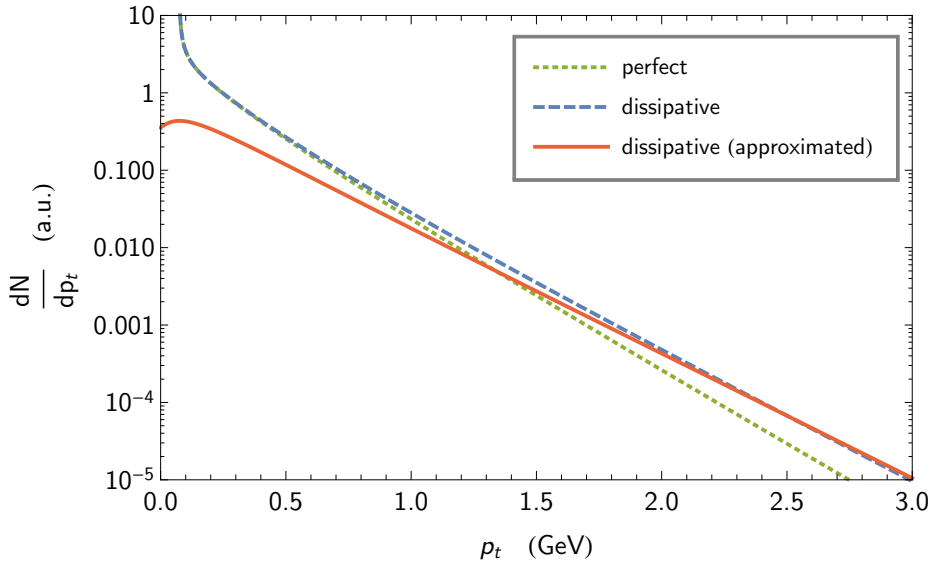

Figure 5.1: Comparison between the transverse momentum spectrum for a perfect and a dissipative fluid for fixed values of u_{max}, T, m, and η.

rapidity y does not play a role for our calculations and therefore remove it from our expressions.

The expansion of the maximum transverse flow velocity has already been introduced in section 4.4. Again, we perform an expansion of $u_{max}(\varphi)$ at the freeze-out as a Fourier series

$$u_{max}(\varphi) = \overline{u}_{max}\left[1 + 2\sum_{n\geq 1} V_n \cos\left[n(\varphi - \Psi_n)\right]\right], \tag{5.46}$$

with Ψ_n the n-th harmonic symmetry-plane angle. Given any realistic velocity profile, $\overline{u}_{max}$ and the anisotropies V_n should easily be reconstructed. The three-velocity value corresponding to the average maximum transverse flow velocity $\overline{v}_{max}$ will be denoted as

$$\overline{v}_{max} = \frac{\overline{u}_{max}}{\sqrt{1 + \overline{u}^2_{max}}}. \tag{5.47}$$

A typical value for $\overline{u}_{max}$ is roughly 1, which amounts to $\overline{v}_{max} \approx 0.7$. In turn the Fourier coefficients V_n are assumed to be small, roughly of order 0.05 or smaller. We assume the following hierarchy: $V_2 \gtrsim V_3 \gg V_1, V_4, V_5$, and the higher coefficients all vanish. Our calculations can easily be repeated with any other hierarchy of the anisotropies of the maximum transverse flow velocity at the freeze-out.

The expansion from equation (5.46) is inserted in equation (5.44), in the exponent and in the prefactor. In the latter, one should keep in mind the Fourier expansions of various combinations of the derivatives of the flow velocity u around the saddle point. We are for instance interested in the azimuthal dependence of the shear stress tensor, but for simplicity we neglect this dependence, considering that it only represents a small modulation of a small quantity itself. There is however no difficulty in including the refinement at the cost of introducing new Fourier coefficients for each azimuthally dependent quantity.

We start with the exponent of (5.44) and expand it with the help of (5.46). We use $\sqrt{1+(a+x)^2} \approx \sqrt{1+a^2} + ax/\sqrt{1+a^2}$ to rewrite the exponent

$$\begin{aligned} & p_t u_{max}(\varphi) - m_t u^0_{max}(\varphi) \\ & = p_t \overline{u}_{max} - m_t \sqrt{1+\overline{u}^2_{max}} + 2\left(p_t - m_t \overline{v}_{max}\right) \overline{u}_{max} \\ & \quad \times \sum_{n\geq 1} 2V_n \cos\left[n(\varphi - \Psi_n)\right]. \end{aligned} \tag{5.48}$$

Expanding only the exponential function in (5.44) with the help of (5.48) up to quadratic order results in

$$\begin{aligned} E_{\vec{p}} \frac{d^3N}{d^3\vec{p}} \propto & \exp\left[\frac{p_t \overline{u}_{max} - m_t\sqrt{1+\overline{u}^2_{max}}}{T}\right] \\ & \times \Big[1 + \mathcal{I}(p_t) \sum_{n\geq 1} 2V_n \cos\left[n(\varphi - \Psi_n)\right] \\ & \quad + \mathcal{I}(p_t)^2 \sum_{n\geq 1} 2V_n^2 \cos^2\left[n(\varphi - \Psi_n)\right] \\ & \quad + \mathcal{I}(p_t)^2 \sum_{n>m} 4V_n V_m \cos\left[n(\varphi - \Psi_n)\right] \cos\left[m(\varphi - \Psi_m)\right] \Big], \end{aligned} \tag{5.49}$$

where the function $\mathcal{I}(p_t)$ is introduced as

$$\mathcal{I}(p_t) = \overline{u}_{max} \frac{p_t - m_t \overline{v}_{max}}{T}. \tag{5.50}$$

Since $p_t/m_t > \overline{v}_{max}$ it is assured that $\mathcal{I}(p_t)$ is always positive for fast particles. Trigonometric relations are used for the term between the squared brackets to write

$$\begin{aligned} &1 + \mathcal{I}(p_t)^2 \sum_{n\geq 1} V_n^2 \\ &\quad + \mathcal{I}(p_t) \sum_{n\geq 1} 2V_n \cos\left[n(\varphi - \Psi_n)\right] \\ &\quad + \frac{1}{2}\mathcal{I}(p_t)^2 \sum_{n\geq 1} 2V_n^2 \cos\left[2n(\varphi - \Psi_n)\right] \\ &\quad + \mathcal{I}(p_t)^2 \sum_{n>m} 2V_n V_m (\cos[(n+m)\varphi - n\Psi_n - m\Psi_m] \\ &\qquad\qquad + \cos[(n-m)\varphi - n\Psi_n + m\Psi_m]). \end{aligned} \tag{5.51}$$

The second term, which is φ-independent is dropped because the V_n themselves are very small. As a consequence the flow coefficients v_n are read off the expansion (5.51) itself by selecting the corresponding $2\cos[n(\varphi - \Psi_n)]$ terms. The results for the first five coefficients are

$$v_1(p_t) = \mathcal{I}(p_t) V_1 + \mathcal{I}(p_t)^2 V_2 V_3, \tag{5.52a}$$
$$v_2(p_t) = \mathcal{I}(p_t) V_2, \tag{5.52b}$$
$$v_3(p_t) = \mathcal{I}(p_t) V_3 + \mathcal{I}(p_t)^2 V_1 V_2, \tag{5.52c}$$
$$v_4(p_t) = \mathcal{I}(p_t) V_4 + \frac{\mathcal{I}(p_t)^2}{2} V_2^2, \tag{5.52d}$$
$$v_5(p_t) = \mathcal{I}(p_t) V_5 + \mathcal{I}(p_t)^2 V_2 V_3. \tag{5.52e}$$

If p_t is high enough, V_1, V_4, and V_5 can be neglected and one finds the following two relations

$$v_4(p_t) \simeq \frac{v_2(p_t)^2}{2}, \tag{5.53a}$$
$$v_5(p_t) \simeq v_2(p_t) v_3(p_t). \tag{5.53b}$$

The first relation is the same as in equation (4.9) and the second relation is found in [31].

The final step in this section is to extend the previous steps to a dissipative fluid. Fortunately, we can use all aspects of the solution for the exponential function and simply have to "expand" them to the dissipative prefactor. We go back to equation (5.43) and rewrite it to

$$\delta f_{shear} = C'_{shear} \left[p_t - m_t v_{max}(y,\varphi)\right]^2 \tag{5.54}$$

with the new function C'_{shear}

$$C'_{shear} \equiv C_{shear}(\mathsf{x}_{sp})\pi^{rr}_{shear}(\mathsf{x}_{sp}). \tag{5.55}$$

The expansion of $u_{max}(\varphi)$ in (5.46) is applied to the dissipative correction (5.54), which results in

$$\begin{aligned} p_t - m_t v_{max}(\varphi) &\approx p_t - m_t \overline{v}_{max} - \frac{m_t \overline{v}_{max}}{1+\overline{u}^2_{max}} \sum_{n\geq 1} 2V_n \cos\left[n(\varphi - \Psi_n)\right] \\ \Rightarrow \left[p_t - m_t v_{max}(\varphi)\right]^2 &\approx \left(p_t - m_t \overline{v}_{max}\right)^2 - 2\left(p_t - m_t \overline{v}_{max}\right) \frac{m_t \overline{v}_{max}}{1+\overline{u}^2_{max}} \\ &\quad \times \sum_{n\geq 1} 2V_n \cos[n(\varphi - \Psi_n)], \end{aligned} \tag{5.56}$$

where quadratic terms in φ have been neglected. The φ-dependence of $\pi^{rr}_{shear}(\mathsf{x}_{sp})$ is also neglected and we insert (5.56) into the correction (5.54) so that we can rewrite $1 + \delta f_{shear}$ to

$$\begin{aligned} 1 + \delta f_{shear} &= 1 + C'_{shear}\left[p_t - m_t v_{max}(y,\varphi)\right]^2 \\ &\approx 1 + C'_{shear}\left(p_t - m_t \overline{v}_{max}\right)^2 \\ &\quad \times \left[1 - \frac{2}{p_t - m_t \overline{v}_{max}} \frac{m_t \overline{v}_{max}}{1+\overline{u}^2_{max}} \sum_{n\geq 1} 2V_n \cos n(\varphi - \Psi_n)\right] \\ &= \left[1 + C'_{shear}\left(p_t - m_t \overline{v}_{max}\right)^2\right] \\ &\quad \times \left[1 - \mathcal{D}(p_t) \sum_{n\geq 1} 2V_n \cos[n(\varphi - \Psi_n)]\right]. \end{aligned} \tag{5.57}$$

The first factor in (5.57) is independent of the azimuth angle φ and does not contribute to the flow coefficients v_n. The second factor yields the dissipative term $\mathcal{D}(p_t)$

$$\mathcal{D}(p_t) = \frac{2C'_{shear}\left(p_t - m_t\overline{v}_{max}\right)}{1 + C'_{shear}\left(p_t - m_t\overline{v}_{max}\right)^2}\frac{m_t\overline{v}_{max}}{1+\overline{u}^2_{max}}, \tag{5.58}$$

which adds dissipative properties to the flow coefficients v_n. The term $C'_{shear}\left(p_t - m_t\overline{v}_{max}\right)^2$ should be significantly smaller than one to assure that dissipative corrections remain small. The dependence of $\mathcal{D}(p_t)$ on the transverse momentum p_t is thus actually given by the numerator and is approximately quadratic. We combine the expansions (5.51) and (5.57) and recalculate the first five flow coefficients

$$v_1(p_t) = \left[\mathcal{I}(p_t) - \mathcal{D}(p_t)\right]V_1 + \left[\mathcal{I}(p_t)^2 - \mathcal{I}(p_t)\mathcal{D}(p_t)\right]V_2V_3, \tag{5.59a}$$

$$v_2(p_t) = \left[\mathcal{I}(p_t) - \mathcal{D}(p_t)\right]V_2, \tag{5.59b}$$

$$v_3(p_t) = \left[\mathcal{I}(p_t) - \mathcal{D}(p_t)\right]V_3 + \left[\mathcal{I}(p_t)^2 - \mathcal{I}(p_t)\mathcal{D}(p_t)\right]V_1V_2, \tag{5.59c}$$

$$v_4(p_t) = \left[\mathcal{I}(p_t) - \mathcal{D}(p_t)\right]V_4 + \left[\frac{\mathcal{I}(p_t)^2}{2} - \mathcal{I}(p_t)\mathcal{D}(p_t)\right]V_2^2, \tag{5.59d}$$

$$v_5(p_t) = \left[\mathcal{I}(p_t) - \mathcal{D}(p_t)\right]V_5 + \left[\mathcal{I}(p_t)^2 - \mathcal{I}(p_t)\mathcal{D}(p_t)\right]V_2V_3. \tag{5.59e}$$

The dissipative contribution vanishes if dissipative corrections are absent, leaving only the solutions for a perfect fluid. It is possible to compute $\mathcal{D}(p_t)$ starting from any ansatz for δf. The result can then be compared to the shape constrained from experimental results. Furthermore, there is another change which is not reflected in our notations, affecting the average $\overline{u}_{max}$ and the Fourier coefficients V_n of the maximum flow velocity at freeze-out, depending on the amount of dissipation along the evolution of the system. In the following, we assume that these values are fixed and only consider the effects of $\mathcal{D}(p_t)$.

In figure 5.2 on page 68 the flow coefficients $v_2(p_t)$, $v_3(p_t)$, and $v_4(p_t)$ for a perfect fluid taken from the equations (5.52) and for a dissipative fluid from the equations (5.59) are shown.

We perceive that $\mathcal{D}(p_t)$ is positive and its inclusion leads to a decrease of every flow coefficient (see also [32]). The graphical presentation in figure 5.2 shows clearly this property of $\mathcal{D}(p_t)$. The actual sign of $\mathcal{D}(p_t)$ depends

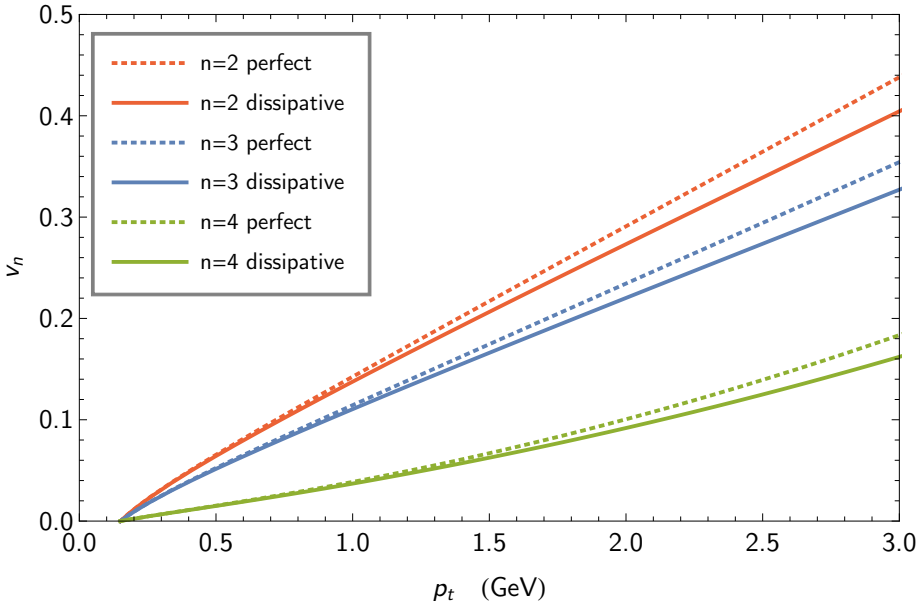

Figure 5.2: Comparison between the flow coefficients $v_2(p_t)$, $v_3(p_t)$, and $v_4(p_t)$ for a perfect fluid (dotted lines) and for a dissipative fluid (full lines). We set C'_{shear} to 0.2 and fixed $\overline{u}_{max}$, T, and m. Not shown are $v_1(p_t)$ and $v_5(p_t)$ because they mostly overlap with $v_4(p_t)$.

on the flow profile at freeze-out. It turned out to be positive in existing hydrodynamical simulations. In particular, the decrease of $v_2(p_t)$ at large transverse momentum and mid-rapidity explains a posteriori our choice of signs in the equations (5.59). However, there are theoretical reasons to expect that the bulk viscosity contribution to $\mathcal{D}(p_t)$ could change the sign [29]. It is not clear if this behavior should happen in the fast particle region and therefore no definite statement can be made.

Similar to the perfect fluid case, some equations in (5.59) show obvious similarities. For vanishing V_1, V_4, and V_5, equation (5.59b) and equation (5.59c) predict a constant ratio

$$\frac{v_3(p_t)}{v_2(p_t)} \simeq \frac{V_3}{V_2}, \tag{5.60}$$

in case the hierarchy $V_3 \sim V_2$ holds. Likewise, equations (5.59a) and (5.59e) are very similar and predict similar behavior for $v_1(p_t)$ and $v_5(p_t)$ in the regime where the linear contributions to these harmonics become negligible with respect to the V_2V_3 term. We emphasize that the similarities between different flow harmonics hold in the regime of fast particles, far from low p_t, where the analyticity of the momentum distribution induces different scaling behaviors for each flow harmonic [33].

From the equations in (5.59) it is deduced that the nonlinear relations from (5.53), which were valid in the perfect case, no longer hold. Thus the first relation (5.53a) is changed to

$$\frac{v_4(p_t)}{v_2(p_t)^2} < \frac{1}{2}, \tag{5.61}$$

if V_4 is neglected. The ratio is decreased by the inclusion of the dissipative correction $\mathcal{D}(p_t)$, with or without V_4. In contrast, when we neglect V_5 the second relation (5.53b) changes to

$$\frac{v_5(p_t)}{v_2(p_t)v_3(p_t)} > 1. \tag{5.62}$$

It shows a larger value than in the case of a perfect fluid. These qualitative results originates from either a Boltzmann transport model [34] or hydrodynamical simulations [31,35]. We exploited the nonlinear relations for more quantitative results, still in negligible linear contributions. We extract from (5.59b), (5.59c), and (5.59e) the relation

$$\frac{v_5(p_t) - v_2(p_t)v_3(p_t)}{v_3(p_t)} \simeq V_2\mathcal{D}(p_t) \tag{5.63}$$

or similar from equation (5.59b) and (5.59d) the relation

$$v_2(p_t)^2 - 2v_4(p_t) \simeq [V_2\mathcal{D}(p_t)]^2. \tag{5.64}$$

It is possible to isolate the dissipative contributions from decoupling to $v_2(p_t)$ or more generally $\mathcal{D}(p_t)$. We find two independent relations from which the dissipative term can be constrained experimentally and then may be compared with the functional form derived from an ansatz for δf.

5.3 Discussion

In the previous section 5.2, we investigated the dissipative effects of dissipative corrections δf to the phase-space distribution f_0 of particles at freeze-out. In this section, we want to test the found results, especially those for fast particles. Therefore, we compare them to the flow coefficients calculated from the numerical integration over a three dimensional freeze-out hypersurface Σ of a flow profile u. For Σ we choose an infinite azimuthally symmetric cylinder of radius R at a constant proper time τ_{fo} and cylindrical coordinates r, ϕ and space-time rapidity η_s. Furthermore, we assume that for the fluid velocity on Σ a generalized blast-wave profile for the radial component is applicable [36, 37]

$$u^r(r,\phi) = \overline{u}_{max}\frac{r}{R}\left(1 + 2\sum_{n=1}^{5} V_n \cos(n\phi)\right). \tag{5.65}$$

For the other velocity coordinates we simply assume

$$u^\phi = u^{\eta_s} = 0, \tag{5.66}$$

in the ϕ- and η_s-direction, as well as the natural component

$$u^\tau(r,\phi) = \sqrt{1 + u^r(r,\phi)^2} \tag{5.67}$$

in the time-like direction. From these expressions the maximal transverse velocity in equation (5.46) is directly extracted. The graphical presentations were generated with the following values: $R = 7.5\,\mathrm{fm}$, $\tau_{fo} = 5.25\,\mathrm{fm}$, $T = 160\,\mathrm{MeV}$, $\overline{u}_{max} = 0.55$, $V_2 = 0.05$ (corresponding to [20]), $V_3 = 0.05$, and all other $V_n = 0$. Other values did not change the general behavior of the following results.

With such a choice of values for the flow profile, 7 out of 10 components of $\pi^{\mu\nu}_{shear}(\mathsf{x})$ are non-zero. Nevertheless, in our saddle point approximation only the $\pi^{rr}_{shear}(\mathsf{x})$ term was kept, as explained in section 5.2.2. The relatively small $\overline{u}_{max}$ along with a small value for

$$\frac{\eta}{s} = \frac{\eta}{(e+\mathcal{P})T} = 0.16 \tag{5.68}$$

lead to a value of about 0.6 for the coefficient C'_{shear}. This ensures that some of the terms we have neglected when deriving the correction term

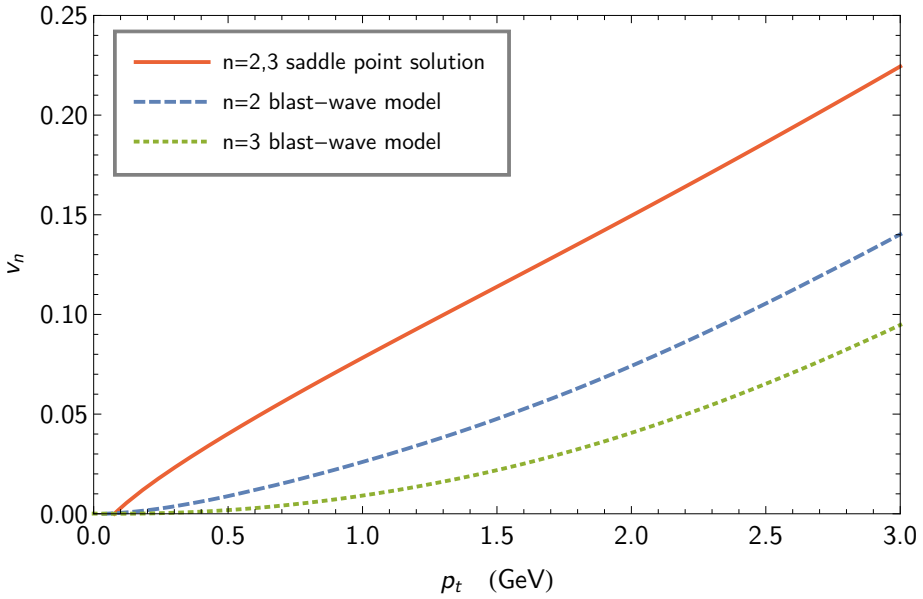

Figure 5.3: Comparison between the saddle point solutions and the numerical blast-wave model results for $v_2(p_t)$ and $v_3(p_t)$ for a dissipative fluid.

(5.58) remain small as long as p_t is not too large, respectively $p_t - m_t\overline{v}_{max}$. With this setup for our blast-wave model of the Cooper-Frye formula, we compare its results to our findings within the saddle point approximation. We focus on pions and choose $p_t \geq 0.6\,\text{GeV}$.

Let us start with the unsatisfying aspects of our approximation of the v_n in (5.59). The approximation itself is a poor representation compared to those of the numerical blast-wave simulation in a reasonable p_t-region (see figure 5.3). We list a few discrepancies for the v_n from (5.59), which already appear for the results of a perfect fluid. $v_2(p_t)$ in the exact blast-wave model grows quadratically at low p_t for pions, this should be between 1 GeV to 1.5 GeV, while the equation (5.59b) is almost linear (see figure 5.3). Furthermore, (5.59b) and (5.59c) predict a parallel behavior for $v_2(p_t)$ and $v_3(p_t)$. Actually, with our choice of V_n, they are identical. The full computation of $v_2(p_t)$ and $v_3(p_t)$ shows that they are significantly

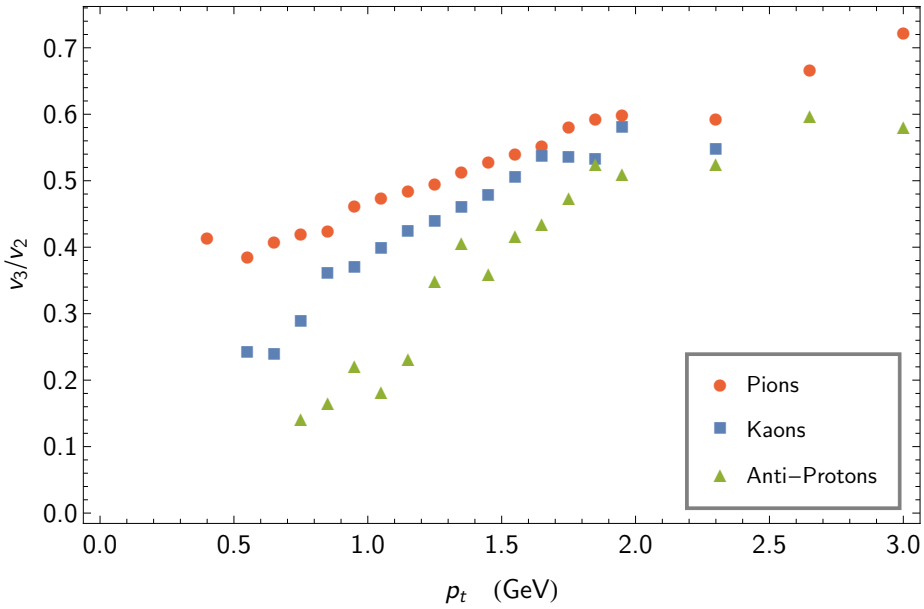

Figure 5.4: Experimental data from the ALICE collaboration. [38]

smaller and differ from each other, also seen in figure 5.3. The ratio $v_3(p_t)/v_2(p_t)$ for pions grows from 0.5 at 1 GeV to 0.8 at 3 GeV. Comparisons between the other v_n reveal further discrepancies. Below 3 GeV the blast-wave $v_1(p_t)$ and $v_5(p_t)$ differ by more than a factor 2, while in our equations (5.59a) and (5.59e) they are equal. $v_4(p_t)$ and $v_5(p_t)$ are almost equal, while (5.59d) and (5.59e) predict a factor of 2. All in all, below 3 GeV our approximations in (5.59) are quite unsatisfactory. However, they become much better above 5 GeV, as it was already observed for the nonlinear relations between higher and lower flow coefficients in realistic hydrodynamical computations [31]. Unfortunately, this region is not relevant to experimental data, but might help with the understanding of numerical fluid dynamics simulations.

On the other hand, experimental data shows the estimated behavior for $v_2(p_t)$ and $v_3(p_t)$ above a certain p_t value, as seen in the experimental data

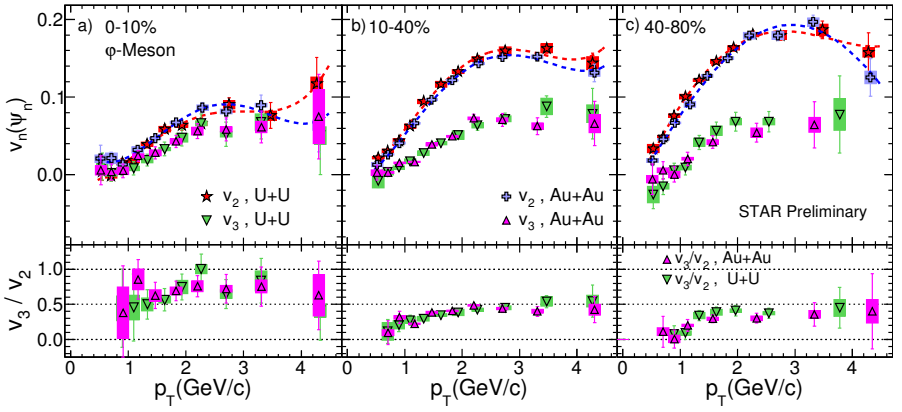

Figure 5.5: Experimental data from the STAR collaboration. [39]

from ALICE [38] and STAR [39]. Data[8] from the ALICE collaboration almost shows the desired behavior, seen in figure 5.4. While pions and kaons have only a small deviation from our predicted constant behavior between 1.5 GeV and 2.5 GeV for p_t, anti-protons deviate clearly from it. Data from the STAR collaboration shows in the p_t range from 2 GeV to 4 GeV for 10% to 40% centrality that the ratio remains at a constant value of about 0.5 (figure 5.5, middle). For 40% to 80% centrality the behavior is still visible between 1.5 GeV and 4 GeV with a value of 0.5, however the error bars slightly increase (figure 5.5, right). And finally for 0% to 10% centrality (figure 5.5, left) the ratio between $v_2(p_t)$ and $v_3(p_t)$ is still found, but the value changes to 0.75 and the error bars are significantly larger.

Despite having just criticized our predictions in (5.59), we argue now that the saddle point approximation captures the nature of dissipative effects at freeze-out in a very good manner. To illustrate this point, we display in figure 5.6 on page 74 the difference between the perfect and dissipative $v_2(p_t)$, computed with the same parameters as above, given by the exact numerical integration of the Cooper-Frye formula. This difference should only reflect the dissipative correction δf, which within our

[8] Note that the error bars for the data points in figure 5.4 are too small to be visible.

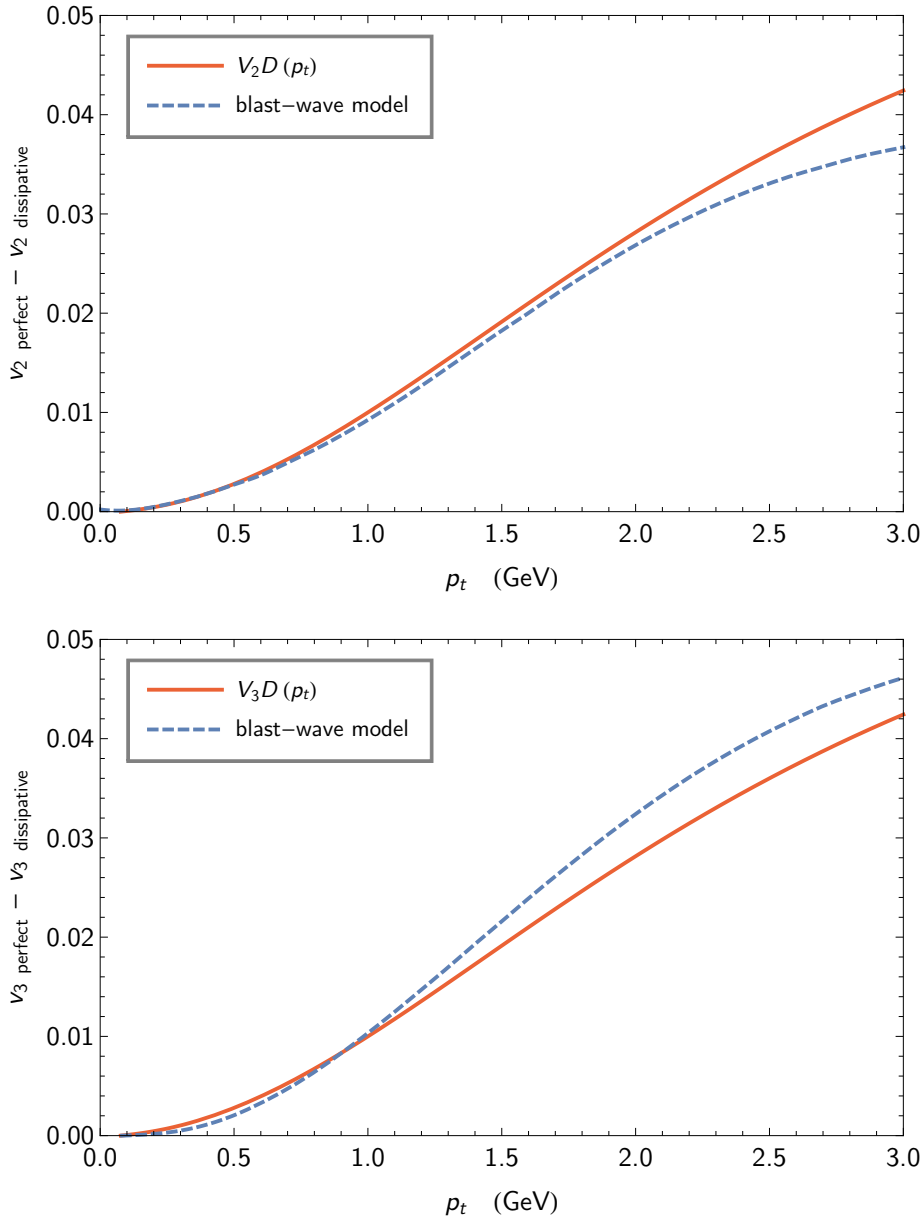

Figure 5.6: The difference between the perfect and dissipative solution of $v_2(p_t)$ (top) and $v_3(p_t)$ (bottom) for a blast-wave model computation (dashed line) or within the saddle point approximation (full line).

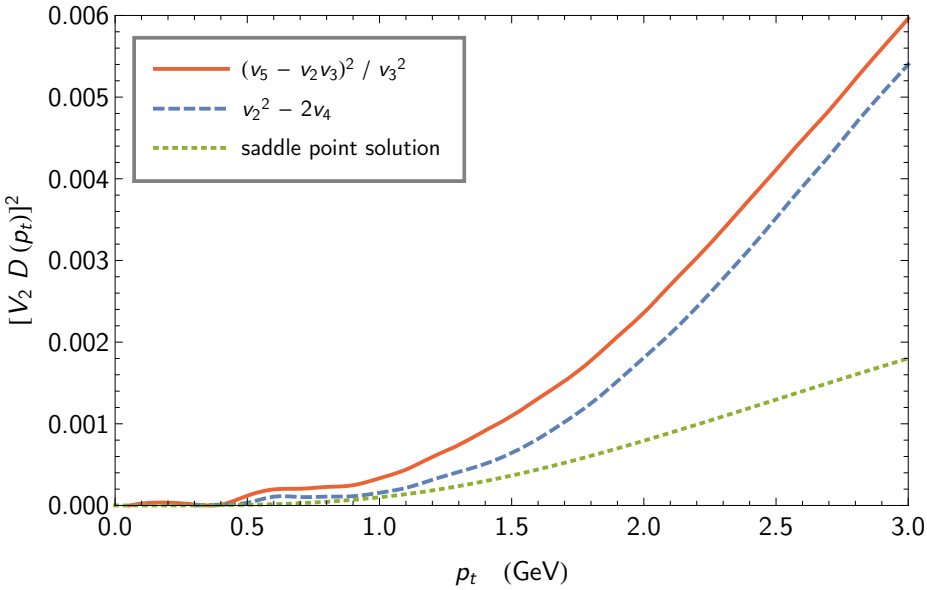

Figure 5.7: Results from (5.63) and (5.64) in a blast-wave model computation of the Cooper-Frye integral with dissipative corrections (full and dashed lines). Also shown is the squared dissipative part of $v_2(p_t)$ within the saddle point approximation (dotted line).

saddle point approximation is simply $V_2\mathcal{D}(p_t)$, with $\mathcal{D}(p_t)$ given by equation (5.58). The agreement between the analytical and numerical result is very good, especially when one keeps in mind that the $v_2(p_t)$ value itself is quite poorly approximated by the saddle point approximation in both cases. One should note that the two curves depart above 2 GeV. This behavior arises from discarding terms in the derivation of the simple formula (5.58) and could be handled by including more terms. However, we have no explanation for the good agreement for low p_t outside the regime of fast particles.

As mentioned above, the blast-wave results for $v_2(p_t)$ and $v_3(p_t)$ are quite different from each other, in contrast to the saddle point approximation. In figure 5.6 we also show the difference of the perfect and dissipative $v_3(p_t)$. The saddle point approximation $V_3\mathcal{D}(p_t)$ is again a good approx-

imation to the full computation within the blast-wave model. Especially given by the fact, that the saddle point calculation for $v_3(p_t)$ is too large by a factor of about 2 across the whole p_t range.

Both figures in 5.6 reveal that the saddle-point approximation correctly approximates the dissipative corrections arising from additive terms at freeze-out. However, the displayed quantities are no experimental observables and thus this particular result can only be used for numerical simulations where corrections are turned on and off at will. In contrast, the combinations on the left-hand sides of equations (5.63) and (5.64) only involve measurable quantities. In figure 5.7 on page 75, we show the squared left-hand side of (5.63) and the left-hand side of (5.64), computed within the blast-wave model at freeze-out with dissipative corrections. From the equations they should be equal to the squared dissipative contribution of $v_2(p_t)$, which is $[V_2\mathcal{D}(p_t)]^2$. However, they are about a factor of 2-3 times larger than $[V_2\mathcal{D}(p_t)]^2$, which is calculated within the saddle point approximation (also seen in figure 5.7). Furthermore, these combinations of flow coefficients do not vanish when they are computed with flow coefficients obtained in the blast-wave model without dissipative corrections unlike the saddle point results. This is disappointing, yet we view the good agreement between the full line and the dashed line in figure 5.7 as a hint that the displayed quantities open the possibility to pin down the effects of dissipation at decoupling, although we could not come up with a good mathematical argument to substantiate this statement.

6 Anisotropic hydrodynamics

In chapter 5 the fundamental theory was dissipative hydrodynamics. The results we achieved in the dissipative framework were sometimes remarkably good and may allow some insight in the form of the dissipative corrections in the process of the freeze-out. Unfortunately, other results were not accurate and need either a more complex modeling for the (one-particle) distribution function corrections δf or a complete new ansatz for the whole distribution function f. But even before our model was applied, the whole concept of the sudden freeze-out approximation has some discrepancies. For example, the approximation needs a certain proper time τ_{fo}, when the freeze-out should begin, and a certain freeze-out temperature T at which the transition from a fluid to particles takes place.

We do not want to abandon the whole idea of the Cooper-Frye formula, but instead want to find a new ansatz which might help with the conceptual problems of the sudden freeze-out approximation. Since a few years, such an ansatz is present in form of *anisotropic hydrodynamics*. The general idea is that the distribution function itself should be anisotropic, generated by an *anisotropic tensor* of rank two. The origin of this idea stems from the fact that the initial condition in a relativistic heavy-ion collision itself is highly anisotropic. It should be easier to account for this anisotropy by making the whole dynamic process anisotropic, instead of just adding anisotropic terms to parameters and observables.

In this chapter the motivation and basic formulas for anisotropic hydrodynamics are presented. We also present calculations for the hydrodynamic fields in case of an anisotropic distribution function.

6.1 Motivation

Despite the success of perfect and dissipative hydrodynamic descriptions in the process of relativistic heavy-ion collisions, there are still some issues which need to be addressed. One issue is, that the traditional derivation

of dissipative hydrodynamics and its dynamical equations (see chapter 3), relies on a linearization around an isotropic (local) equilibrium distribution. In recent years we have come to understand that the matter created in relativistic heavy-ion collisions is not momentum-space isotropic. For example, shortly after the collision of two nuclei one finds very large pressure anisotropies. This signifies that the pressure along the beam axis, the *longitudinal pressure* $\mathcal{P}_L$ is smaller than the pressure perpendicular to the beam axis, the *transverse pressure* $\mathcal{P}_T$ inside the created fireball for a realistic shear viscosity. As one moves to the edge of the fireball, the pressure anisotropy increases. Such pressure anisotropies are an indication for large dissipative correction terms assumed to be at the starting point of perfect hydrodynamics. Furthermore, for a dissipative distribution function negative values are possible, which are unphysical regions in phase-space. Such unphysical regions may affect the calculation of several signatures, like dilepton production, quarkonia suppression or the freeze-out. This may lead to potential inaccuracies in the calculations. [19]

Such problems are motivating to create an alternative framework for describing dissipative dynamics, but also describe more accurately the dynamics of an anisotropic momentum distribution. A successful framework for accounting such properties is anisotropic hydrodynamics. One assumes that the distribution function $f(\mathsf{x}, \mathsf{p})$ allows an anisotropic momentum-space to leading order. This means that for a perfect isotropic distribution function f_0 with dissipative corrections δf the distribution function can be rewritten as

$$f(\mathsf{x}, \mathsf{p}) = f_0(\mathsf{x}, \mathsf{p}) + \delta f(\mathsf{x}, \mathsf{p}) = f_0\left(\frac{\sqrt{p^\mu \Xi_{\mu\nu}(\mathsf{x}) p^\nu}}{\Lambda(\mathsf{x})}\right), \tag{6.1}$$

with $\Xi_{\mu\nu}(\mathsf{x})$ the components of a second-rank tensor that is a reference for the amount of anisotropy in momentum-space and $\Lambda(\mathsf{x})$ a temperature-like scale which can be identified with the temperature T of an isotropic system. The most useful anisotropies are the spheroidal and the ellipsoidal forms. For the first one the spatial components of the energy-momentum tensor $T^{\mu\nu}$ to leading order are assumed to be $T^{xx} = T^{yy} \neq T^{zz}$ in the local rest frame. In the second form all three components are different $T^{xx} \neq T^{yy} \neq T^{zz}$. For the spheroidal case this means that $\Xi_{\mu\nu}(\mathsf{x})$ involves a single *anisotropy parameter* $\xi(\mathsf{x})$ such that $p^\mu \Xi_{\mu\nu}(\mathsf{x}) p^\nu$ is reduced to $p^\mu p_\mu +$

$\xi(x)p_z^2$ in the local rest frame. From here, the dynamical equations for spheroidal anisotropic hydrodynamics may be derived by taking equation (6.1) and using the zeroth and first moments of the Boltzmann equation in a relaxation time approximation (see section 3.5).

By using an anisotropic distribution function it is possible to account for dissipative terms in a non-perturbative approach[1]. In addition, the following benefits are achieved:

- For $\xi \to 0$ and $\Lambda \to T$ it reproduces the perfect hydrodynamics limit, corresponding to $\frac{\eta}{s} \to 0$
- Since $f_0 \geq 0$, the distribution function and all pressures are equal or greater than zero in contrast to first order dissipative corrections δf
- It is possible to show that for small anisotropies the formalism is reduced to second order dissipative hydrodynamics [40, 41]

We want to take a closer look at the motivation for anisotropic hydrodynamics in relativistic heavy-ion collisions. This motivation originates from [19].

Let us review the different stages of a relativistic heavy-ion collision (figure 6.1 on page 80). After the initial collision the created matter passes through several stages. First, there is the semi-hard particle production which is describable in terms of the color-glass-condensate (CGC). In the next step, the pre-equilibrium quark-gluon-plasma is reached, where in a small perimeter dissipative hydrodynamics should be applicable. After the pre-equilibrium, the equilibrium phase is reached and we traverse to the (dissipative) hydrodynamical regime. In the following the quark-gluon-plasma freezes out, first in the process of hadronization (chemical freeze-out) and finally in the (kinetic) freeze-out. In this process hydrodynamics ceases to be applicable.

We take a closer look at this evolution in terms of pressure anisotropy. Figure 6.2 on page 81 helps us to illustrate the pressure anisotropy $\mathcal{P}_L/\mathcal{P}_T$ at various stages in the quark-gluon-plasma. Here, we want to focus more on the later parts of this evolution. After the initial anisotropy with a significant value apart from one for $\mathcal{P}_L/\mathcal{P}_T$, the longitudinal expansion

[1] Although it is possible to add correction terms to the anisotropic distribution in (6.1), we will neglect such terms completely in this work.

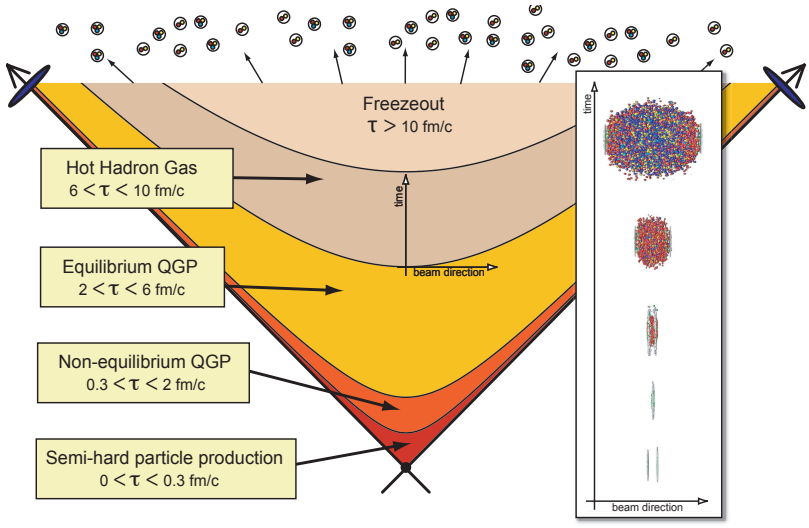

Figure 6.1: Schematic space-time history of the created matter in a relativistic heavy-ion collision at the LHC. The right overlay shows the laboratory frame evolution. [19]

is reduced and interactions between the constituents of the quark-gluon-plasma drive the system back towards an isotropic equilibrium. However, the system does not cease to expand longitudinally and the interactions may never fully restore isotropy. At late times the degree of the anisotropy in momentum-space should be set by the shear viscosity, indicated in figure 6.2. If the shear viscosity is large enough, one expects large non-equilibrium corrections and the need for an anisotropic description arises.

After this qualitative aspect, a quantitative aspect should also underline the need for anisotropic hydrodynamics. We follow again the arguments of [19] and look at a system that is transversely homogenous and boost invariant in the longitudinal direction. The dissipative hydrodynamics in chapter 3 (more precisely the relativistic Navier-Stokes equation) predicts, that in the local rest frame the corrections to the perfect pressures are diagonal. For the spatial components of the shear stress tensor $\pi^{\mu\nu}_{shear}$ the

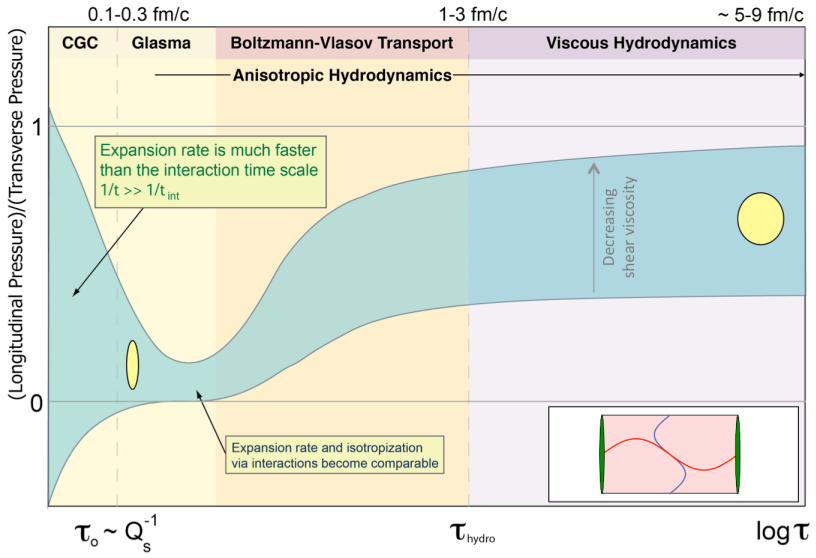

Figure 6.2: The temporal evolution of the momentum-space anisotropy evolution expected to be generated in relativistic heavy-ion collisions at the LHC. [19]

following relation holds

$$\pi^{zz}_{shear} = -2\pi^{xx}_{shear} = -2\pi^{yy}_{shear} = -\frac{4\eta}{3\tau}, \tag{6.2}$$

with η the already known shear viscosity and τ the proper time. In dissipative hydrodynamics, the longitudinal pressure is given by $\mathcal{P}_L = \mathcal{P} + \pi^{zz}_{shear}$ and the transverse pressure by $\mathcal{P}_T = \mathcal{P} + \pi^{xx}_{shear}$. If one assumes an ideal equation of state ($\epsilon = 3\mathcal{P}$), the ratio $\mathcal{P}_L/\mathcal{P}_T$ from first order dissipative hydrodynamics is given by

$$\frac{\mathcal{P}_L}{\mathcal{P}_T} = \frac{3\tau T - 16\bar{\eta}}{3\tau T + 8\bar{\eta}}, \tag{6.3}$$

with $\bar{\eta} = \eta/s$ and s the entropy density. For initial conditions at RHIC with $T_0 = 400\,\text{MeV}$ and $\tau_0 = 0.5\,\text{fm}$ and a conjectured lower bound of $\bar{\eta} = 1/4\pi$ [42], one finds that (6.3) is about 0.5. The initial conditions at

LHC with $T_0 = 600\,\mathrm{MeV}$ and $\tau_0 = 0.25\,\mathrm{fm}$ and taking $\bar{\eta} = 1/4\pi$ results in $\mathcal{P}_L/\mathcal{P}_T = 0.35$. Both results show that even in the best case scenario for $\bar{\eta} = 1/4\pi$, dissipative hydrodynamics itself predicts rather sizable momentum space anisotropies. Larger $\bar{\eta}$ result in even larger anisotropies. In addition, for a fixed value of τ the anisotropy increases when the temperature T is lowered.

In conclusion, the momentum-space anisotropies persist in the evolution of the quark-gluon-plasma and need to be taken into account in the dynamical description of relativistic heavy-ion collisions.

6.2 Anisotropic hydrodynamic fields

In this section we use the results from section 3.5 to calculate the particle number four-current $N^\mu(\mathsf{x})$ and the energy-momentum tensor $T^{\mu\nu}(\mathsf{x})$ for an anisotropic distribution function. The calculations were developed in cooperation with S. Feld and are originally presented in his master thesis [43].

6.2.1 Anisotropic distribution function

We start with the form (5.2) of the distribution function and expand it to the anisotropic case

$$f_a(\mathsf{x},\mathsf{p}) \propto \exp\left(-\frac{\sqrt{p^\mu \Xi_{\mu\nu}(\mathsf{x}) p^\nu}}{\Lambda(\mathsf{x})}\right). \tag{6.4}$$

This equation is further simplified by assuming that the scale $\Lambda(\mathsf{x})$ is independent of the space-time x. Λ takes the role of a parameter allowing us to tune possible results. Also, we assume that the anisotropic tensor $\Xi_{\mu\nu}(\mathsf{x})$ is symmetric, to assure that the argument of the exponential function is commuting. If $\Xi_{\mu\nu}(\mathsf{x})$ is symmetric, we can choose a basis in which the tensor is diagonal, reducing it to only four components. We also use $\mathsf{p}^2 = m^2$ to explicitly include the mass m of the fluid particles. Finally, for a purely spatial anisotropy, $\Xi_{00}(\mathsf{x})$ is assumed to be one and we define $\Xi_i(\mathsf{x}) \equiv 1 + \Xi_{ii}(\mathsf{x})$. With these assumptions we write

$$p^\mu \Xi_{\mu\nu} p^\nu = \left(p^0\right)^2 \Xi_{00} + \left(p^1\right)^2 \Xi_{11} + \left(p^2\right)^2 \Xi_{22} + \left(p^3\right)^2 \Xi_{33}$$

$$
\begin{aligned}
&= m^2\Xi_{00} + \left(p^1\right)^2(\Xi_{00}+\Xi_{11}) + \left(p^2\right)^2(\Xi_{00}+\Xi_{22}) \\
&\quad + \left(p^3\right)^2(\Xi_{00}+\Xi_{33}) \\
&= m^2 + \left(p^1\right)^2\Xi_1 + \left(p^2\right)^2\Xi_2 + \left(p^3\right)^2\Xi_3,
\end{aligned} \tag{6.5}
$$

where we dropped the x-dependence of the anisotropies $\Xi_{\mu\nu}$, respectively Ξ_i. The distribution function (6.4) can then be rewritten as

$$
f_a(\mathsf{x},\mathsf{p}) \propto \exp\left(-\frac{\sqrt{m^2 + (p^1)^2\,\Xi_1 + (p^2)^2\,\Xi_2 + (p^3)^2\,\Xi_3}}{\Lambda}\right). \tag{6.6}
$$

The form of (6.6) can be found in [10] and [44]. Due to the resemblance of Λ in (6.6) to the thermodynamic temperature, we call Λ simply the *anisotropic temperature*. From a thermodynamical point of view, this picture is wrong. However, if we set all Ξ_i to zero, Λ gains the role of the temperature T in equation (5.2), which justifies its name.

It is useful to change the spatial coordinates from the cartesian to the out-side-long coordinates introduced in section 2.3.3. In this coordinate system, every volume element dV is locally defined. For simplicity, we write: $o \mathrel{\hat{=}} out$, $s \mathrel{\hat{=}} side$ and $l \mathrel{\hat{=}} long$. The distribution function (6.6) changes to

$$
f_a(\mathsf{x},\mathsf{p}) \propto \exp\left(-\frac{\sqrt{m^2 + (p^o)^2\,\Xi_o + (p^s)^2\,\Xi_s + (p^l)^2\,\Xi_l}}{\Lambda}\right). \tag{6.7}
$$

6.2.2 Anisotropic particle number four-current

We start with $\mathsf{N}(\mathsf{x})$ from (3.36)

$$
N^\mu = \int \frac{d^3\vec{p}}{p^0} p^\mu f_a(\mathsf{x},\mathsf{p}). \tag{6.8}
$$

Note that the factor $1/(2\pi)^3$ is neglected in all calculations. We also rewrote p_0 to p^0. In Minkowski or the out-side-long coordinates this is a trivial step, but keep in mind that in other coordinate systems this may

not be the case. We apply f_a from (6.7) to equation (6.8) and calculate N^μ component-by-component, starting with N^0

$$N^0 = \int d^3\vec{p}\, \exp\left(-\frac{\sqrt{m^2 + (p^o)^2\,\Xi_o + (p^s)^2\,\Xi_s + (p^l)^2\,\Xi_l}}{\Lambda}\right). \tag{6.9}$$

The substitution $q^i = \sqrt{\Xi_i/\Lambda}\, p^i$ with $dq^i = \sqrt{\Xi_i/\Lambda}\, dp^i$ simplifies the integral and we replace the q^o and q^s coordinates by cylindric coordinates q and ϕ. The ϕ-integral simply yields 2π and also the q-integral is solvable

$$\begin{aligned} N^0 &= \frac{\Lambda^3}{\sqrt{\Xi_o\Xi_s\Xi_l}} \int d^3\vec{q}\, \exp\left(-\sqrt{\frac{m^2}{\Lambda^2} + (q^o)^2 + (q^s)^2 + (q^l)^2}\right) \\ &= \frac{\Lambda^3}{\sqrt{\Xi_o\Xi_s\Xi_l}} \int dq^l \int_0^\infty dq \int_0^{2\pi} d\phi\, q \exp\left(-\sqrt{\frac{m^2}{\Lambda^2} + q^2 + (q^l)^2}\right) \\ &= \frac{2\pi\Lambda^3}{\sqrt{\Xi_o\Xi_s\Xi_l}} \int dq^l \int_0^\infty dq\, q \exp\left(-\sqrt{\frac{m^2}{\Lambda^2} + q^2 + (q^l)^2}\right) \\ &= \frac{2\pi\Lambda^3}{\sqrt{\Xi_o\Xi_s\Xi_l}} \int dq^l \left(\sqrt{\frac{m^2}{\Lambda^2} + (q^l)^2} + 1\right) \exp\left(\sqrt{\frac{m^2}{\Lambda^2} + (q^l)^2}\right). \end{aligned} \tag{6.10}$$

The substitution $q^l = \sqrt{\frac{m^2}{\Lambda^2}}\sinh(r)$ with $dq^l = \sqrt{\frac{m^2}{\Lambda^2}}\cosh(r)dr$ results in

$$\begin{aligned} N^0 = \frac{4\pi\Lambda^2 m}{\sqrt{\Xi_o\Xi_s\Xi_l}} \Bigg[&\int_0^\infty dr \cosh(r) \exp\left(-\frac{m}{\Lambda}\cosh(r)\right) \\ &+ \frac{m}{\Lambda}\int_0^\infty dr \cosh^2(r) \exp\left(-\frac{m}{\Lambda}\cosh(r)\right)\Bigg]. \end{aligned} \tag{6.11}$$

The last integrals are solved by using the definition of the modified Besselfunction $K_\alpha(x)$

$$K_\alpha(x) = \int_0^\infty dt \cosh(\alpha t) \exp(-x\cosh(t)), \tag{6.12}$$

as well as the reciprocal relation for $K_\alpha(x)$

$$K_{n+1}(x) = K_{n-1}(x) + \frac{2n}{x} K_n(x) \tag{6.13}$$

and the identity $\cosh^2(r) = \frac{1}{2} + \frac{1}{2}\cosh(2r)$. The final result for N^0 is

$$\begin{aligned} N^0 &= \frac{4\pi\Lambda^2 m}{\sqrt{\Xi_o\Xi_s\Xi_l}}\left[K_1\left(\frac{m}{\Lambda}\right) + \frac{m}{2\Lambda}\left(K_2\left(\frac{m}{\Lambda}\right) + K_0\left(\frac{m}{\Lambda}\right)\right)\right] \\ &= \frac{2\pi\Lambda m^2}{\sqrt{\Xi_o\Xi_s\Xi_l}}\left[\frac{2\Lambda}{m}K_1\left(\frac{m}{\Lambda}\right) + K_2\left(\frac{m}{\Lambda}\right) + K_0\left(\frac{m}{\Lambda}\right)\right] \\ &= \frac{4\pi\Lambda m^2}{\sqrt{\Xi_o\Xi_s\Xi_l}}K_2\left(\frac{m}{\Lambda}\right). \end{aligned} \tag{6.14}$$

This is the same result as in [8] (page 110, formula 2.182), [10] (page 141, formula 8.56) or [45] (formula 28). The solution resembles the one for an isotropic perfect fluid, except for the square root of the anisotropies Ξ_i

$$N^0_{aniso}(\Lambda, \Xi_i) = \frac{1}{\sqrt{\Xi_o\Xi_s\Xi_l}}N^0_{iso}(\Lambda = T). \tag{6.15}$$

This behavior is a good argument for viewing Λ as a temperature. For the sake of completeness, we also show the result for N^0 in case of massless particles ($m = 0$)

$$\begin{aligned} N^0 &= \int d^3\vec{p}\,\exp\left(-\frac{\sqrt{(p^o)^2\,\Xi_o + (p^s)^2\,\Xi_s + (p^l)^2\,\Xi_l}}{\Lambda}\right) \\ &= \frac{\Lambda^3}{\sqrt{\Xi_o\Xi_s\Xi_l}}\int d^3\vec{q}\,\exp\left(-\sqrt{(q^o)^2 + (q^s)^2 + (q^l)^2}\right) \\ &= \frac{4\pi\Lambda^3}{\sqrt{\Xi_o\Xi_s\Xi_l}}\int_0^\infty dq\,q^2\exp\left(-q\right) \\ &= \frac{8\pi\Lambda^3}{\sqrt{\Xi_o\Xi_s\Xi_l}}. \end{aligned} \tag{6.16}$$

In the isotropic case ($\Xi_i = 1\ \forall\, i$) the known result $N^0 = 8\pi T^3$ is retrieved. Both results for massless particles coincide with [46] (formula 36 and 37).

The spatial components of N^μ are all solved in the same way, exemplified by N^o

$$N^o = \int \frac{d^3\vec{p}}{p^0}p^o\exp\left(-\frac{\sqrt{m^2 + (p^o)^2\,\Xi_o + (p^s)^2\,\Xi_s + (p^l)^2\,\Xi_l}}{\Lambda}\right). \tag{6.17}$$

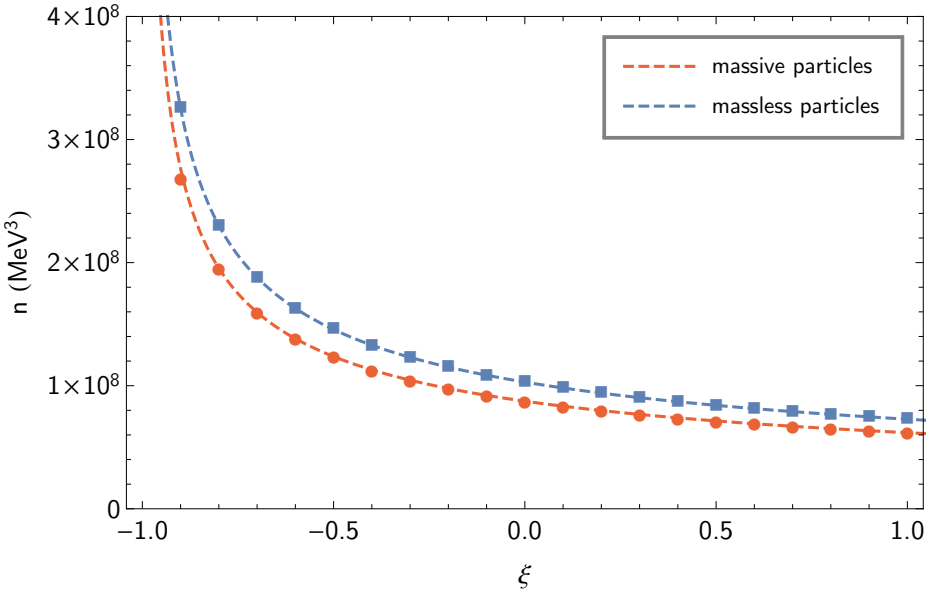

Figure 6.3: The particle density $N^0 = n$ in dependence of the anisotropy parameter ξ. The dots represent numeric calculations of (6.9) for massive particles, while the squares are the results of (6.9) for massless particles. The dashed lines are the analytic results (6.14) and (6.16). For the massive particles we chose pions ($m = 140\,\mathrm{MeV}$) and for Λ we chose 160 MeV.

The integral over p^o is equal to zero, because the integrand is a product of an even function ($(1/p^0) \cdot \exp(...)$) times an odd function (p^o) integrated over the whole integration region and consequently N^o is zero as well. The same symmetric argument is applied to N^s and N^l and for all spatial components we find

$$N^o = N^s = N^l = 0. \tag{6.18}$$

The result is unchanged if we switch to massless particles.

For a graphical representation of the equations (6.14) and (6.16), we set Ξ_s and Ξ_l to one and rewrite Ξ_o as $1 + \xi$ according to the simplification

made in section 6.2.1. This results in a lower bound for ξ:

$$N^0 \in \mathbb{R} \Leftrightarrow \xi > -1. \tag{6.19}$$

In figure 6.3 the massive and massless results for N^0 as a function of the anisotropy parameter ξ are presented. In both cases, we found two important properties: First, for a positive ξ the value for N^0 has only a small deviation compared to the isotropic ($\xi = 0$) case. Second, for a negative ξ, the value of N^0 grows significantly larger and is more sensitive to a variation of ξ.

6.2.3 Anisotropic energy-momentum tensor

The energy-momentum tensor is calculated by using formula (3.39)

$$T^{\mu\nu} = \int \frac{d^3\vec{p}}{p^0} p^\mu p^\nu f_a(\mathsf{x}, \mathsf{p}). \tag{6.20}$$

The 16 components of $T^{\mu\nu}$ are reduced to 4 components due to symmerty considerations. From (6.20) we already deduce that $T^{0i} = T^{i0}$ and $T^{ij} = T^{ji}$, which eliminates the first six components. Inserting f_a from (6.7) into (6.20) yields

$$T^{\mu\nu} = \int \frac{d^3\vec{p}}{p^0} p^\mu p^\nu \exp\left(-\frac{\sqrt{m^2 + (p^o)^2\,\Xi_o + (p^s)^2\,\Xi_s + (p^l)^2\,\Xi_l}}{\Lambda}\right). \tag{6.21}$$

For $\mu = 0$ and $\nu = i$ or $\mu = i$ and $\nu = j$, we deduce that the corresponding components vanish. Due to p^i being an odd function and the exponential function an even function, the integration over the whole integration region results in a zero value for these components. This leaves the diagonal components $\mu = \nu$ for an actual calculation

$$T^{\mu\mu} = \int \frac{d^3\vec{p}}{p^0} p^\mu p^\mu \exp\left(-\frac{\sqrt{m^2 + (p^o)^2\,\Xi_o + (p^s)^2\,\Xi_s + (p^l)^2\,\Xi_l}}{\Lambda}\right). \tag{6.22}$$

The different components are identified by their physical interpretation with $\epsilon = T^{00}$, $\mathcal{P}_o = T^{oo}$, $\mathcal{P}_s = T^{ss}$ and $\mathcal{P}_l = T^{ll}$.

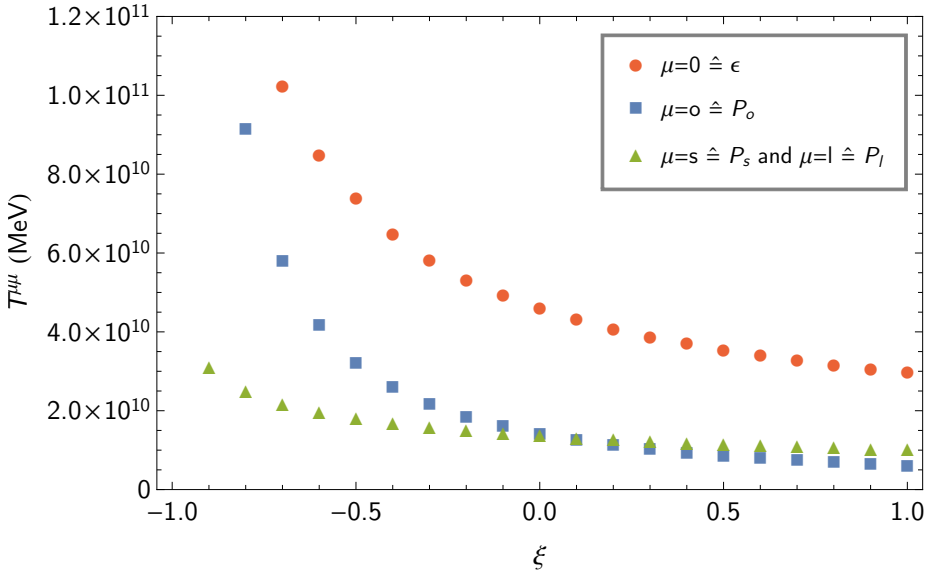

Figure 6.4: Numerical solution of (6.22) for $m = 140\,\mathrm{MeV}$ and $\Lambda = 160\,\mathrm{MeV}$ in dependence of ξ.

Unfortunately, for massive particles we need to exploit numerical integration to solve (6.22). The results[2] are presented in figure 6.4, where we chose the same values as above for N^0 ($\Xi_s = \Xi_l = 1$ and $\Xi_o = 1 + \xi$). The numerical calculations confirm our observations made for N^0. For negative ξ, the values of T^{00} and T^{oo} grow significantly larger. On the other hand, T^{ss} and T^{ll} do not change as much as the former two, simply because we set the corresponding anisotropies to one. It is notable, that the pressure in the out-direction $\mathcal{P}_o$ is larger than $\mathcal{P}_s$ and $\mathcal{P}_l$ for a negative ξ and smaller for positive ξ. All four results are consistent with the general relation that $T^{\mu\nu}$ is traceless, meaning that the sum $\mathcal{P}_o + \mathcal{P}_s + \mathcal{P}_l$ is equal to ϵ.

For massless particles ($m = 0$) it is possible to find a semi-analytic solution. We start with equation (6.22) for $\mu = 0$, which is simplified by

[2] The pressures $\mathcal{P}_s$ and $\mathcal{P}_l$ are identical and overlap in our calculation.

the same substitution already applied to N^0

$$T^{00} = \int d^3\vec{p}\, p^0 \exp\left(-\frac{\sqrt{(p^o)^2\,\Xi_o + (p^s)^2\,\Xi_s + (p^l)^2\,\Xi_l}}{\Lambda}\right)$$

$$= \int d^3\vec{p}\,\sqrt{(p^o)^2 + (p^s)^2 + (p^l)^2} \times \exp\left(-\frac{\sqrt{(p^o)^2\,\Xi_o + (p^s)^2\,\Xi_s + (p^l)^2\,\Xi_l}}{\Lambda}\right)$$

$$= \frac{\Lambda^4}{\sqrt{\Xi_o\Xi_s\Xi_l}} \int d^3\vec{q}\,\sqrt{\frac{(q^o)^2}{\Xi_o} + \frac{(q^s)^2}{\Xi_s} + \frac{(q^l)^2}{\Xi_l}} \times \exp\left(-(q^o)^2 - (q^s)^2 - (q^l)^2\right). \tag{6.23}$$

Further simplifications are achieved by changing the coordinate system to spherical coordinates in the out-side-long coordinate system. In the spherical coordinates (6.23) is rewritten to

$$T^{00} = \frac{\Lambda^4}{\sqrt{\Xi_o\Xi_s\Xi_l}} \int_0^\infty dq \int_0^\pi d\Theta \int_0^{2\pi} d\phi\; q^3 \sin(\Theta)\, \exp(-q)\, \sqrt{F(\Theta,\phi)}$$
$$= \frac{6\Lambda^4}{\sqrt{\Xi_o\Xi_s\Xi_l}} \int_0^\pi d\Theta \int_0^{2\pi} d\phi\; \sin(\Theta)\, \sqrt{F(\Theta,\phi)}, \tag{6.24}$$

where the function $F(\Theta,\phi)$ is introduced as

$$F(\Theta,\phi) = \frac{\sin^2(\Theta)\cos^2(\phi)}{\Xi_o} + \frac{\sin^2(\Theta)\sin^2(\phi)}{\Xi_s} + \frac{\cos^2(\Theta)}{\Xi_l}. \tag{6.25}$$

Replacing Ξ_i with $1 + \xi_i$ yields the same form as in [46] (formula 57). Unfortunately, the angular integrals have in general no analytical solution and we have to fall back to numerical integration. By setting all Ξ_i to one and replacing Λ by T, the function $F(\Theta,\phi)$ is equal to one and we find the isotropic solution for T^{00} [46]

$$T^{00} = 24\pi T^4. \tag{6.26}$$

The three pressures $\mathcal{P}_o$, $\mathcal{P}_s$ and $\mathcal{P}_l$ are calculated in the same way as for T^{00}, exemplified for $\mathcal{P}_o$

$$\begin{aligned}
T^{oo} &= \int \frac{d^3\vec{p}}{p^0} p^o p^o \exp\left(-\frac{\sqrt{(p^o)^2\,\Xi_o + (p^s)^2\,\Xi_s + (p^l)^2\,\Xi_l}}{\Lambda}\right) \\
&= \int \frac{d^3\vec{p}}{\sqrt{(p^o)^2 + (p^s)^2 + (p^l)^2}} p^o p^o \\
&\qquad\qquad \times \exp\left(-\frac{\sqrt{(p^o)^2\,\Xi_o + (p^s)^2\,\Xi_s + (p^l)^2\,\Xi_l}}{\Lambda}\right) \\
&= \frac{\Lambda^4}{\sqrt{\Xi_o^3 \Xi_s \Xi_l}} \int d^3\vec{q} \frac{q^o q^o}{\sqrt{\frac{(q^o)^2}{\Xi_o} + \frac{(q^s)^2}{\Xi_s} + \frac{(q^l)^2}{\Xi_l}}} \exp\left(-(q^o)^2 - (q^s)^2 - (q^l)^2\right) \\
&= \frac{\Lambda^4}{\sqrt{\Xi_o^3 \Xi_s \Xi_l}} \int_0^\infty dq \int_0^\pi d\Theta \int_0^{2\pi} d\phi\, q^3 \exp(-q) \frac{\sin^3(\Theta)\cos^2(\phi)}{\sqrt{F(\Theta,\phi)}} \\
&= \frac{6\Lambda^4}{\sqrt{\Xi_o^3 \Xi_s \Xi_l}} \int_0^\pi d\Theta \int_0^{2\pi} d\phi \frac{\sin^3(\Theta)\cos^2(\phi)}{\sqrt{F(\Theta,\phi)}}
\end{aligned} \tag{6.27}$$

$\mathcal{P}_s$ and $\mathcal{P}_l$ have similar results

$$T^{ss} = \frac{6\Lambda^4}{\sqrt{\Xi_o \Xi_s^3 \Xi_l}} \int_0^\pi d\Theta \int_0^{2\pi} d\phi \frac{\sin^3(\Theta)\sin^2(\phi)}{\sqrt{F(\Theta,\phi)}} \tag{6.28}$$

$$T^{ll} = \frac{6\Lambda^4}{\sqrt{\Xi_o \Xi_s \Xi_l^3}} \int_0^\pi d\Theta \int_0^{2\pi} d\phi \frac{\sin(\Theta)\cos^2(\Theta)}{\sqrt{F(\Theta,\phi)}}, \tag{6.29}$$

where $F(\Theta,\phi)$ is the same function as in equation (6.25). These results are compatible with the results in [46] (formula 60).

In the last step, the angular integrals of (6.24), (6.27), (6.28) and (6.29) are solved numerically to gain a functional form. Again, we choose Ξ_s and Ξ_l to be one and the remaining anisotropy Ξ_o is set to $1+\xi$. The results are shown in figure 6.5, where we find the same qualitative results already found for massive particles.

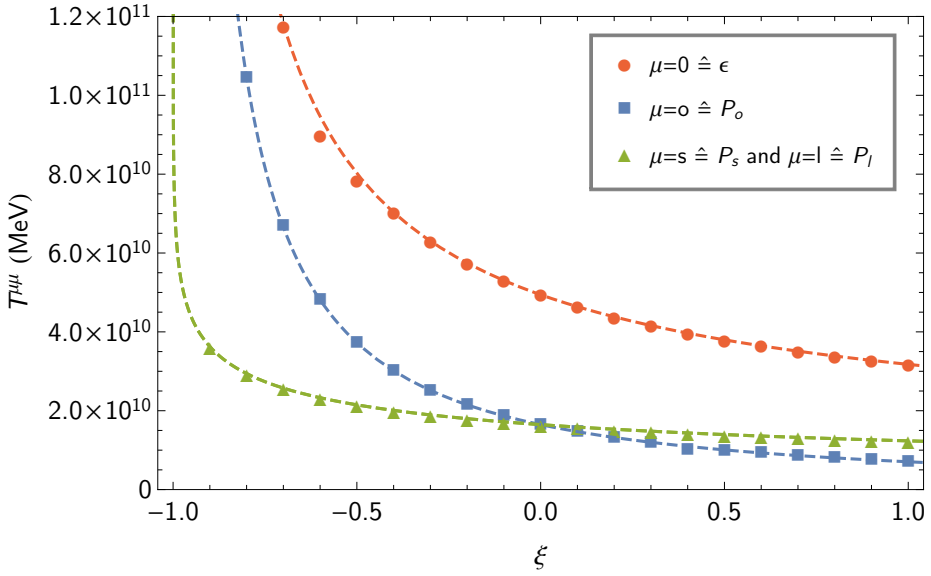

Figure 6.5: Semi-analytical solutions for (6.24), (6.27), (6.28) and (6.29) for $\Lambda = 160\,\mathrm{MeV}$ in dependence of ξ (dashed lines). The points represents exact numerical results of (6.22) for massless particles.

The results in this chapter may seem unimportant for the freeze-out, where N^μ and $T^{\mu\nu}$ do not contribute, but we gain insight into the effectiveness of the anisotropy on hydrodynamic quantities. Especially, the behavior of the pressure $\mathcal{P}_o$ in dependence of ξ has the remarkable property, that a negative anisotropy shifts $\mathcal{P}_o$ to larger values, while the other pressures are, compared to $\mathcal{P}_o$, are hardly affected by the anisotropy ξ.

7 Anisotropic corrections to the freeze-out

We return to chapter 5 with the sudden freeze-out approximation and the Cooper-Frye formula

$$E_{\vec{p}} \frac{d^3N}{d^3\vec{p}} = \frac{g}{(2\pi)^3} \int_\Sigma d\sigma_\mu(x)\, p^\mu f\left(\mathsf{x}, \mathsf{p}\right). \tag{7.1}$$

In the sudden freeze-out approximation the fluid breaks up abruptly when it reaches the hypersurface Σ. In chapter 5 this happens when a certain temperature is reached ($T = 160\,\mathrm{MeV}$). It is possible to make the process a little less abrupt, if the "thin" region of the hypersurface is replaced by a four-dimensional shell to weaken the abruptness of the process. However, there is still the problem that the freeze-out has to start somewhere in the phase-space and the problem of an abrupt transition persists.

Apart from the problem, **when** the transition takes place, we also have to ask **how** the transition proceeds. In chapter 4 and 5, we assumed an equilibrium thermal distribution for the fluid in the case of a perfect fluid or a near-equilibrium distribution including correction terms in case of a dissipative fluid. In both cases it has been assumed, explicitly or implicitly, that the fluid is not far away from the local thermal equilibrium to assure that the dissipative effects remain small. Determining the corrections may be achieved by pure theory (see again [20–28]) or by phenomenological data-driven approaches [29], and is an ongoing effort.

The distribution $f\left(\mathsf{x}, \mathsf{p}\right)$ at the freeze-out considered in the literature is isotropic in the local rest frame of the fluid, a reflection of the (near) local thermal equilibrium. In this chapter we depart from the local isotropy and assume instead a locally asymmetric (anisotropic) momentum distribution for the fluid at the freeze-out.

Before proceeding any further, we want to mention that the existence of a local anisotropy at freeze-out was already considered in [47]. However,

we are interested in a different kind of anisotropy, reflecting the dissimilar underlying motivation. Nevertheless, some of the results of [47] naturally translate into similar results in our case.

The content of this chapter has also been published in the following article: [48].

7.1 Motivation

The sudden freeze-out scenario within the Cooper-Frye prescription aims at joining two different descriptions together. The mismatch of the model is obvious when the fluid freezes out into the free-streaming particles, exemplified by the jump of the Knudsen-number (see equation (3.1)) from very small values (fluid) to very large values (free particles). Even when the Cooper-Frye formula is used to switch from a dissipative fluid to a collection of hadrons, some issues remain [13, 49].

An often mentioned problem is the existence of regions on the hypersurface Σ where $d\sigma_\mu(\mathsf{x})d\sigma^\mu(\mathsf{x}) < 0$, which can lead to negative contributions to the Cooper-Frye integral, as it has been mentioned in section 6.1. Solutions have been proposed in [50], which themselves remain incomplete since they introduce discontinuities across Σ either in the stress tensor or in the four-velocity. These discontinuities are only mathematical artifacts of the modeling process and no physical manifestations.

Another issue of the usual sudden freeze-out approximation is the sensitivity of the observables computed with the emitted particles. In particular their spectra is sensitive to the parameters in the Cooper-Frye formula (7.1). This rather crucial point implies, that the matching between a microscopic approach (kinetic description of the particles) and a macroscopic effective theory (fluid description) depends significantly on the parameter that separates them, making the whole process questionable. A strong theoretical incentive for developing and investigating new approaches to the modeling of decoupling at the end of the dynamical stages of relativistic heavy-ion collisions is thus to obtain a description, which interpolates between the hydrodynamic and kinetic regimes in a smoother manner than the usual prescriptions.

There is of course the possibility to find a way out of the problem by dropping the assumption of a sudden freeze-out in favor of a continuous

freeze-out [51–53]. In the current implementation of this approach, the particles decouple from the fluid and are not interacting with each other after this process. Unfortunately, this implies a sudden transition from a very small to a very large (infinitely) mean free path length for each particle, which is again unsatisfactory, even though it does not happen "at once" for the whole fluid.

Despite the mentioned discrepancies, the Cooper-Frye formula remains appealing because of its simplicity, which makes it easier to test new ideas. We want to ensure a better transition between the fluid and particle description, so it seems promising to tweak one of the models in order to bring them closer together. We suggest that the anisotropic hydrodynamics [40, 54, 55] may improve the smoothness of the transition between the fluid and the particle framework. As we shall demonstrate in section 7.2, this ansatz diminishes the sensitivity to the freeze-out temperature T. We introduce control parameters, namely those governing the anisotropy of the phase-space distribution at decoupling, which widen the possible range of values for T. Three arguments in favor of distorting the particle distribution at freeze-out are:

1. In the context of heavy-ion physics there is an obvious analogy with the advocated use of anisotropic hydrodynamics at early stages of the evolution of the medium. It is used to ease the transition from the locally asymmetric energy-momentum tensor of the fields left by the colliding nuclei to the almost isotropic tensor needed to apply usual hydrodynamics consistently. In the early evolution stage, the phase-space distribution is deformed along the axis of the nucleus-nucleus collision (z-axis). However, for our case we do not expect such a global direction for the anisotropy.

2. As a matter of fact, our resort to a possibe strongly anisotropic freeze-out distribution is the observation of a similar asymmetry, parameterized as two different translation temperatures along the streamlines and perpendicular to them, in hypersonic non-relativistic flows [56]. These observations help us specify the kind of anisotropy we want to consider hereafter. Let us for simplicity focus on particle emission around mid-rapidity to discard any anisotropy along the z-direction on symmetry grounds. Far from the fluid, each particle will

tend to fly away radially, as implied by the simultaneous conservation of angular momentum and (kinetic) energy. The dispersion of the momentum components transverse to the radial direction will thus be much smaller than that of the radial component.

3. Eventually, the argument for assuming a deformed particle distribution is that such an anisotropy was actually found for post-freeze-out distributions arising from the decoupling through time-like portions of freeze-out hypersurfaces [28, 57].

We conclude that it would be helpful to adopt a particle distribution which is already deformed with a larger mean squared momentum along the radial direction in the Cooper-Frye description. If we adopt the out-side-long coordinate system, we assume a larger pressure along the local out-direction than in the side- and long-directions, motivated by the results in section 6.2. The asymmetry is admittedly a mere assumption, motivated by non-relativistic studies where the freeze-out happens when the local particle distribution has a large enough anisotropy in momentum-space, and by the incentive to have a smoother transition between the fluid and particle descriptions. The actual functional form of the phase-space distribution at freeze-out, as well as the size of the parameters measuring the anisotropy, should emerge from a detailed kinetic description of the decoupling process [58]. In section 7.2, we postulate such a form and examine the change induced by the momentum-space asymmetry on various observables of relativistic heavy-ion collisions.

One last remark: Note that the anisotropy we consider hereafter differs from that considered in [47], in which the distribution is assumed to be distorted along the z-axis, as a remnant of the distortion along that direction in the initial state of the heavy-ion collision. Both deformations can naturally be present at once, yet our intention here is to examine the influence of a larger radial momentum dispersion, so that we keep the pressures in the side- and long-directions equal.

7.2 Freeze-out of an anisotropic fluid

We propose that for the phase-space distribution at the freeze-out of a particle species with mass m a Romatschke-Strickland-like profile can be assumed [59], which is similar to the distribution used in chapter 6. In the local rest frame the distribution should take the following form

$$f_{a,LR}(\mathsf{x},\mathsf{p};\Lambda,\xi) = \exp\left(-\frac{\sqrt{m^2+\vec{p}_{LR}^{\,2}+\xi(\mathsf{x})p_{out,LR}^2}}{\Lambda(\mathsf{x})}\right), \tag{7.2}$$

where $p_{out,LR}$ denotes the out-component of the particle momentum $\vec{p}_{LR}$ with respect to the local rest frame of the fluid at position x. $\Lambda(\mathsf{x})$ is again a temperature-like scale over which the particle momentum takes significant values and $\xi(\mathsf{x})$ characterizes the anisotropy in the out-direction. A priori, both $\Lambda(\mathsf{x})$ and the anisotropy parameter $\xi(\mathsf{x})$ depend on their position in space-time as well as the particle type, but for simplicity we treat them as parameters and they are assumed to be constant over the freeze-out hypersurface Σ. Obviously, (7.2) does not include quantum effects.

In the same way as in section 6.2, the anisotropy parameter ξ must be larger than -1, to ensure the positivity of the expression under the square root. In order to obtain a larger pressure along the radial direction than perpendicular to it, ξ should be negative. Therefore, ξ has to be in the range of $-1 < \xi < 0$.

To test the influence of the momentum anisotropy in equation (7.2), we assume some specific freeze-out flow profile $\mathsf{u}(\mathsf{x})$ and hypersurface Σ. We let the fluid decouple like in chapter 5 at a constant proper time τ_{fo} on a longitudinally infinite, azimuthally symmetric cylinder of radius R. The coordinates in the laboratory frame are the proper time τ, space-time rapidity η, and cylindrical coordinates r and ϕ. We also assume for the fluid velocity on Σ a generalized blast-wave profile [36, 37]

$$u^r(r,\phi) = \overline{u}_{max}\frac{r}{R}\left(1+2\sum_{n\geq 1}V_n\cos\left(n\phi\right)\right) \tag{7.3}$$

for the radial coordinate, $u^\phi = u^\eta = 0$ for the azimuthal- and rapidity-direction and eventually $u^\tau(r,\phi) = \sqrt{1+(u^r(r,\phi))^2}$. With this choice,

the phase-space distribution (7.2) is written in the laboratory frame as

$$f_a(\mathsf{x}, \mathsf{p}; \Lambda, \xi) = \exp\left(-\frac{\sqrt{[p^\tau u^\tau(\mathsf{x}) - p^r u^r(\mathsf{x})]^2 + \xi[p^r u^\tau(\mathsf{x}) - p^\tau u^r(\mathsf{x})]^2}}{\Lambda}\right). \tag{7.4}$$

Equation (7.4) is achieved by rewriting $m^2 + \vec{p}_{LR}^{\,2}$ and $p_{out,LR}$.

First, $p^\tau u^\tau(\mathsf{x}) - p^r u^r(\mathsf{x})$ is found by writing $m^2 + \vec{p}_{LR}^{\,2} = \left(p^0_{LR}\right)^2$. In the local rest frame $\mathsf{u}(\mathsf{x})$ is $(1,0,0,0)$, which allows us to write $p^0_{LR} = (p^\mu u_\mu(\mathsf{x}))_{LR}$ and holds automatically in every reference frame, so that we can write $(p^\mu u_\mu(\mathsf{x}))_{LR} = (p^\mu u_\mu(\mathsf{x}))$. For our choice of $\mathsf{u}(\mathsf{x})$ from above we find $(p^\mu u_\mu(\mathsf{x})) = p^\tau u^\tau(\mathsf{x}) - p^r u^r(\mathsf{x})$.

The second squared bracket is found by boosting $p_{out,LR}$ along the u^r-direction[1]: $p^r \to p'^r = \gamma(\mathsf{x})\,(p^r - \beta(\mathsf{x}) p^\tau)$. In our cylindrical coordinate system, $\gamma(\mathsf{x})$ is equal to $u^\tau(\mathsf{x})$ and $\beta(\mathsf{x})$ is equal to $u^r(\mathsf{x})/u^\tau(\mathsf{x})$, which results in $p'^r = (p^r u^\tau(\mathsf{x}) - p^\tau u^r(\mathsf{x}))$.

Under these assumptions we compute the Cooper-Frye integral numerically, from which we obtain the transverse momentum spectrum, respectively the particle momentum spectrum, the anisotropic flow coefficients v_n, and the three HBT-radii R_{out}, R_{side} and R_{long} [26, 60]. The HBT-radii are computed with formula (2.41), while the v_n are computed with equation (2.10). We will focus on pions ($m = 140\,\mathrm{MeV}$) produced at mid-rapidity ($y \approx 0$).

7.2.1 Effects for a fixed anisotropic temperature

First, we present results obtained with fixed values of the anisotropic temperature $\Lambda = 150\,\mathrm{MeV}$ and the following parameters of the blast-wave profile: $\tau_{fo} = 7.5\,\mathrm{fm}$, $R = 10\,\mathrm{fm}$, $\overline{u}_{max} = 1$, $V_2 = V_3 = 0.05$ and all other $V_n = 0$. The HBT-radii are an exception where all V_n are set to zero. In contrast, the anisotropy parameter ξ varies and we use values from -0.5 to 0 in steps of 0.1 and include the positive values $\xi = 0.15$ and $\xi = 0.3$. According to our argumentation in section 7.1, these positive values, which lead to a smaller pressure in radial direction as perpendicular to it, should not be relevant for the freeze-out, yet we conclude them for the sake of reference.

[1] Note that the *out*-direction and the r-direction coincide here.

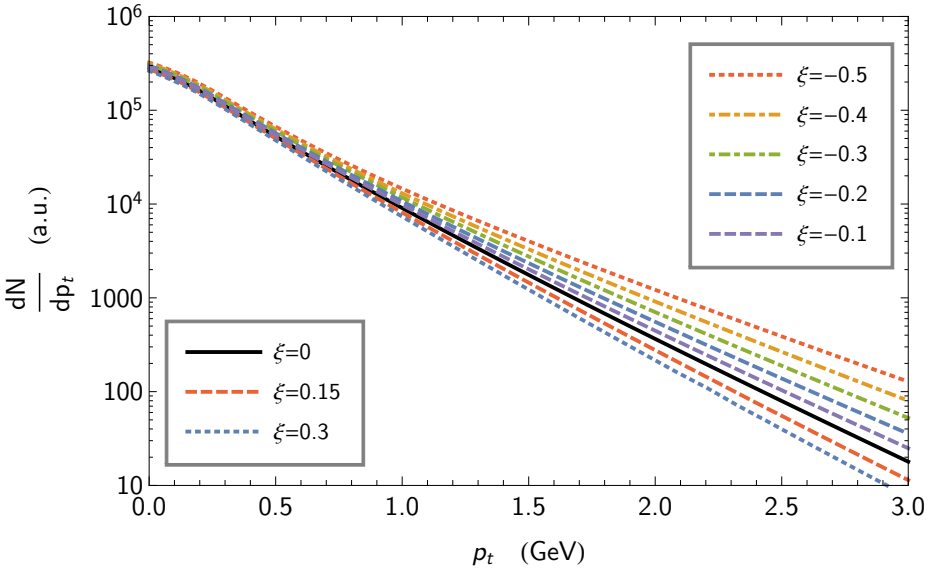

Figure 7.1: Transverse spectra for fixed Λ and varying anisotropy parameter ξ.

We start with the results of the transverse momentum spectra, which are equivalent to formula (7.1) for neglected y and φ, in figure 7.1. As it is expected, the non-zero values of ξ lead to deviations from the almost exponential shape valid in the isotropic case. While for low p_t up to 0.5 GeV almost no deviations from the isotropic spectrum are present, the spectrum becomes harder for high p_t, meaning the spectrum raises at larger values of p_t when ξ goes to increasingly negative values. This clearly reflects the growing radial pressure, or equivalently the effective radial temperature $\mathcal{T}$

$$\mathcal{T} = \Lambda/\sqrt{1+\xi}, \tag{7.5}$$

obtained by assuming $-1 < \xi < 0$.

Figure 7.2 on page 100 displays the transverse momentum dependence of the elliptic flow $v_2(p_t)$ for various ξ. The triangular flow $v_3(p_t)$ follows the same trend, also seen in figure 7.2. We conclude from both graphics that the anisotropic flow decreases when ξ becomes more negative. At

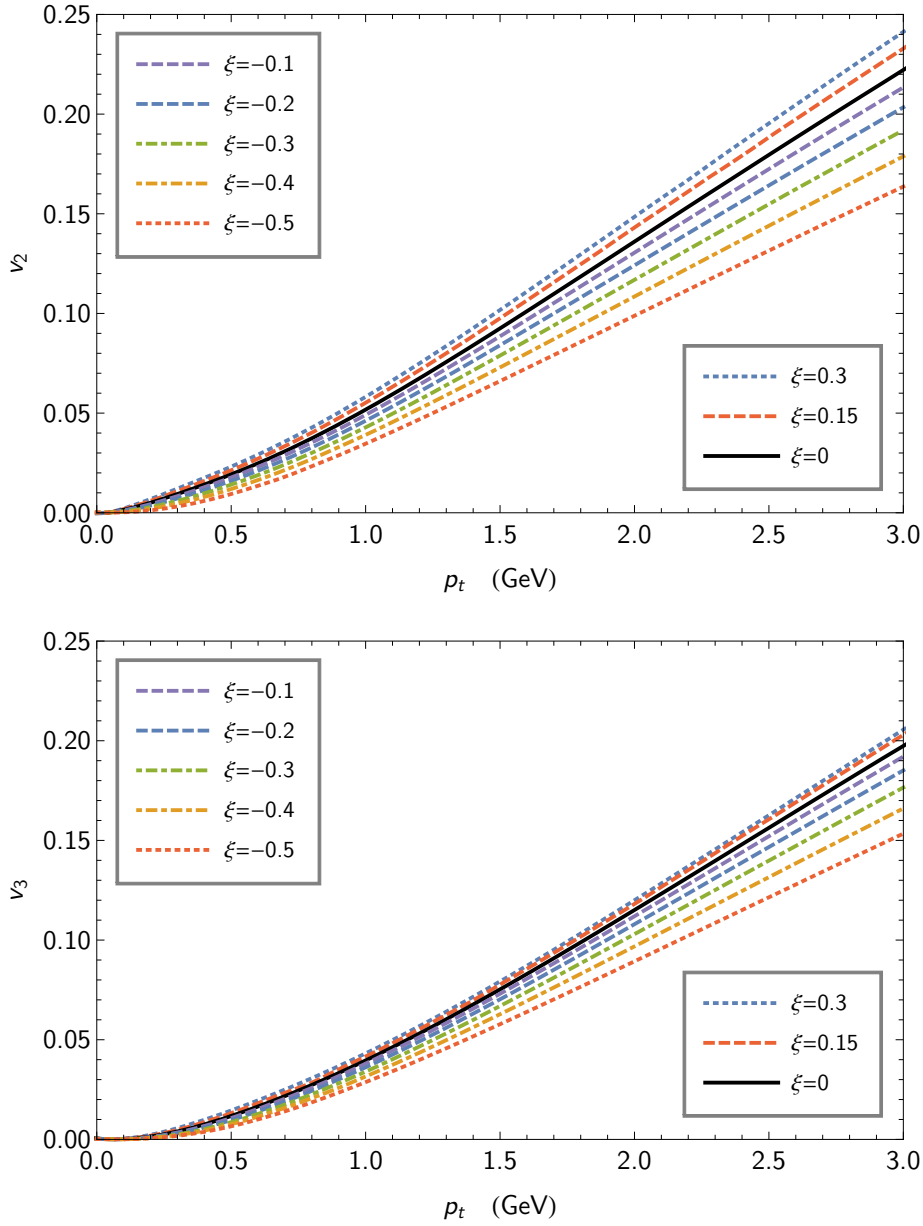

Figure 7.2: Elliptic flow $v_2(p_t)$ and triangular flow $v_3(p_t)$ for fixed Λ and varying anisotropy parameter ξ.

the same time the radial temperature $\mathcal{T}$ grows. This behavior reflects the fact that an increase in random thermal motion tends to dilute the effect of directed collective behavior encoded in the flow velocity and its anisotropies and therefore diminishes the values of the flow coefficients $v_n(p_t)$, here exemplified by $v_2(p_t)$ and $v_3(p_t)$.

Finally, the HBT-radii, are shown in figure 7.3 and 7.4 on pages 102 and 103, together with the ratio $R_{out}(K_t)/R_{side}(K_t)$, as functions of the pair transverse momentum K_t. To be more precise, the radii $R^2_{side}(K_t)$ and $R^2_{long}(K_t)$ are the weighted averages with f_a from equation (7.4) over the freeze-out hypersurface of $y^2 = r^2 \sin^2\phi$, respectively $z^2 = \tau^2 \sinh^2\eta$, while $R^2_{out}(K_t)$ is the average of $(x - (K_t/E_{\vec{K}})t)^2$, where $x = r\cos\phi$ and $t = \tau\cosh\eta$ (see also the formulas in (2.41)). As it was just mentioned, negative values of ξ amount to a larger radial temperature $\mathcal{T}$ and thus to higher thermal velocities in the out-direction. Since the emission duration at the same time barely changes, this naturally leads to a larger $R_{out}(K_t)$ (see figure 7.3), as well as to a larger ratio $R_{out}(K_t)/R_{side}(K_t)$ (see figure 7.4). In turn, the longitudinal radius $R_{long}(K_t)$ shown in figure 7.4 is to a large extent unaffected by ξ. This could be anticipated since the longitudinal part of the occupation factor remains unchanged. The behavior of the sidewards radius $R_{side}(K_t)$ with varying ξ (see figure 7.3) is more complicated without finding a satisfactory explanation describing all its details.

Before we go any further, one should note that in a more complete approach, the local anisotropy parameterized in this work by ξ should not be uniform, but rather position-dependent. In particular, ξ (or similar parameters) would normally be a function of the azimuthal angle ϕ, paralleling the corresponding dependence of the velocity profile, as we now argue[2]. The fluid-particle conversion, whose modeling ξ is supposed to facilitate, roughly happens when the fluid expansion rate $\nabla_\mu(\mathsf{x})u^\mu(\mathsf{x})$ becomes comparable to that of elastic scatterings. Since the flow velocity varies with ϕ, so does the expansion rate, which motivates the azimuthal dependence of ξ. On the other hand, the scattering rate depends on the particle density obtained by integrating the occupancy factor over momentum, and on the relative velocity of the particles. As follows from a

[2]Similarly, Λ also might depend on ϕ, yet we leave this possibility aside to simplify the discussion.

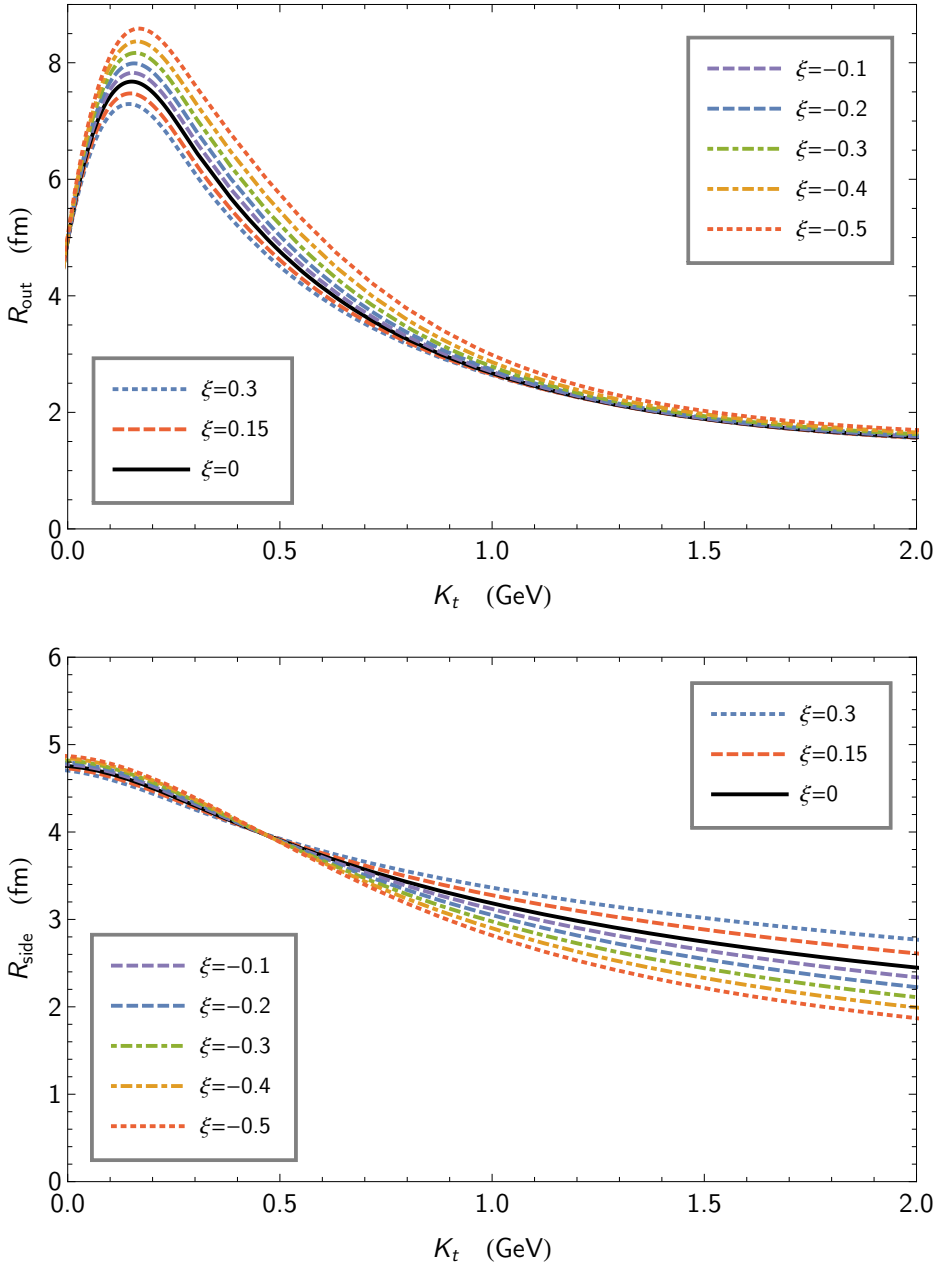

Figure 7.3: HBT-radii $R_{out}(K_t)$ and $R_{side}(K_t)$ for fixed Λ and variable anisotropy parameter ξ.

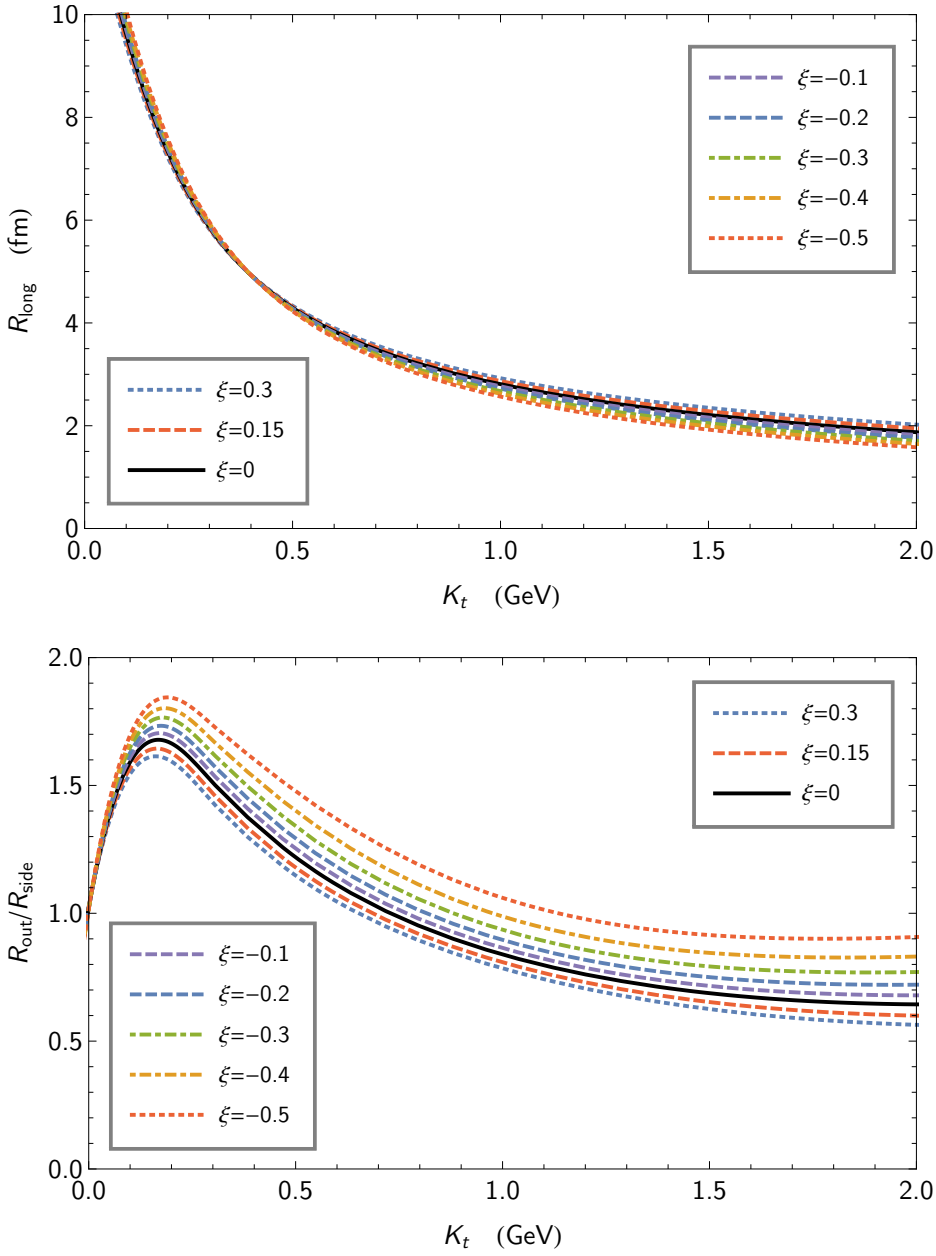

Figure 7.4: HBT-radius $R_{long}(K_t)$ and the ratio $R_{out}(K_t)/R_{side}(K_t)$ for fixed Λ and varying anisotropy parameter ξ.

straightforward change of the integration variable [47], the density is inversely proportional to $\sqrt{1+\xi(x)}$, thus is a priori ϕ-dependent. In turn, the typical relative velocity is controlled by the (effective) temperature(s) of the decoupling medium and thus a function of ϕ as well. All in all, every relevant physical quantity depends on the azimuth angle which results in a non-trivial description of the ϕ-dependence to determine the actual dependence of ξ. In any case, there will be such a dependence, which will affect the anisotropic flow coefficients v_n. The results shown in figure 7.2 and also figure 7.6 are obviously neglecting this feature.

7.2.2 Effects for a variable anisotropic temperature

After investigating the influence of ξ when all other parameters are fixed, we want to illustrate the degeneracy introduced by the new parameter Λ, showing that very similar values of the observables can be obtained with different pairs (Λ, ξ). Note that we did not attempt to optimize the results we are showing by fine tuning parameters[3], as it will be made apparent by the values of the latter.

We show the transverse momentum spectra for four sets of values of (Λ, ξ), where Λ varies between 130 MeV and 160 MeV and ξ between -0.5 and 0.3, in figure 7.5. In all four cases, we have chosen the same values for the other parameters, in particular $\overline{u}_{max} = 1$. We find that all curves are barely distinguishable below $p_t = 1.5\,\mathrm{GeV}$, while for larger p_t the one with $(\Lambda = 130\,\mathrm{MeV}, \xi = -0.5)$ starts curving up. The spectrum for $(\Lambda = 140\,\mathrm{MeV}, \xi = -0.25)$ only starts to differ from those with larger Λ from about 2 GeV onwards, while the remaining two stay very close together up to at least 3 GeV. In the same figure the spectrum for $(\Lambda = 130\,\mathrm{MeV}, \xi = -0.5)$ is shown, but with a different flow velocity, namely $\overline{u}_{max} = 0.8$. The change in $\overline{u}_{max}$ makes the spectrum almost coincide with the one for $(\Lambda = 150\,\mathrm{MeV}, \xi = 0)$, with a relatively small difference over the whole momentum range.

The elliptic flow $v_2(p_t)$ and the triangular flow $v_3(p_t)$ for the same set of parameters as in figure 7.5 are shown in figure 7.6 on page 106. The three HBT-radii $R_{out}(K_t)$, $R_{side}(K_t)$ and $R_{long}(K_t)$ are also shown in figure 7.7 on page 107 and figure 7.8 on page 108, again for the same set of

[3] An attempt to optimize the results is presented in the master's thesis by S. Feld [43].

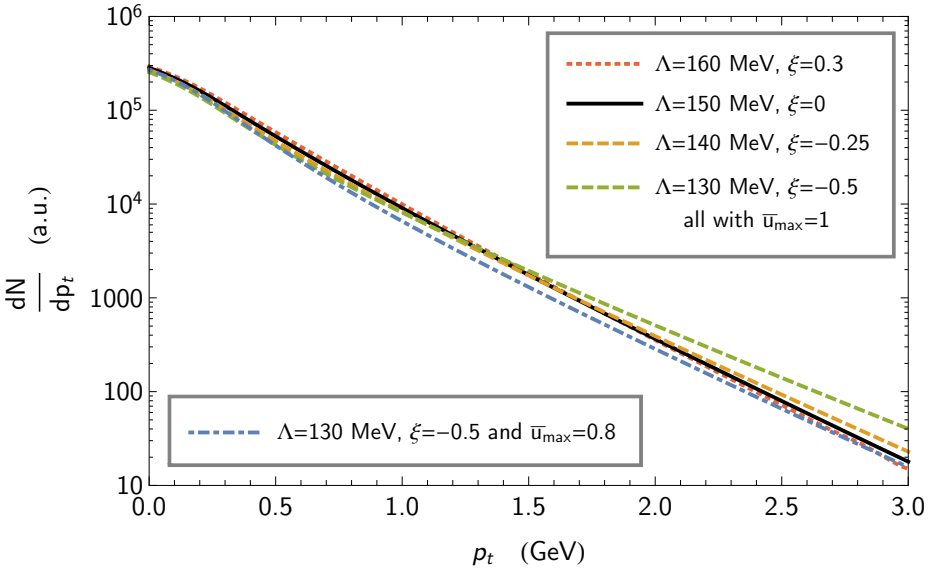

Figure 7.5: Transverse spectra for different choices of Λ, ξ, and $\overline{u}_{max}$.

parameters as before.

As in the case of the transverse spectra, the values for $v_2(p_t)$ (figure 7.6) and $R_{out}(K_t)$ (figure 7.7) for all pairs of (Λ, ξ) with $\overline{u}_{max} = 1$ are very close to each other, with $(\Lambda = 130\,\text{MeV}, \xi = -0.5)$ once more being the farthest apart from the other three. Also included is the calculation with $\overline{u}_{max} = 0.8$, which provides a good approximation for the transverse momentum spectrum. For $v_2(p_t)$ it basically makes no difference with respect to the case $\overline{u}_{max} = 1$, whereas the departure is more marked for $R_{out}(K_t)$. All in all, the results for the transverse momentum spectra, $v_2(p_t)$, and $R_{out}(K_t)$ support our claim that introducing extra parameters opens a much wider range for the freeze-out temperature Λ without drastically affecting the values of the two observables.

In contrast, the sidewards HBT-radius $R_{side}(K_t)$ displayed in figure 7.7 is much more sensitive to the choice of the decoupling parameters (Λ, ξ). This is actually somewhat reassuring, since femtoscopic measurements are precisely designed to probe the space-time configuration at decoupling [61].

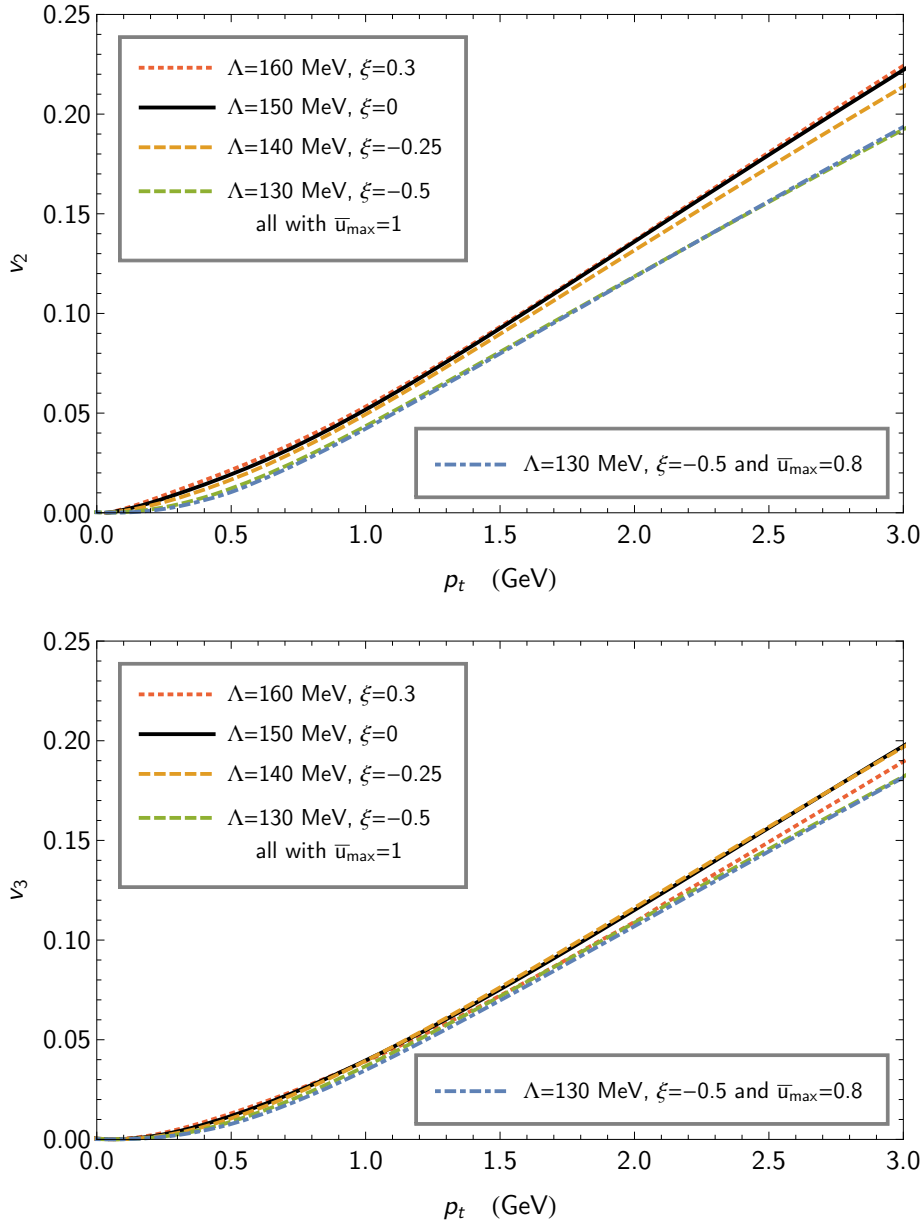

Figure 7.6: Elliptic flow $v_2(p_t)$ and triangular flow $v_3(p_t)$ for different choices of Λ, ξ, and $\overline{u}_{max}$.

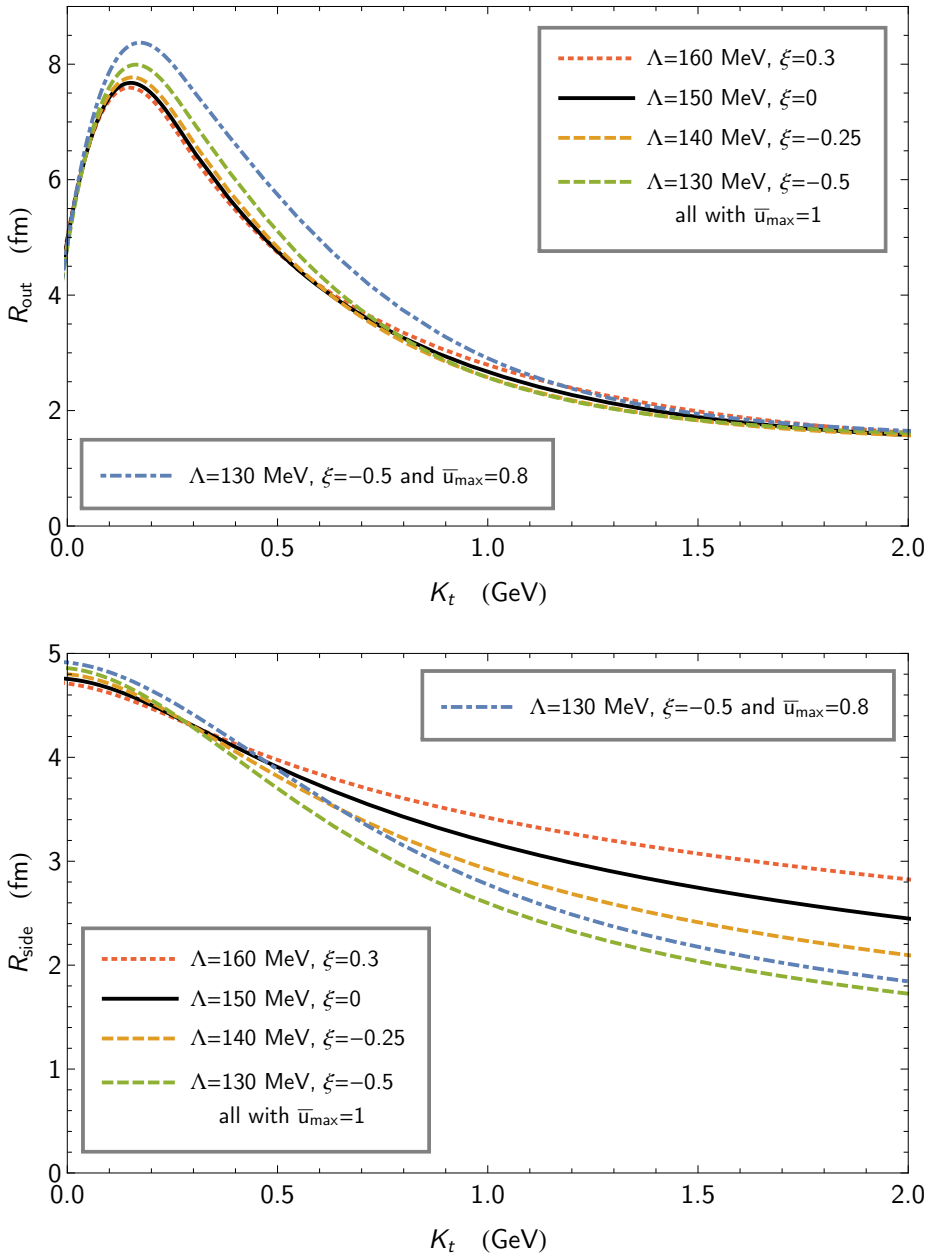

Figure 7.7: HBT-radii $R_{out}(K_t)$ and $R_{side}(K_t)$ for different choices of Λ, ξ, and $\overline{u}_{max}$.

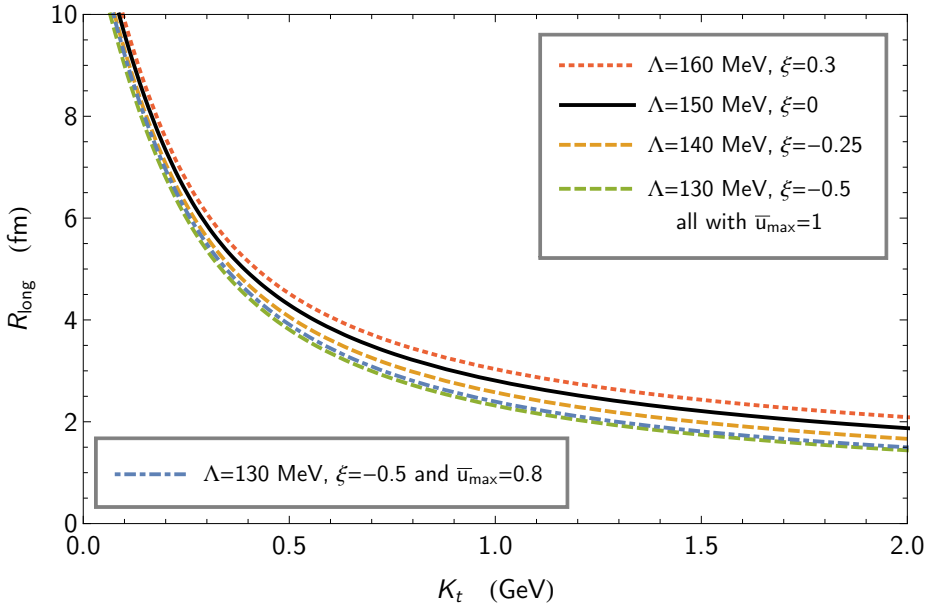

Figure 7.8: HBT-radius $R_{long}(K_t)$ for different choices of Λ, ξ, and $\overline{u}_{max}$.

On the other hand, the radius $R_{long}(K_t)$ is very insensitive to the choice of (Λ, ξ), also seen in figure 7.8. This behavior has already been explained in context of figure 7.4. Finally, $v_3(p_t)$ (figure 7.6) shows more or less the same characteristics as $v_2(p_t)$: For all pairs (Λ, ξ) the curves stay close to each other, with $(\Lambda = 130\,\text{MeV}, \xi = -0.5)$ being the farthest apart from them.

7.3 Discussion

We have argued that there are two main motivations for resorting to an anisotropic momentum distribution to describe the transition from a usual perfect or dissipative hydrodynamic model to a particle distribution at the end of the evolution of the fireball, created in relativistic heavy-ion collisions. First, this ansatz is supported by non-relativistic studies [56]. Second, this could help diminish the sensitivity of computed observables

on the parameters introduced by the decoupling description and thus lead to a smoother matching between models. This is all in the spirit of seeing fluid dynamics emerging as an effective theory caused by some underlying, more microscopic dynamics.

As a matter of fact, our findings for the transverse momentum spectra, $v_2(p_t)$, and $R_{out}(K_t)$ (figures 7.5, 7.6 and 7.7) support the idea of introducing an extra parameter, which governs the local momentum anisotropy at decoupling. It opens a much wider range for the freeze-out temperature Λ without significantly changing the values of the observables. This is admittedly not too surprising, since we introduced one new degree of freedom. Yet it emphasizes the fact that the freeze-out temperature Λ is just a parameter for switching between two models, not a real physical temperature determined by some critical energy or entropy density, for which the medium properties change drastically. As such a parameter, Λ may not have a dramatic impact on measured quantities.

Accordingly, it seems possible to find a whole region of parameters to which the early time signals, like anisotropic flow, are to a large extend insensitive. They carry information on the properties of the fireball along the whole evolution, rather than on decoupling itself [62]. On the other hand, some sensitivity remains for the observables which are governed by the freeze-out process.

We postulated the asymmetric form of the occupation factor at decoupling f_a (see equation (7.4)) and investigated some of the consequences within a toy model. The actual form of f_a, together with that of the associated hydrodynamical quantities, still has to be calculated in a more microscopic approach [58]. This involves at the same time a discussion of the freeze-out hypersurface Σ, whose position in space-time obviously depends on the amount of momentum anisotropy in the phase-space distribution.

8 Conclusion

This conclusion will shortly summarize the main results in terms of dissipative and anisotropic corrections.

8.1 Dissipative corrections

The first goal of this thesis was to expand the method of the sudden freeze-out approximation, solved by a saddle point approximation for a perfect relativistic fluid presented in [6], to a relativistic dissipative fluid. In the process of this expansion we found that the most general result persists. We could group the emitted particles in the process of the freeze-out into two kinds, slow and fast particles. However, new features did arise.

We assumed that the saddle points for the dissipative fluid are the same as for the perfect fluid. Also, we specified the dissipative corrections, where we found that only the first order viscosity corrections (shear and bulk viscosity) were important and that the heat flow could be neglected by choosing the right reference frame (Landau frame).

For slow particles, the dissipative corrections did not change the results of a perfect fluid. The particle spectrum is given by the product of a factor depending on the particle mass and a function depending on the velocity of the emitted particles. The particle spectrum resulted in a mass ordering of the anisotropic flow coefficients, meaning that for heavier particles the flow coefficients decrease.

Turning to fast particles, the bulk viscosity could be neglected and the shear viscosity corrections could be expressed with the help of the Grad's prescription. Analytical results for the transverse momentum spectrum and the anisotropic flow coefficients were found, which reproduced for vanishing shear viscosity the results of a perfect fluid. Also, "new" relations between different flow coefficients were found.

To test the new results for fast particles, the blast-wave model was chosen to calculate the flow coefficients. As it turned out, the absolute

results of the flow coefficients calculated within the saddle point approximation are poor approximations compared to the coefficients in the blast-wave model. However, if the dissipative part of the flow coefficients was isolated, the saddle point approximation gave astonishingly good results compared to the blast-wave model results. Furthermore, if one combined different flow coefficients to calculate the dissipative corrections, another good agreement was found. This is especially convenient, since for an experimental measurement an isolation of the dissipative part alone is not possible.

8.2 Anisotropic corrections

Several articles, like [19] and [55], suggested that an anisotropic momentum distribution could help to describe dissipative corrections.

Therefore, we adapted the idea of [47], but changed the direction of the anisotropy. To understand anisotropic relativistic hydrodynamics, the fundamental hydrodynamical fields were calculated within a kinetic theory. In this calculation we found that the anisotropy can be quantified by two parameters, an anisotropy parameter ξ and an anisotropic temperature Λ. We gained insight on how the anisotropy parameter changes the values of the hydrodynamical fields. From these results we concluded that a negative parameter ξ results in the desired behavior.

Next, we examined the impact of the anisotropy on the freeze-out. Since an analytical calculation within the sudden freeze-out approximation did not give any satisfying results, we reverted to the known blast-wave model from the first part of the thesis to calculate the transverse momentum spectrum, the elliptic and triangular flow coefficients $v_2(p_t)$ and $v_3(p_t)$, and the three possible HBT-radii $R_{out}(K_t)$, $R_{side}(K_t)$ and $R_{long}(K_t)$. To simplify the calculation, only one anisotropic parameter in the out-direction was included.

For a fixed anisotropic temperature and variable anisotropic parameter ξ, we found that the transverse momentum spectrum for negative anisotropic parameters increases for high transverse momenta, while the anisotropic flow coefficients are reduced. Both results were anticipated due to the hydrodynamical results. For the HBT-radii, the radius $R_{out}(K_t)$ changes significantly compared to the isotropic case, while the radius

$R_{long}(K_t)$ hardly changes. Both results were again expected, however, the radius $R_{side}(K_t)$ also changed significantly, which could not be explained.

In the final step, both parameters ξ and Λ were changed in order to find anisotropic solutions which are mostly overlapping with the isotropic solutions. Such parameter sets were indeed found and it is even possible to change other parameters of the blast-wave model without changing the overall results. With the help of anisotropic correction we gained a much smoother transition between the two states, fluid and free particles, in the freeze-out process compared to the sharp transition in the case of dissipative corrections.

8.3 Outlook

In section 5.3, we left aside a few phenomena which could ruin the validity of our findings. There are initial-state fluctuations, but their effect should not be too hard to be dealt with by adding analysis-method-dependent multiplication coefficients [31,34] in front of the flow harmonics in relations (5.63) or (5.64). These are related to the initial eccentricities and can be deduced from the study of integrated flow or from slow particles. A possible more worrisome effect is the rescattering. After the fluid-particle transition, this effect might blur the relations by contributing more anisotropic flow. Again, we think this problem can be handled by exploiting particles that rescatter less and by gauging the influence of hadronic collisions in transport models.

Also, there is an interesting possibility: By investigating particles with different cross sections that decouple at different stages of the evolution, one could hope to map the temperature dependence of the transport coefficients. This can be done once the functional form of δf is known, although it may depend on the particle type. This idea may be followed in the future within more realistic numerical solutions.

As far as for section 7.3, the actual form of f_a, together with that of the associated hydrodynamical quantities, still has to be calculated in a microscopic approach [58]. In this microscopic approach we wish to solve the Boltzmann equation with an anisotropic part to gain not just a postulated distribution function. Until now we have successfully transferred the relativistic Boltzmann equation from a Minkowski coordinate system to a

cylindrical system. In the next step we need to insert the anisotropy into the interaction term of the equation. So far, we assume that a relaxation time approach should be sufficient enough. The solution of the Boltzmann equation should yield a distribution function which already includes the free streaming regime after the freeze-out. The ultimate goal is to achieve new constrains for the anisotropic tensor $\Xi^{\mu\nu}$.

Once this is done, it will be necessary to study how the improved description may be implemented in practice. This is the process of how numerical simulations of dissipative fluid dynamics, anisotropic hydrodynamics, and particle transport are connected with each other in a satisfactory manner. An important point is to check what the shortcomings of the sudden freeze-out approximation, in particular the backflow of particles through Σ [63], become in the new approach. If there is more freedom in choosing the decoupling hypersurface Σ, some choices may be more convenient than others. Eventually, it is of interest to investigate the possible relation of the new description, which in its essence still assumes a sudden conversion from fluid to particles, with continuous emission [50–52]. For instance, one may wonder if it is possible to mimic the latter within the former, or whether one has to formulate a continuous version of the anisotropic freeze-out scenario.

Bibliography

[1] F. Gellis. http://ipht.cea.fr/Pisp/francois.gelis/Physics/2013-orsay1.pdf, Last checked: April, 2016.

[2] S. A. Bass. https://inspirehep.net/record/1256115/files/figs_figure2, Last checked: April, 2016.

[3] L. D. Landau, *Multiple particle production during fast-particle collisions*, *Izv. Akad. Nauk Ser. Fiz.* **17** (1953) 51.

[4] **STAR** Collaboration, K. H. Ackermann et al., *Elliptic flow in Au + Au collisions at (S(NN))**(1/2) = 130 GeV*, *Phys. Rev. Lett.* **86** (2001) 402–407, [nucl-ex/0009011].

[5] L. D. McLerran, *Two lectures on small x delete and high gluon density*, *Acta Phys. Polon.* **B30** (1999) 3707–3729, [nucl-th/9911013].

[6] N. Borghini and J.-Y. Ollitrault, *Momentum spectra, anisotropic flow, and ideal fluids*, *Phys.Lett.* **B642** (2006) 227–231, [nucl-th/0506045].

[7] A. K. Chaudhuri, *A short course on relativistic heavy ion collisions*. IOP Publishing, 2014.

[8] L. Rezzolla, O. Z. L. Rezzolla, O. Z. L. Rezzolla, and O. Zanotti, *Relativistic hydrodynamics*. Oxford, 2013.

[9] F. Cooper and G. Frye, *Comment on the Single Particle Distribution in the Hydrodynamic and Statistical Thermodynamic Models of Multiparticle Production*, *Phys. Rev.* **D10** (1974) 186, [DOI: 10.1103/PhysRevD.10.186].

[10] W. Florkowski, *Phenomenology of ultra-relativistic heavy-ion collisions*. World Scientific, 2010.

[11] J. Y. Ollitrault, *Collective dynamics in heavy ion collisions*, *NATO Sci. Ser. II* **87** (2002) 237. [237(2002)].

[12] U. A. Wiedemann, *Heavy-ion collisions: Selected topics*, in *Proceedings, 2007 European School of High-Energy Physics (ESHEP 2007)*, pp. 277–306, 2008.

[13] P. Huovinen, *Hydrodynamics at RHIC and LHC: What have we learned?*, *Int. J. Mod. Phys.* **E22** (2013) 1330029, [arXiv:1311.1849].

[14] G. Baym, *The Physics of Hanbury Brown-Twiss intensity interferometry: From stars to nuclear collisions*, *Acta Phys. Polon.* **B29** (1998) 1839–1884, [nucl-th/9804026].

[15] N. Borghini, "Hydrodynamics." https://www.physik.uni-bielefeld.de/~borghini/Teaching/Hydrodynamics/Hydrodynamics.pdf, Last update: September, 2015.

[16] C. Eckart, *The thermodynamics of irreversible processes. iii. relativistic theory of the simple fluid*, *Phys. Rev.* **58** (Nov, 1940) 919–924, [DOI: 10.1103/PhysRev.58.919].

[17] L. D. Landau and E. M. Lifshitz, *Fluid mechanics*, vol. 6 of *Course of theoretical physics*. Pergamon Press, 1987.

[18] J. M. S. W. Israel, *Transient relativistic thermodynamics and kinetic theory*, *Annals Phys.* **118** (1979) 341–372.

[19] M. Strickland, *Anisotropic hydrodynamics: Three lectures*, arXiv:1410.5786.

[20] D. Teaney, *The Effects of viscosity on spectra, elliptic flow, and HBT radii*, *Phys. Rev.* **C68** (2003) 034913, [nucl-th/0301099].

[21] K. Dusling and D. Teaney, *Simulating elliptic flow with viscous hydrodynamics*, arXiv:0710.5932.

[22] D. Teaney and L. Yan, *Second order viscous corrections to the harmonic spectrum in heavy ion collisions*, arXiv:1304.3753.

[23] G. S. Denicol, T. Kodama, T. Koide, and P. Mota, *Effect of bulk viscosity on elliptic flow near qcd phase transition*, arXiv:0903.3595.

[24] A. Monnai and T. Hirano, *Effects of bulk viscosity at freezeout*, arXiv:0903.4436.

[25] K. Dusling, G. Moore, and D. Teaney, *Radiative energy loss and v2 spectra for viscous hydrodynamics*, arXiv:0909.0754.

[26] S. Pratt and G. Torrieri, *Coupling relativistic viscous hydrodynamics to boltzmann descriptions*, arXiv:1003.0413.

[27] K. Dusling and T. Schaefer, *Bulk viscosity, particle spectra and flow in heavy-ion collisions*, arXiv:1109.5181.

[28] D. Molnar, *Identified particles from viscous hydrodynamics*, arXiv:1107.5860.

[29] M. Luzum and J.-Y. Ollitrault, *Constraining the viscous freeze-out distribution function with data obtained at the bnl relativistic heavy ion collider (rhic)*, arXiv:1004.2023.

[30] C. Lang and N. Borghini, *Dissipative corrections to particle spectra and anisotropic flow from a saddle-point approximation to kinetic freeze out*, *Eur. Phys. J.* **C74** (2014) 2955, [arXiv:1312.7763].

[31] D. Teaney and L. Yan, *Non linearities in the harmonic spectrum of heavy ion collisions with ideal and viscous hydrodynamics*, arXiv:1206.1905.

[32] L.V.Bravina, B. Johansson, G.Kh.Eyyubova, V.L.Korotkikh, I.P.Lokhtin, L.V.Malinina, S.V.Petrushanko, A.M.Snigirev, and E.E.Zabrodin, *Hexagonal flow v_6 as a superposition of elliptic v_2 and triangular v_3 flows*, arXiv:1311.0747.

[33] P. Danielewicz, *Effects of compression and collective expansion on particle emission from central heavy ion reactions*, *Phys. Rev.* **C51** (1995) 716–750, [nucl-th/9408018].

[34] C. Gombeaud and J.-Y. Ollitrault, *Effects of flow fluctuations and partial thermalization on v_4*, arXiv:0907.4664.

[35] N. Borghini and C. Gombeaud, *Anisotropic flow far from equilibrium*, arXiv:1012.0899.

[36] P. J. Siemens and J. O. Rasmussen, *Evidence for a blast wave from compress nuclear matter*, *Phys. Rev. Lett.* **42** (1979) 880–887, [DOI: 10.1103/PhysRevLett.42.880].

[37] P. Huovinen, P. F. Kolb, U. W. Heinz, P. V. Ruuskanen, and S. A. Voloshin, *Radial and elliptic flow at RHIC: Further predictions*, *Phys. Lett.* **B503** (2001) 58–64, [hep-ph/0101136].

[38] **ALICE** Collaboration, Y. Zhou, *Anisotropic flow of identified particles in Pb–Pb collisions at $\sqrt{s_{\rm NN}} = 2.76$ TeV with the ALICE detector*, *J. Phys. Conf. Ser.* **509** (2014) 012029, [arXiv:1309.3237].

[39] **STAR** Collaboration, V. Bairathi, *Azimuthal anisotropy of phi meson in u+u and au+au collisions at rhic*, *J. Phys. Conf. Ser.* **668** (2016), no. 1 012039, [DOI: 10.1088/1742-6596/668/1/012039].

[40] M. Martinez and M. Strickland, *Dissipative dynamics of highly anisotropic systems*, arXiv:1007.0889.

[41] L. Tinti, *(3+1)-dimensional framework for leading-order non conformal anisotropic hydrodynamics*, *Phys. Rev. C* **92** (2015) 014908, [arXiv:1411.7268].

[42] G. Policastro, D. Son, and A. Starinets, *Shear viscosity of strongly coupled n=4 supersymmetric yang-mills plasma*, *Phys.Rev.Lett.* **87** (2001) 081601, [hep-th/0104066].

[43] S. Feld, *Freeze-out eines anisotropen fluids in hoch-energetischen schwerionenkollisionen*, Master's thesis, University Bielefeld, 2015.

[44] D. Bazow, U. W. Heinz, and M. Strickland, *Second-order (2+1)-dimensional anisotropic hydrodynamics*, *Phys. Rev. C 90, 054910* (11, 2013) [arXiv:1311.6720].

[45] M. Nopoush, R. Ryblewski, and M. Strickland, *Bulk viscous evolution within anisotropic hydrodynamics*, arXiv:1405.1355.

[46] L. Tinti and W. Florkowski, *Projection method and new formulation of leading-order anisotropic hydrodynamics*, *Phys. Rev. C* **89** (2014) 034907, [arXiv:1312.6614].

[47] M. Rybczyński and W. Florkowski, *Locally anisotropic momentum distributions of hadrons at freeze-out in relativistic heavy-ion collisions*, arXiv:1206.6587.

[48] N. Borghini, S. Feld, and C. Lang, *Kinetic freeze out from an anisotropic fluid in high-energy heavy-ion collisions: particle spectra, hanbury brown-twiss radii, and anisotropic flow*, arXiv:1412.5199.

[49] T. Hirano, P. Huovinen, K. Murase, and Y. Nara, *Integrated dynamical approach to relativistic heavy ion collisions*, arXiv:1204.5814.

[50] F.Grassi, *Particle emission in hydrodynamics: a problem needing a solution*, *Braz.J.Phys.* **35** (2005) 52–69, [nucl-th/0412082].

[51] F. Grassi, Y. Hama, and T. Kodama, *Continuous particle emission: A Probe of thermalized matter evolution?*, *Phys. Lett.* **B355** (1995) 9–14, [DOI: 10.1016/0370-2693(95)00686-F].

[52] F. Grassi, Y. Hama, and T. Kodama, *Particle emission in the hydrodynamical description of relativistic nuclear collisions*, *Z. Phys.* **C73** (1996) 153–160, [DOI: 10.1007/s002880050305].

[53] Y. M. Sinyukov, S. V. Akkelin, and Y. Hama, *On freeze-out problem in hydro-kinetic approach to a+a collisions*, *Phys.Rev.Lett.* **89** (2002) 052301, [nucl-th/0201015].

[54] W. Florkowski and R. Ryblewski, *Highly-anisotropic and strongly-dissipative hydrodynamics for early stages of relativistic heavy-ion collisions*, arXiv:1007.0130.

[55] R. Ryblewski, *Anisotropic hydrodynamics for ultra-relativistic heavy-ion collisions*, *J. Phys.* **G40** (2013) 093101, [DOI: 10.1088/0954-3899/40/9/093101].

[56] D. W. B.B. Hamel, *Kinetic theory of source flow expansion with application to the free jet*, *Phys. Fluids* **9** (1966), no. 829.

[57] M. I. Gorenstein and Yu. M. Sinyukov, *Local Anisotropy Effects in the Hydrodynamical Theory of Multiparticle Production*, *Phys. Lett.* **B142** (1984) 425–428, [DOI: 10.1016/0370-2693(84)91355-8].

[58] N. Borghini, S. Feld, and C. Lang, "in preparation."

[59] P. Romatschke and M. Strickland, *Collective modes of an anisotropic quark-gluon plasma*, *Phys.Rev.D* **68** (2003) 036004, [hep-ph/0304092].

[60] M. T. G. Bertsch, M. Gong, *Pion interferometry in ultrarelativistic heavy-ion collisions*, *Phys. Rev.* **37** (1988) 1896.

[61] M. A. Lisa and S. Pratt, *Femtoscopically probing the freeze-out configuration in heavy ion collisions*, arXiv:0811.1352.

[62] U. W. Heinz and R. Snellings, *Collective flow and viscosity in relativistic heavy-ion collisions*, arXiv:1301.2826.

[63] S. Pratt, *Accounting for backflow in hydrodynamic-simulation interfaces*, arXiv:1401.0316.

Acknowledgements

I want to thank Nicolas Borghini for the supervision of this thesis and the support during my time at the University Bielefeld.

Further, I wish to thank Steffen Feld for support and collaboration on the second part of this thesis and for proofreading.

I want to thank my family, who always provided support during my life.

Also, I want to thank Viktor, Nina, Steffen (again), Hauke, Kathrin, Dennis and all the other members of the high energy physics workgroup for a pleasant work environment and good working atmosphere.

Outside the research group I want to thank Niklas, Hendrik, Sascha and Markus for enjoyable years at the University Bielefeld.

Declaration of authorship

I hereby declare that I have written this thesis without the assistance of any other person. The thesis has not been previously submitted to any examination office. Only the sources and literature indicated have been used.

Christian Lang